INVESTIGATION OF INTERCALATION IN GRAPHITE ELECTRODES THROUGH IN-SITU IMAGING

Madeline Shea Stark

A dissertation submitted to the faculty at the University of North Carolina at Chapel Hill in partial fulfillment of the requirements for the degree of Doctor of Philosophy in the Department of Chemistry in the College of Arts and Sciences.

Chapel Hill
2021

Approved by:

Scott C. Warren

Joanna Atkin

James Cahoon

Carrie Donley

Wei You

© 2021
Madeline Shea Stark
ALL RIGHTS RESERVED

ABSTRACT

Madeline Shea Stark: Investigation of Intercalation in
Graphite Electrodes with in-situ Imaging
(Under the direction of Scott C. Warren)

Intercalation in layered materials is a rapidly growing area of research to develop next-generation energy-storage and optoelectronic devices, including batteries, sensors, transistors, and electrically tunable displays. Advances in few-layer intercalation are addressed in the historical context of bulk intercalation (Chapter 1), emphasizing electrochemical techniques, mechanism of intercalation, and optoelectronic properties. Despite immense progress, there is still a critical need for simple devices that enable *in-situ* characterization of a variety of layered electrodes across the electromagnetic spectrum. In addition, a straightforward method of analyzing staging and calculating transport rates in layered materials from *in-situ* optical measurements would facilitate direct comparisons between experimental observations and computational models. This work describes efforts to address both of these needs through device design (Chapter 3) and the development of an image analysis platform (Chapter 4). Detailed synthesis, characterization, and electrochemical methods are described in Chapter 2.

Engineering electrode materials for optoelectronic and energy storage applications requires a fundamental understanding of intercalation using spatially-resolved techniques. However, spectroscopic methods can have limited spatial resolution and low intensity since the signal passes through electrolyte. In Chapter 3, a device geometry is presented in which the electrolyte is laterally separated from the area probed spectroscopically, so that the signal

does not pass through the electrolyte. This geometry enables us to visualize ion transport with optical microscopy and monitor charge transfer with Raman and visible reflectance spectroscopies. In addition, vibrational changes are probed in the mid-IR, a region previously difficult to access due to electrolyte absorption.

Our observation of colorful domains (i.e. intercalant islands) that move rapidly during the stage 2-1 transition in Chapter 3 motivated us to investigate origin of these colors and transport rates (Chapter 4). We designed an image analysis program in Python to analyze color patterns and calculate (de)intercalation rates of the moving domains. This multifunctional program enabled us to compare differences in the distribution of transport rates among different domains, colors, and (de)intercalation. Our observations support a substage model of intercalation and suggest that structural features and electrostatic interactions affect ion transport.

To my family and my husband, thank you for your love and support.

ACKNOWLEDGMENTS

Special thanks to my advisor, Scott for taking a chance and giving me the opportunity to work in the Warren lab during my first year. I couldn't have asked for a better mentor throughout graduate school. Over the years, you have consistently challenged me to grow as a writer, teacher, and scientist. I appreciate all of the encouragement and advice you have given me throughout graduate school.

To all of my lab mates in grad school: Adam, Tyler, Dan, Kaci, Suzanne, Anginelle, Jacob, Sean, Zack, Jack, Lauren, Jessica, Matt, Becca, Connor, Duncan, and Karen, thank you for creating a welcoming and fun work environment in the Warren lab. From escape rooms and dinners to virtual game nights and lab chats, you all made these past five years fly by. It has been an honor to work with such a talented group of researchers during my time here and I look forward to seeing what you all do next.

In addition, I want to acknowledge the amazing undergraduates who worked with me over the past four years, Hailey Kim, Judy Cheng, and Carolyn Chen. Your creativity and excitement for research inspired me every day. The projects described in this dissertation would not have been possible without your hard work and contributions. I wish you all the best in your future endeavors.

To my church family and life group, thank you all for your friendship, for the supportive community you provided to challenge me to grow in my faith, and for praying for me continually during grad school.

To my family, I am deeply grateful to you all for your love and support. You have given me so much, and I appreciate how you've always been there for me, cheering me on. Thank you for reminding me that chemistry isn't everything and helping me stay positive. To my sisters, I'm so proud of you all and I'm excited to see the things that you do in the future. I love y'all!

Finally, to my husband Michael, thank you for being my constant support and best friend. I'm glad we both ended up at UNC so that we could meet. You have definitely listened to more than you ever cared to know about my struggles with graphite intercalation, coding, and COMSOL, and I appreciate your insights that help keep things perspective. From our walks together, playing games, and Maple View dates, I always enjoy spending time with you as you encourage me to grow as a person and a scientist. Looking forward to the next stage of our adventure together. I love you!

TABLE OF CONTENTS

LIST OF FIGURES xii

CHAPTER 1 – INTRODUCTION 1

1.1 History of Layered Intercalation Compounds 5

1.2 Electrochemical Methods of Intercalation 8

1.3 Structure 13

1.3.1 Intercalation Staging Model 13

1.3.2 Lattice Expansion 16

1.3.3. Solid-Electrolyte Interphase 18

1.4 Electronic Properties 24

1.4.1. Charge Transfer 25

1.4.2 Conductivity 36

1.5 Optical Properties 41

1.6 Conclusions and Outlook 51

REFERENCES 55

CHAPTER 2 – METHODS 67

2.1 Introduction 67

2.2 Electrochemical Device Design 67

2.3 Electrochemical techniques 70

2.3.1 Setting up the Electrochemical Measurement 71

2.3.2 Intercalation of Bulk Graphite using CP 72

2.4 Synthesis of CVD graphite 74

2.4.1 Substrate Preparation 74

2.4.2 Few-layer graphite synthesis 75

2.4.3 Transfer to new substrate 76

2.4.4 Characterizing the transferred film 79

2.4.5 Initial intercalation results 81

2.5 Nanosphere Lithography (NSL) 82

2.6 Ultrathin Flake Intercalation 89

2.6.1 Mechanical exfoliation to form the working electrode 89

2.6.2 Device design and electrochemistry 90

2.6.3 Optical microscopy 91

2.6.4 Raman spectroscopy 91

2.6.5 Characterizing the intercalation of ultrathin flakes 91

REFERENCES 98

CHAPTER 3 – ELECTROLYTE-FREE SPECTROSCOPY AND IMAGING OF INTERCALATION IN GRAPHITE ELECTRODES 99

3.2 Methods 101

3.2.1 Device Design 101

3.2.2 Electrochemistry 107

3.2.3 Optical Microscopy 110

3.2.4 Raman Spectroscopy 110

3.2.5 UV-vis Spectroscopy 112

3.2.6 FT-IR Spectroscopy 112

3.3 Device Design 113

3.4 Optical Microscopy 113

3.5 Raman Spectroscopy 117

3.6 UV-Vis Spectroscopy 120

3.7 FTIR-Spectroscopy 121

3.8 Conclusions and Future Work 122

REFERENCES 124

CHAPTER 4 – STAGING DYNAMICS AND ION TRANSPORT RATES IN GRAPHITE ELECTRODES 126

4.1 Introduction..... 126

4.2 Developing the Image Analysis Program 128

4.2.1 Masking methods 129

4.2.2 Edge detection method 132

4.2.3 Velocity calculation method..... 134

4.3 Characterizing Staging Dynamics 138

4.4 Conclusion and Future Work..... 151

REFERENCES.....154

LIST OF FIGURES

Figure 1-1. Potassium intercalation of graphite. 2

Figure 1-2. History of intercalation of layered compounds: bulk to 2D. 4

Figure 1-3. Layered structures 6

Figure 1-4. Density of states 7

Figure 1-5: Electrochemical cell designs for in-situ studies 11

Figure 1-6. Galvanostatic curve for the intercalation of lithium into graphite. 15

Figure 1-7. Raman spectra during lithium intercalation. 16

Figure 1-8. SEI thickness for spherical graphite particles of various radii during lithiation .. 21

Figure 1-9. Schematic of Li diffusion through amorphous and crystalline layers of SEI. 22

Figure 1-10. Phonon-dispersion and the corresponding DOS plots for stages 1 a) and 3 c) .. 26

Figure 1-11. Band Structure and Emission spectra for Li-intercalated graphite. 29

Figure 1-12. The density of states based on the calculated band structure of KC_8 30

Figure 1-13. The representative mechanism of disproportionation in GICs 32

Figure 1-14. Halide intercalation into graphite. 34

Figure 1-15. $FeCl_3$ intercalation into graphite. 36

Figure 1-16. UPS for donor and acceptor species 38

Figure 1-17. Thickness dependence of Rs for GICs. 41

Figure 1-18. Plasma frequency shifts for acceptor GICs. 46

Figure 1-19. Plasma frequency shifts for donor GICs 47

Figure 1-20. Transmittance as a function of wavelength for LiC_6 50

Figure 2-1: Chronopotentiogram for bulk HSO4- GIC. 73

Figure 2-2: Transfer process for FLG. 78

Figure 2-3: XPS spectra of FLG surface 79

Figure 2-4: Characterizing the FLG after transfer 80

Figure 2-5: Raman spectra of transferred FLG 81

Figure 2-6: Optical microscopy images of the intercalation of transferred graphite. 82

Figure 2-7: Sequence of steps to make h-FLG 83

Figure 2-8: SEM images of the PS spheres on the surface of the FLG 84

Figure 2-9: SEM images of the alumina mask after removal of the PS spheres on the surface of the FLG. 85

Figure 2-10: XPS for the alumina mask before and after removal 87

Figure 2-11: XPS for the alumina mask after removal 88

Figure 2-12: Cyclic voltammetry of graphite flakes. 94

Figure 2-13: Optical images of graphite flakes acquired during cyclic voltammetry. 94

Figure 2-14: Optical microscopy images of mechanically-exfoliated HOPG flakes on a platinum substrate 95

Figure 2-15: CV of the ultrathin flakes using the modified exfoliation method 95

Figure 3-1: Fabricating the electrolyte-free device. 104

Figure 3-2: Fabricating the electrolyte and electrolyte-free devices. 105

Figure 3-3: Chronopotentiogram showing the stage transitions in the electrolyte device. 108

Figure 3-4: Chronopotentiogram showing the stage transitions in the electrolyte-free device. 109

Figure 3-5: Raman spectra of (a) electrolyte and (b) electrolyte-free regions. 111

Figure 3-6. Device schematic and in-situ optical microscopy images in electrolyte and electrolyte-free environments. 114

Figure 3-7. Raman shifts of the graphite G-peak..... 118

Figure 3-8. In-situ visible reflectance spectra of graphite in (a) the electrolyte and (h) the electrolyte-free environments. 120

Figure 3-9. Mid-infrared spectra of the electrolyte region (a) and the electrolyte-free environment 122

Figure 4-1: Optical microscopy images showing the domains of color during (a-f) intercalation and (g-l) deintercalation. 128

Figure 4-2: Comparison of the pixel groupings that result from segmentation 129

Figure 4-3: Color masks (a,c,e,g,i,k) that result from image segmentation of the frames.... 131

Figure 4-4: A frame that has a) undergone image segmentation and recoloring, and b) subsequent Canny edge detection. 134

Figure 4-5: Illustration of optical flow..... 136

Figure 4-6: Scheme that illustrates what the periodic patterns in local domains could look like,..... 139

Figure 4-7: Demonstration of how the colors emerge over time 140

Figure 4-8: Comparing the distribution of speeds for a) intercalation and b) deintercalation..... 141

Figure 4-9: Comparison of the distribution of rates observed for each of the colors 142

Figure 4-10: Comparing the distribution of rates during early and late times during intercalation..... 143

Figure 4-11: Comparing the distribution of rates during early and late times during deintercalation..... 144

Figure 4-12: Investigating the speed distributions of a) individual domains during intercalation..... 146

Figure 4-13: Investigating the speed distributions of a) individual domains during deintercalation 147

Figure 4-14: Analysis of domain 1 148

Figure 4-15: Analysis of domain 3 149

Figure 4-16: Analysis of domain 2 150

Figure 4-17: Analysis of domain 6 151

CHAPTER 1 – INTRODUCTION[1]

*Madeline S. Stark[§], Kaci L, Kuntz[§#], Sean J. Martens[§#], and Scott C. Warren[§±]**

[§]Department of Chemistry, and Department of Applied Physical Sciences, [±]University of North Carolina at Chapel Hill, Chapel Hill NC, 27599. USA.

[#]These authors contributed equally.

Intercalation in layered materials is a process that profoundly alters chemical, electrical, optical, and magnetic properties, enabling applications in areas from batteries to superconductors to drug delivery. The emergence of 2D materials is now creating exciting opportunities to understand fundamental questions, such as how intercalation depends on material thickness and lateral size. Moreover, because 2D materials can be stacked in virtually any sequence to form van der Waals (vdW) heterostructures, a fascinating area of intercalation is now just emerging in which the internal interfaces of layered materials can be engineered.[2,3][4] Collectively, these new material architectures are leading to observations of fascinating phenomena such as optical switching,[5–8] mixed ionic and electronic conduction,[9] and exotic charge transport physics.[10] These materials are also being integrated into new device architectures because of their mechanical flexibility, with potential applications including wearable devices[11–14] or 2D-on-silicon integrated circuits[15]. While recent reviews have focused on the synthesis and properties of 2D intercalation compounds,[16,17] here, we present an account of how intercalation changes in 2D materials with thickness, lateral size,

and stacking sequence, and we make comparisons to intercalation in bulk materials. We focus on establishing scaling laws for the transition between bulk and 2D materials, and we focus particularly on aspects of the physical structure of intercalation compounds, and their optical and electronic properties.[5,16–18]

Intercalation is the insertion of guest species into the void space of a layered host structure. Many layered and few-layer materials are promising hosts for intercalation because they have weak vdW interlayer interactions that allow the host to expand readily and the guest to diffuse quickly. As guest species insert into the interlayer gap of layered host materials, the chemical and physical properties are radically altered.[19–21] For example, shown in **Figure 1-1**, graphite is a grey semi-metal with an in-plane carrier concentration of $5.5 \cdot 10^{12}$ electrons cm^{-2}, while potassium-intercalated graphite KC_8 is a golden metal with a carrier concentration of $5 \cdot 10^{14}$ electrons cm^{-2}.[5]

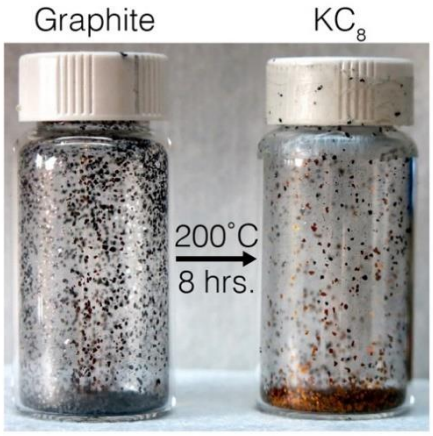


Figure 1-1. Potassium intercalation of graphite. Semi-metallic graphite, shown on the left, has a dark grey color, while potassium-intercalated graphite (KC_8) is metallic with a golden color, shown on right.

The magnitude of charge transfer between the host and intercalant—altering the carrier concentration—naturally creates opportunities to construct high-performance batteries as well

as optoelectronic switches and sensors.

In 1841, the first layered intercalation compound was reported.[22–24] Nearly a century later, intercalation-induced changes in structure[25,26] and properties[27–30] were systematically investigated for various layered intercalation compounds (**Figure 1-2**). In the decades that followed, researchers explored the charge transfer between the guest and host[29] and found that the host lattices have interesting properties, such as conductivity as high as copper[27,28] and tunable optical properties, with a single material changing colors from to black to blue to gold[23,30] to transparent[6,31]. The mechanism of intercalation was not understood until the late 1960s when models were developed for the kinetics and thermodynamics of intercalation of bulk layered crystals.[32]

With an understanding of the intercalation process, layered intercalation compounds with high conductivity, high capacity, and minimal lattice expansion began to find applications in energy storage, including lithium-ion batteries[24,33–36]. With the discovery of graphene in 2004[37] and the subsequent emergence of many new 2D materials, the properties of 2D intercalation compounds began to inspire curiosity, in large part because of the radical changes seen in the properties of 2D materials versus their bulk counterparts.

2D materials exhibit novel properties relative to bulk material due to variations in their electronic structure. For example, MoS_2 transitions from a bulk semiconductor with an indirect band gap to a monolayer with a direct band gap.[38–40] Black phosphorus (BP) is a semiconductor with a thickness-dependent band gap.[41–46] Because of their thickness-dependent properties, intercalation of 2D and few-layer materials offers a unique platform to further alter the electronic,[6,7,47] optical,[6,8,48] and magnetic[49,50] properties that are not

realizable in the bulk form.

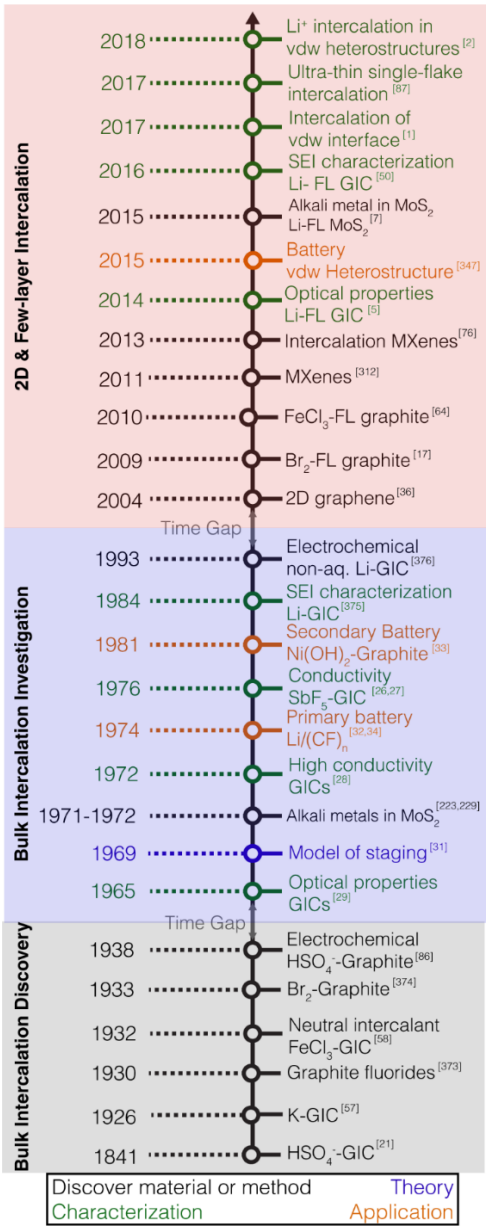


Figure 1-2. History of intercalation of layered compounds: bulk to 2D. Modified and updated with permission.[24] Copyright 1998, Elsevier Ltd. Reprinted from Journal of Power Sciences, 72, M. Noel and R. Santhanam, Electrochemistry of graphite intercalation compounds, 53-65, 1998, with permission form Elsevier.[33] Copyright 1989, Cambridge University Press.

Due to the inherent structure of 2D and few-layer materials relative to bulk material, 2D intercalation is anticipated to exhibit faster kinetics,[20,51–54] experience greater effects resulting from surface interactions,[52,54] and have interesting mechanical properties such as flexibility and strain-induced effects[2,3]. Differences between the intercalation of bulk and few-layer materials are likely a consequence of thickness and lateral size dependence, resulting in more uniformly staged intercalation compounds than bulk intercalation compounds with faster kinetics.[20,51–54] The increase in surface area relative to thickness of 2D materials implies that surface interactions with intercalants play a more crucial role in the charge transfer between guest and host.[52,54] Additionally, the flexibility of 2D materials can likely be imparted to 2D intercalation compounds, expanding the application of intercalation compounds to flexible electronics. Furthermore, one of the more exciting aspects of 2D intercalation compounds is the ability to build vdW heterostructures[2,3] to selectively design structures with desired change/discharge rates, surface interactions, flexibility, and strain-influenced intercalation.[2,3] Despite the interesting advantages of few-layer intercalation, intercalation of 2D and few-layer materials remains relatively unexplored.

1.1 History of Layered Intercalation Compounds

In 1841, the first layered intercalation compound was discovered, H_2SO_4—Graphite, as H_2SO_4 and HSO_4^- inserted into the interlayer space of graphite.[23,55] This electron-withdrawing intercalant results in hole-doped graphite. Interestingly, potassium intercalated graphite, discovered in 1926,[56] results in an electron-doped host. In the 1930s, neutral species, such as $FeCl_3$,[57] were found to intercalate the layered host. Since these early studies of graphite intercalation compounds (GICs), a variety of layered materials have been observed to host various atoms, ions, and molecules (Figure 1-2).[19–21,23,58]

In 1969, the model of staging was introduced, where a stage is defined as the ratio of host to guest layers.[32] In a stage 1 compound, layers alternate between intercalant and host, while in a stage 2 compound, a layer of intercalant is separated by two layers of host (**Figure 1-3**a). In these intercalated materials, host layers adjacent to intercalant species are called bounding layers, while layers not adjacent are interior layers (Figure 1-3a). Stage 1 is generally the highest degree of intercalation and lower stages (e.g. 3, 4, 5, etc.) are also often observed. During intercalation, the host lattice usually expands as guest species insert into the interlayer space (Figure 1-3a), creating thermodynamic and kinetic barriers for intercalation and diffusion.[17,23] Notably, the intercalation of bulk layered materials occurs more quickly in smaller, thinner samples.[20,52] In addition to faster kinetics, the resulting intercalation compounds reach higher (e.g. stage 1), more homogenous staging.[20]

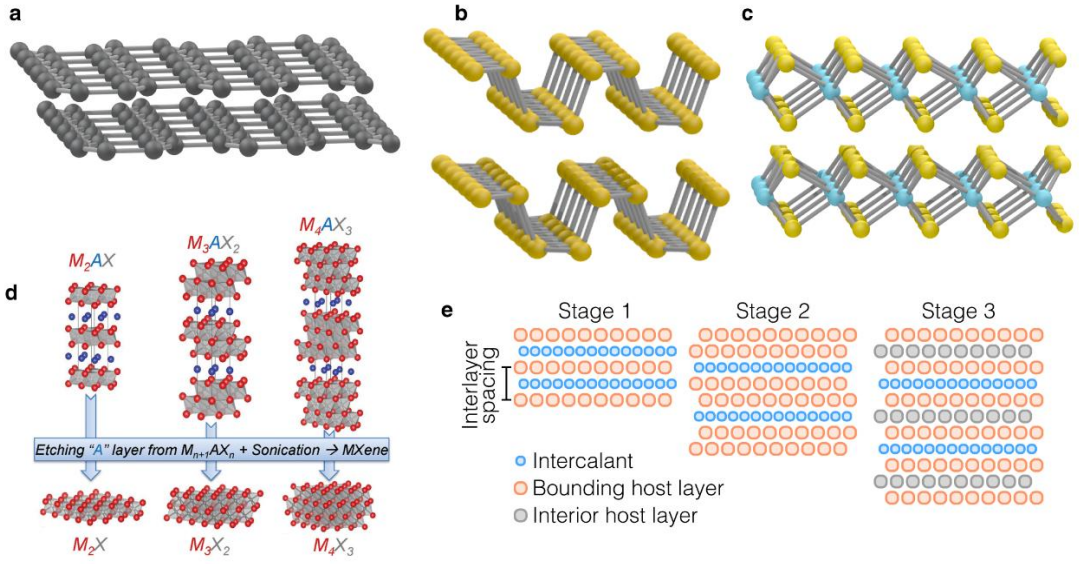


Figure 1-3. Layered structures depicting a) stages of intercalation are shown for graphite depicting the c-axis lattice expansion with guest insertion, b) bilayer graphite, c) bilayer black phosphorus, d) bilayer MoS_2, and e) MXenes derived from parent MAX phase. Reproduced with permission.[59] Copyright 2014, John Wiley & Sons Inc.

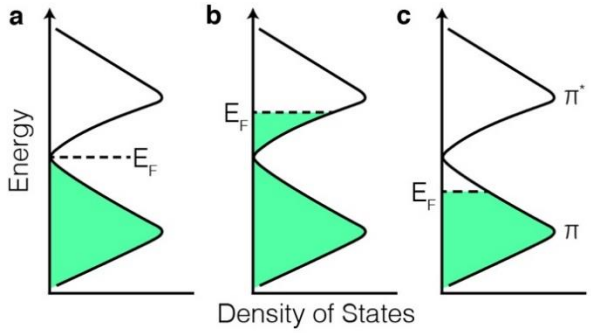


Figure 1-4. Density of states of a) graphite, b) donor-intercalated graphite, c) acceptor-intercalated graphite at 0 K depicting the Fermi level E_F shift with respect to the bonding π-type and anti-bonding π^*-type bands.

Depending on the nature of the intercalant and the host, a donor or acceptor intercalation compound forms. The charge transfer between the guest and host is described from the perspective of the intercalant. For example, in donor-type compounds, the guest species (*D*) donate electrons to the host layer (*H*), shown in **Equation 1**. However, in acceptor compounds, the inserted species (*A*) accept electrons from *H*, shown in **Equation 2**.

$$H_x + D \rightleftharpoons H_x^- \cdot D^+ \quad (1)$$

$$H_x + A \rightleftharpoons H_x^+ \cdot A^- \quad (2)$$

These charge transfer mechanisms can dramatically alter the carrier concentration or electronic structure of the host lattice. For example, graphite intercalates anionic, cationic, or neutral species, due in part to its electronic structure.[60] Graphite lacks a bandgap at the Fermi level E_F (**Figure 1-4**a) and results in identical values for the ionization energy and electron affinity. This allows graphite to be easily reduced or oxidized in a chemical reaction; as such, graphite is described as amphoteric. Therefore, during an intercalation process, electrons can be donated by the intercalant to the host (Figure 1-4b) or accepted by the intercalant (Figure 1-4c).[60] With intercalation, semi-metallic graphite becomes metallic as the concentration of electrons or holes at E_F increases with charge transfer from donor or acceptor species, respectively.[23,58,60–

[62] Due to the high density of carriers near E_F, to date, all species of intercalants result in metallic GICs.[62]

The electronic structure of intercalation compounds yields interesting electronic and optical properties. In 1965, graphite demonstrated increased transmission after intercalation due to the metallic optical responses of intercalated compounds.[30] An increase of in-plane conductivity in GICs was observed in 1972, leading to the description of these compounds as "synthetic metals."[29] In 1976, SbF_5-intercalated graphite demonstrated conductivity of 10^8 S/cm, which is higher than copper.[27,28] With high conductivity, graphite and fluorinated-graphite materials found commercial application as intercalation hosts in primary[33,34] and secondary[35] batteries in the 1970s. Since 2D and few-layer intercalated compounds exhibit electronic structures that are distinct from bulk, the increase in carrier density, high conductivity, and optical response of 2D intercalation compounds are of interest for switchable optical behavior and technologies with highly confined dimensions.

1.2 Electrochemical Methods of Intercalation

Since the discovery of intercalation, many techniques have been developed to produce these compounds. Studies of intercalation in bulk layered materials show that the structure and quality of the host lattice play an important role, as do temperature, pressure, and concentration. In addition, the chemical and physical properties of the guest species determine the intercalation technique that is appropriate for a specific host/guest pair.[20] Each synthetic route affects the kinetics of intercalation, impacts the quality of the resulting product, and can dictate the applications of the intercalation compound. With many synthetic routes to layered intercalation compounds, current techniques for 2D and few-layer intercalation fit into these

classes: gaseous, non-electrochemical solution-phase, or electrochemical (aqueous or solid-state) methods. With extensive reviews of bulk layered intercalation,[17,19,20,23,60,63] here we will focus on the electrochemical synthetic routes that have also been applied to few-layer materials.

Electrochemical intercalation offers a unique platform to reversibly intercalate layered materials. It allows for precise control of chemical, electronic, and optical properties. Electrochemical intercalation is driven by an external voltage or current (Figure 1-5d). The source provides an electron in the intercalation process, which is shown for a donor compound (**Equation 1-3**) and an acceptor compound (**Equation 1-4**).

$$H_x + D^+ + e^- \rightleftharpoons H_x^- \cdot D^+ \quad (3)$$

$$H_x + A^- \rightleftharpoons H_x^+ \cdot A^- + e^- \quad (4)$$

This method of intercalation is highly advantageous because staging is readily controlled by the external source (e.g. via control of the electrochemical potential of electrons in the host material)[64–66] and allows for the stoichiometry of the intercalant compounds to be observed directly through chronopotentiometry or chronoamperometry.[63] Moreover, the amount of charge transferred between an intercalant and host can be estimated through the integration of the current versus time curve.[63]

With the high degree of control and reversibility, electrochemical intercalation is used in energy technologies and is promising for optoelectronic devices. The first intercalated compound, H_2SO_4—graphite, was initially produced by a non-electrochemical, solution-phase method in 1841,[22] and then electrochemically intercalated for the first time in 1938.[67]

Initially, alkali metals were intercalated thermally; however, they found application in Li-ion batteries through electrochemical intercalation.[33–35]

With the recent emergence of 2D and few-layer intercalation compounds, electrochemical methods facilitate *in-situ* study of the intercalation. For example, electrochemical intercalation in few-layer graphene[6,51] and MoS_2[8] enabled observation of the kinetics of intercalation,[8] staging,[51] changes in optical properties,[6,8] formation of the SEI,[51] differences in mechanism,[68] and the role of defects.[51,68] The design of an electrochemical cell dictates the properties that can be studied *in-situ*, with various setups shown in **Figure 1-5**.

The electrochemical cell design determines the type of investigation that can be performed, such as optical (Figure 1-5a) or electronic (Figure 1-5a,b) studies of thin films or single flakes. In an electrochemical intercalation, the layered or 2D host must be electrically conductive or placed on a conductive substrate. Then, the host needs to be connected to a voltage source (Figure 1-5a), which can be achieved by either placing the host on a conductive substrate or attaching electrical contacts to the few-layer flake or thin film on an insulating substrate. If metal wires are deposited on the top surface of a host lattice, electrical connection may be lost during intercalation as the lattice expands and deforms the metal contacts. Thus, bottom surface placement is preferred; however, flakes can delaminate from the substrate during intercalation. Techniques for preventing delamination include better adhesion to the substrate through rigorous cleaning processes or substrate selection, depositing an inactive material using lithography techniques to ensure the flake remains adhered, or using a binder.

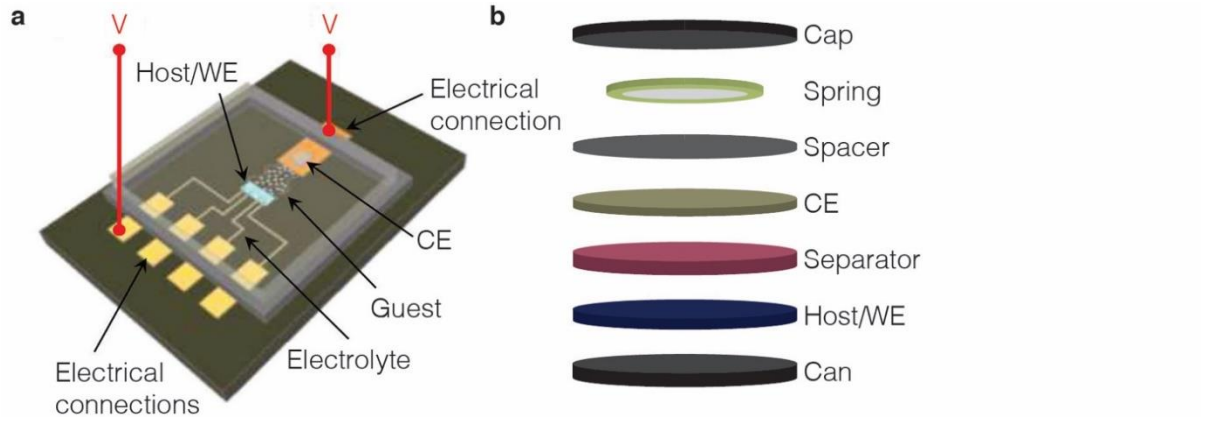


Figure 1-5: Electrochemical cell designs for in-situ studies. a) planar electrochemical cell. Reproduced and modified with permission.[8] Adapted with permission from *Nano Lett.*, 15 (10), pp. 6777-6784. Copyright 2015 American Chemical Society. b) coin-battery cell. Modified and reproduced with permission.[31] Adapted with permission from *Nano Lett.*, 15 (11), pp. 7671-7677. Copyright 2015 American Chemical Society.

As with bulk electrodes,[36,69] binders can improve the binding between host material and a substrate. However, binders, such as PVDF, can negatively impact the performance due to the resistivity and degradation of the binder with intercalation/de-intercalation cycles.[70] These binders, as well as other methods can also be used to create films for coin batteries (Figure 1-5b). An advantage of creating a thin film electrode includes the large area of sample that is available for characterization after intercalation/deintercalation. After deciding on a working electrode setup, a counter electrode should be selected such that it does not negatively affect the electrochemical cell performance through side reactions. For example, lithium metal is the counter electrode in a Li^+ battery. In a planar electrochemical cell (Figure 1-5a), the working and counter electrodes are in electrical contact through using a conductive electrolyte reservoir. It is important to note that electrolytes with high absorption coefficients or strong attenuation may hinder *in-situ* investigations in the planar cell configuration. For coin cell batteries, a permeable separator is placed between the electrodes and then the cell is filled with an electrolyte (Figure 1-5b). The entire electrochemical cell is sealed within a coin cell, often

including a spring and spacer. Due to the nature of this cell, it is not readily used for *in-situ* optical studies, but techniques that use X-rays can probe these thick cells.[71] While each of these electrochemical cells have been implemented in studying 2D intercalation, other configurations are actively being developed to enable more characterization of 2D intercalation.

Electrochemical intercalation in 2D materials and heterostructures presents interesting opportunities for interfacial studies. Interfacial engineering can be realized in vdW heterostructures and has been explored for a few combinations of TMDCs, graphene, and hexagonal boron nitride (hBN) through electrochemical intercalation.[2,3] The materials at a vdW interface can induce strain,[2] which can alter the intercalation mechanism[2] or induce more or less charge transfer to the adjacent layers of the interface[3]. The ability to intercalate thin material via interfacial structure and composition is of great interest for 2D materials, which lends to the idea of engineering interfaces to create idealized (e.g. tailored interlayer interactions, faster diffusion, desired charge transfer, etc...) intercalation mechanisms and resulting properties. This is promising for application of these structures to battery and optoelectronic technologies.

Despite the importance of electrochemical intercalation into 2D and few-layer materials, there are shortcomings of this method. Unlike gaseous or non-electrochemical methods, electrochemical intercalation requires an external voltage source to drive the reaction, which dictates specific requirements for substrate and sample fabrication. In addition, the selection of the components in an electrochemical cell are crucial to the success (and limitation) of the intercalation. The host, solvent, and concentration of the intercalant can affect the voltage window in which intercalation occurs. At more extreme voltages, decomposition

reactions can occur and negatively impact the performance with cycling. Moreover, certain electrochemical intercalation reactions only reach higher degrees of staging under inert gas conditions, and thus require more complex methods compared to other techniques. Additionally, the solvent selection is crucial to the composition of the SEI layer,[36] with some solvents resulting in SEIs of varying thicknesses. Formation of a SEI on a 2D material may lead to a substantial loss of the material and the resistive SEI formation[51] may impair the kinetic advantages of 2D intercalation. Furthermore, the guest and solvent can co-intercalate the host lattice, leading to larger interlayer spacing. As the lattice expands during intercalation, it can induce exfoliation of the material or delamination from the electrode[69], degrading the performance of an electrode. To eliminate the negative aspects of a solvent in an electrochemical cell, a solid-state electrolyte can be implemented. For example, a solid-state electrolyte with Li^+ was prepared on the surface of a 2D electrode through rapid evaporation of the solvent from the solvent/polymer/Li^+ mixture.[3] With each of these challenges, the selection of the electrochemical cell components are essential to each host/guest intercalation pair. Therefore, with these insights in this review, we especially focus on electrochemical reversible intercalation studies due to their potential applications in tunable optoelectronics and energy storage devices, but we draw expertise from non-reversible intercalation to aid in our understanding of 2D and few-layer intercalated compounds.

1.3 Structure

1.3.1 Intercalation Staging Model

Intercalation involves a balance between enthalpically favorable guest-host interactions and

enthalpically unfavorable lattice expansion and coulombic repulsion among guest species. To minimize energetic costs, the guests do not insert randomly into the gallery spaces. In many guest-host systems, guests fill an entire interlayer gap before filling adjacent layers. As intercalation progresses, guest layers are separated by fewer layers of host. These stages are denoted by the number of host layers between each layer of guest such that stage 1 is generally the upper limit of intercalation in which host and guest layers alternate (**Figure 1-6**).[36,72,73]

Staging is evidenced by multiple techniques, including electrochemical and optical measurements. Figure 7 shows an idealized galvanostatic plot for the reduction of graphite in a Li-containing solvent with a constant applied current. The flat portions of the curve occur when two or more stages are present simultaneously. The vertical portions of the graph with large changes in potential indicate the presence of a single, pure stage.[36]

The model captures the behavior of bulk graphite and many other layered solids such as TMDCs, but the model begins to change as the thickness approaches the 2D limit. A fundamental change in the structure of an intercalated material as it transitions to 2D is the departure from the bulk staging model. For example, in Li-GICs, intercalation in both bulk and 2D begins with a dilute stage 1 where guests partially fill each of the interlayer spaces until enough guests are present to complete a stage.[51,74,75] Bulk graphite transitions from dilute stage 1 (LiC_{72}) to stage 4 (LiC_{36}).[75]

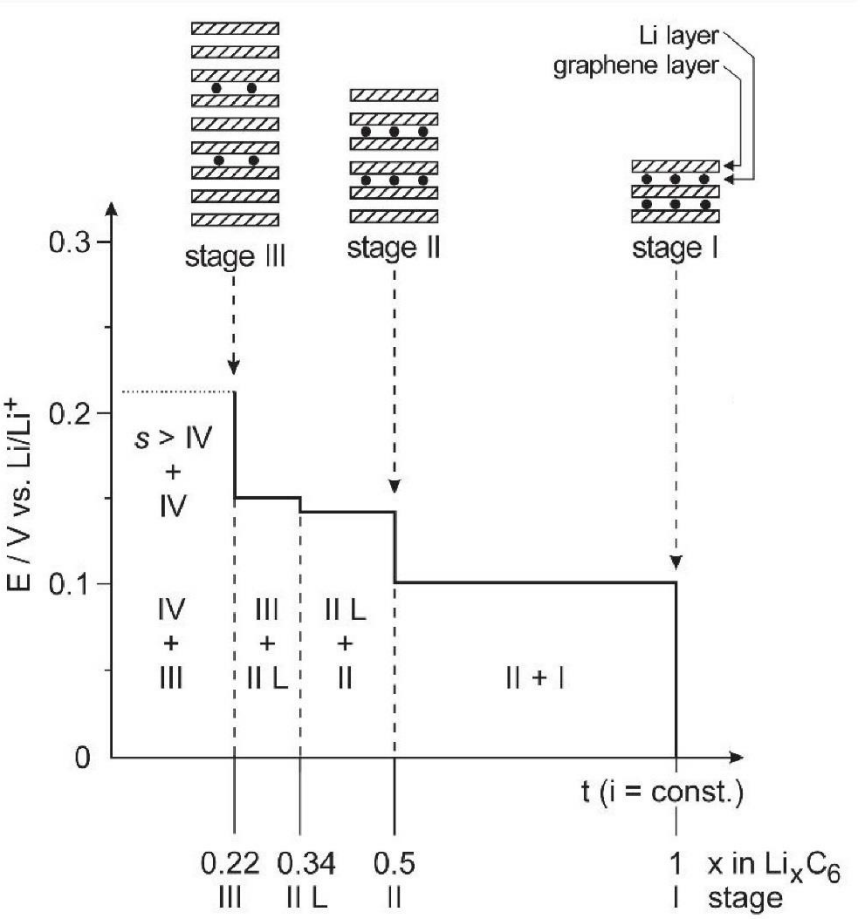


Figure 1-6. Galvanostatic curve for the intercalation of lithium into graphite. The vertical voltage drops indicate pure stage compounds. Splitting of stage 2 into two phases is due to different Li^+ packing densities. Reproduced with permission.[76] Copyright 1998, John Wiley & Sons Inc.

This sequence is disrupted when graphite has fewer than *n* layers (*n* = 5), since there are too few layers to access a stage *n*-1 GIC.[51] Cyclic Voltammetry (CV) experiments of 4-layer graphite reveal transitions only from stages 2 to 1. Increasing the FLG thickness to 6 layers allows for the formation of stage 4 as the material reverts to a more bulk-like intercalation mechanism.[51] In **Figure 1-7**, there is no splitting of the Raman G peak for 3-layer graphite (b), although this splitting is seen in thicker flakes (a). This indicates that for all phases of intercalated 3-layer compounds, each layer is adjacent to a layer of intercalated

guest.[51] The intercalated 3-layer flake transitions directly from the dilute stage 1 to stage 1. These few-layer materials also require a larger concentration of intercalants to transition from the initial dilute stage 1 phase. Relatively little is known about the intercalation mechanisms in other few-layer systems.

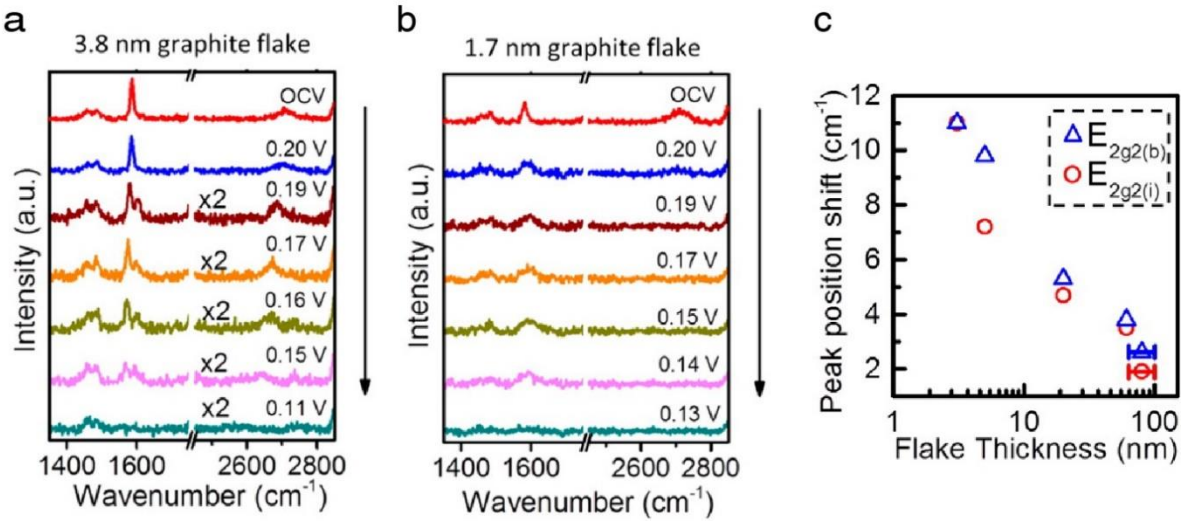


Figure 1-7. Raman spectra during lithium intercalation. a), b) Raman G peak during the lithiation of few-layer graphite electrodes. Absence of G peak splitting in b) suggests the direct transition from dilute stage 1 to stage 1 GIC. c) G peak shift as a function of flake thickness. The thinner flakes experience a greater peak shift and therefore a larger biaxial strain. Reproduced with permission.[72] Copyright 2016, ACS Publications.

1.3.2 Lattice Expansion

The most apparent change in the structure of a layered host after intercalation of a guest is the expansion of the gallery space. The volume of guest and extent of intercalation determine the size of lattice expansion, and can be monitored by X-ray diffraction and HR-TEM.[77,78]

These increases in gallery size are on the order of 10% for lithiation of TiS_2 and graphite, which present a significant increase in total material volume.[36,78] The relative increase in lattice parameter is a key figure in predicting the cyclability of an intercalation compound.

The effects of lattice expansion on material stability are also utilized in exfoliation techniques to produce 2D materials. Lithiation of graphite and TMDCs decreases the vdW binding forces and the layers can then be more easily separated by sonication.[17,79] Intercalation can yield larger scale and higher purity products than alternative oxidative methods.[80,81] The Li exfoliation of MoS_2 is particularly interesting due to the structural change that occurs from 2H semiconducting to the 1T metallic phase.[8,82]

Decreasing the thickness of the host also increases the in-plane strain of intercalated compounds. Intercalation of donors into few-layer graphite lengthens C-C bonds as antibonding states are populated. Microcrystalline graphite has an in-plane (biaxial) strain of 0.04% during lithiation, while the 3-layer graphite reaches 0.17%. The extent of strain is calculated from the G peak shift, where a larger shift relates to more biaxial strain (Figure 1-11c). The greater strain experienced by thinner electrode materials is speculated to degrade the electrode more rapidly during repeated cycling.[72]

Reducing the thickness of layered host materials produces changes in the unit cell of the material. The presence of Co^{2+} rather than Co^{3+} at the surface of 2D $LiCoO_2$, for example, contributes to disorder and an increase in the interlayer spacing.[83,84] Similar structural changes were observed for a two-dimensional TiS_2 electrode material. 2D TiS_2 has a larger c-lattice parameter of 5.80 Å, compared to 5.66 Å in bulk form, which is produced by similar surface disorder as seen in the $LiCoO_2$ case or excess Ti in the interlayer space. As a result of the differences in interlayer spacing of the host, the volume of the 2D material only increased by

2% upon lithiation, compared to 10% for the bulk.[85] The changes in the structure of these host lattices produce unique intercalation kinetics compared to the bulk.

1.3.3. Solid-Electrolyte Interphase

Electrochemical intercalation occurs when the guest species leaves the electrolyte and enters the host material at the solid-electrolyte interphase (SEI). The interphase is formed by decomposition reactions at the surface of the electrode and the deposition of the insoluble products.[86] Ideally, the initial SEI formation will create a passivating barrier to prevent further decomposition, and acts as an electronic insulator and ionic conductor between the two phases. As an ion approaches the SEI from the solvent, the ion is desolvated, inserts into the SEI, diffuses through it, and inserts into the electrode.[86] The composition of the interphase depends on the electrolyte, electrode, solvent, and any additives, and therefore the selection of each is a significant factor in determining device performance and stability. The investigation of the SEI is predominantly focused on the electrolyte reduction products at the anode, but there are reports of an interphase at cathodes as well.[87–94] Thorough reviews of interphases and electrolyte compatibility can be found here.[95,96] In this section, we discuss SEI formation primarily in the context of Li-graphite, since the system is the most well-studied to date and lays the framework for understanding the SEI in other battery materials.

The structure and electrochemical reactions at the SEI of bulk electrodes have been extensively researched, particularly in the context of batteries because ion transport through the SEI directly impacts cell performance.[87,88,94,95,97–99] The diffusion-induced stress from intercalation and deintercalation cycles causes strain on the electrode and a change in SEI morphology that produces multiple interphase growth mechanisms during the life of the cell.

These growth processes produce a spatially and chemically inhomogeneous structure. The rate of the SEI growth depends on the physical morphology of electrode particles, and impacts the performance and lifetime of a cell. The structure of the interphase can also influence the mechanism of ion transport and the kinetics of the cell.

The lattice expansion from guest insertion can cause cracking of the SEI and have significant effects on stability.[97] This cracking and healing of the SEI reduces the performance and lifetime of energy storage devices. For example, in Li-ion batteries, cell capacity is hindered by the loss of available Li during charge cycles, which occurs through multiple SEI-growth mechanisms that form insoluble Li products. In a real system with electrode expansion, SEI growth processes include: 1) initial SEI formation during the first cycle, 2) continued growth of the original SEI, 3) growth on newly exposed electrode surfaces during the first cycle after cracking, and 4) continued growth on the cracked surfaces over the lifetime of the cell.[86,100]

The structure of the SEI is typically complex, as the decomposition products are spatially inhomogeneous. The chemical composition varies through the depth of the SEI, and differences are also found between the basal plane and edges.[101] Such differences motivate a comparison of the effects of the SEI for systems in which both edge and grain boundary intercalation occur. Focused ion beam techniques provide further insight into the complexities of SEI structure by examining cross sections of electrode particles.[102] Bisecting particles after multiple intercalation cycles revealed a second type of SEI that penetrates into the bulk of the electrode, called an internal SEI. The internal SEI forms when the SEI or electrode particle cracks, exposing new surface, and leading to further SEI formation.[102] The decomposition can evolve gases, which contributes to additional stresses, cracking, and loss of Li. The outer SEI

grows continually upon cycling, while the internal SEI does not. The increased thickness of the SEI results in greater resistance and slower ion transport from the electrolyte to the electrode.[102]

The structure and growth rates of the SEI are highly dependent upon the size of active particles and morphology of the electrode. Three major attributes of the particle and electrode influence the SEI: (1) charging time, (2) voltage drop across SEI, and (3) percentage of active material near surface. For particles with a radius of less than 1 μm, the SEI growth is highly dependent on the charging time. Smaller particles require less time to reach full charge and the SEI is thinner than in larger particles.[98] For particles with a radius greater than 1 μm, however, the difference in the voltage drop across the SEI is more important to SEI growth than charging time (See Section 5.1.3). Larger particles experience a smaller increase in potential and produce a thinner SEI (**Figure 1-8**).[98] In addition to individual particle size, the surface area of the electrode also effects the SEI, as higher surface area electrodes result in the production of more SEI to passivate the electrode.[103]

The role of surface area in SEI formation is of particular significance for 2D materials. An electrochemical impedance study showed that the SEI thickness in graphite grows logarithmically, reaching a thickness of 30 nm after 500 lithiation cycles in 1-μm particles.[98] In an electrode derived from 2D materials, the SEI would then occupy a large volume fraction and reduce the electrode's capacity. Moreover, if the host electrode degraded in forming the SEI, most of a few-layer material's capacity could be lost.

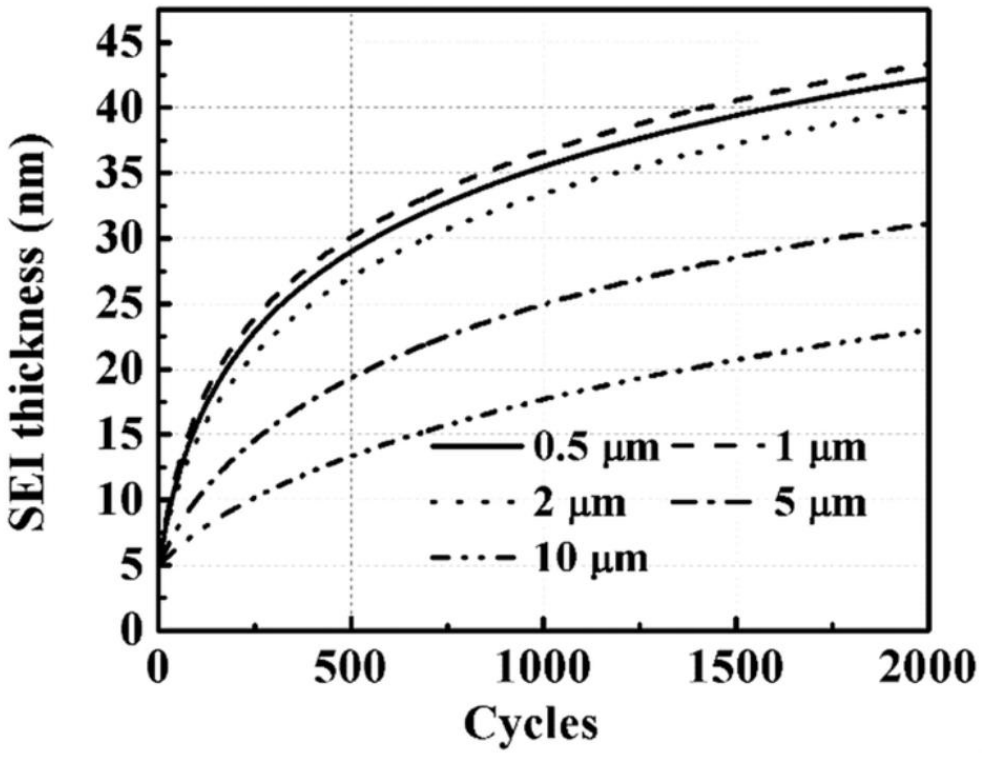


Figure 1-8. SEI thickness for spherical graphite particles of various radii during lithiation, as modeled from impedance spectroscopy. Reproduced with permission.[98] Copyright 1980, Elsevier Ltd.

The composition of the SEI depends on the depth of the film and produces a complex transport mechanism from the electrolyte to the electrode. For example, for a Li-intercalated graphite with a carbonate solvent, a two-layer model describes a porous top layer of organic Li salts, and a dense layer underneath composed of crystalline Li_2CO_3 (**Figure 1-9a**). Density Functional Theory (DFT) predictions find that Li moves through the top layer via diffusion through the pores, and then slows down considerably at the crystalline layer.[101,104,105] The interface between the porous top layer and the crystalline layer beneath is a barrier that limits the rate of Li^+ transport through the SEI. Within the lower layer of dense Li_2CO_3, Li diffuses via a knock-off mechanism in which Li^+ displaces the lattice Li. Isotope tracer measurements find that the $^6Li^+/^7Li^+$ signal peaks at this interface and then decays as depth increases for the

SEI film, which suggests that Li^+ transport is much slower in the crystalline region.[101,105] The implications of SEI structure on transport motivates further work into the structural characterization of the SEI of proposed battery systems.

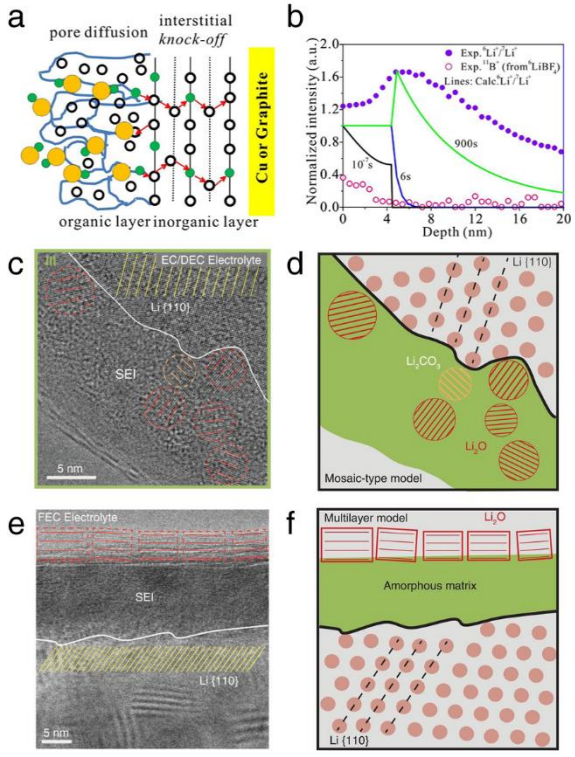


Figure 1-9. Schematic of Li diffusion through amorphous and crystalline layers of SEI. a) Yellow circles denote anions in the electrolyte, green circles are Li^+ in the electrolyte, and open circles are Li^+ already in the SEI. The blue and red path lines describe the ion transport mechanisms in each region of the interphase. b) Li isotope measurements compared to the depth of the SEI. The peak in $^6Li^+/^7Li^+$ suggests the accumulation of Li intercalant at an interface in the SEI. Reproduced with permission.[101] Copyright 2012, ACS Publications. c) Cryo-TEM and d) model of a mosaic-type SEI formed on a Li metal electrode in an ethylene carbonate electrolyte. e) Cryo-TEM and f) model of multilayer SEI after the addition of 10% fluoroethylene carbonate electrolyte. Reproduced with permission.[99] Copyright 2017, AAAS.

The structural complexity of the SEI and its effects on cell performance make the development of characterization and imaging techniques imperative to battery technology. The high reactivity and air-sensitivity of electrode, electrolyte, and SEI materials create a challenge

to experimental investigation of SEI structure. Recent advances in cryo-electron microscopy provide a solution to the atomic-scale imaging of the electrode and SEI.[99] For an ethylene carbonate electrolyte and a Li metal electrode, a mixture of amorphous and crystalline domains was observed in agreement with mosaic-type models of the interphase from the 1990s (Figure 1-9b,c).[99,106] The introduction of 10% fluoroethylene carbonate drove the formation of more defined layers of amorphous and crystalline components.[99] The implementation of advanced characterization technologies will be critical in the understanding of electrode material behavior and failure mechanisms. The increased effects of SEI structure and processes on high surface area materials suggests that consideration and design of the interface is even more important in 2D material electrodes.

Transitioning to 2D also affects the structure and growth rates of the SEI. Growth of the SEI layer is accompanied by a decrease in the capacity of the cell, as the electrolyte decomposes on the surface of the electrode in a complex mixture of products. These commonly include inorganic salts that irreversibly remove intercalant from the electrolyte.[96,97,107] As discussed in Section 4.3, smaller particles charge more quickly and have thicker SEI layers compared to larger particles.[98]

The relationship between particle morphology and SEI growth is more complicated for 2D flakes than spherical particles because of the structural anisotropy of 2D materials.[73] Thinner and narrower flakes are more reactive than larger flakes due to the increased surface area and edge defects.[73,108] The dependence of SEI growth rate on particle dimension suggests that consideration and investigation of electrolyte compatibility and the use of stabilizers becomes even more important for nanostructured electrodes, particularly because a large

proportion of a few-layer flake can be converted into SEI.[96,109]

1.4 Electronic Properties

Upon transitioning from bulk to an atomically thin monolayer, novel electrical properties emerge. Thus, it is important to review the progress that has been made in bulk to understand the electronic changes that occur in 2D intercalated materials. Here we revisit several important discoveries in the electrical properties of bulk intercalation compounds and discuss findings that are relevant to their 2D counterparts.

Early investigations into the electronic properties of GICs utilized polycrystalline graphite from natural sources, which have complex microstructures.[110] Due to the non-uniform orientations of the specimens, experimental results varied widely and were often not reproducible. In 1960, HOPG was synthesized for the first time.[111] Because of its simpler structure and higher purity, the discovery of HOPG allowed researchers to carefully probe the electronic structure of GICs. This development opened new avenues of research into the electrical properties and rapidly established the general character of GICs as metallic.[29,112] With this discovery, the next challenge was to explain the origin of the metallic behavior and its dependence on the intercalant. Such investigations have expanded well beyond graphite to include TMDCs, black phosphorus, MXenes, and others. Collectively, most studies have explored at least one of three areas: charge transfer in donor and acceptor compounds, electronic structure, and conductivity, including superconductivity. As many of these findings can be extrapolated to 2D materials, we will first outline the key conclusions for bulk materials before highlighting the unique electronic properties of 2D intercalation compounds.

1.4.1. Charge Transfer

In intercalation compounds, charge transfer (CT) is an important driving force for the insertion of donors and acceptors into layered materials. Thus, a deeper understanding of CT is needed to rationalize the chemical and physical properties of intercalated materials. Experimentally, CT is often quantified by electrochemically intercalating the host. This calculation assumes that the charge developed on the host material is equal to the charge that flows through the circuit – an assumption that has been challenged by both theory and experiment, as we will discuss later.

To indirectly probe the deep bulk or surface CT, there are several methods that can be paired with an appropriate model. In graphitic materials, the in-plane C-C bond lengths (d_{cc}) of graphite are directly related to the amount of charge transferred from the intercalant. Thus, diffraction can be used to estimate or even quantify CT. In their X-ray diffraction studies of stages 1-6 of K-GICs, Nixon and Parry reported that as intercalation proceeded, d_{cc} increased relative to that of pure graphite by 0.8 %.[61] Kamitakahara later performed *in-situ* neutron diffraction during the D_2SO_4-graphite intercalation and measured the corresponding shift in d_{cc}.[113] They found that d_{cc} contracted by 0.3 % as the intercalation progressed and that this correlated with the amount of charge transferred to the graphite. Whereas X-ray diffraction and neutron scattering probe CT at depths on the order of microns, Raman scattering can explore near surface properties. To confirm the results of neutron diffraction, Eklund *et al.* studied the surface CT of H_2SO_4-GIC through *in-situ* Raman scattering.[114] Their findings indicated that as charge is transferred to the graphite layers, d_{cc} contracts. This contraction stiffens intra-plane bonds and causes high frequency graphitic phonons to shift to higher energies. Although experimental Raman data offered insight into the effect of intercalation on

the intra-plane phonons of graphite, a model was critical to convert phonon frequency to a quantitative measure of staging. Leung and Dresselhaus developed a general model to predict the phonon-dispersions for both donor and acceptor GICs of any stage.[115] **Figure 1-10** shows the phonon dispersion and density of states for stage 1 and 3 donor and acceptor compounds. Based on the degree of staging within the material, the frequencies of the bounding and interior layers of graphite can be calculated.

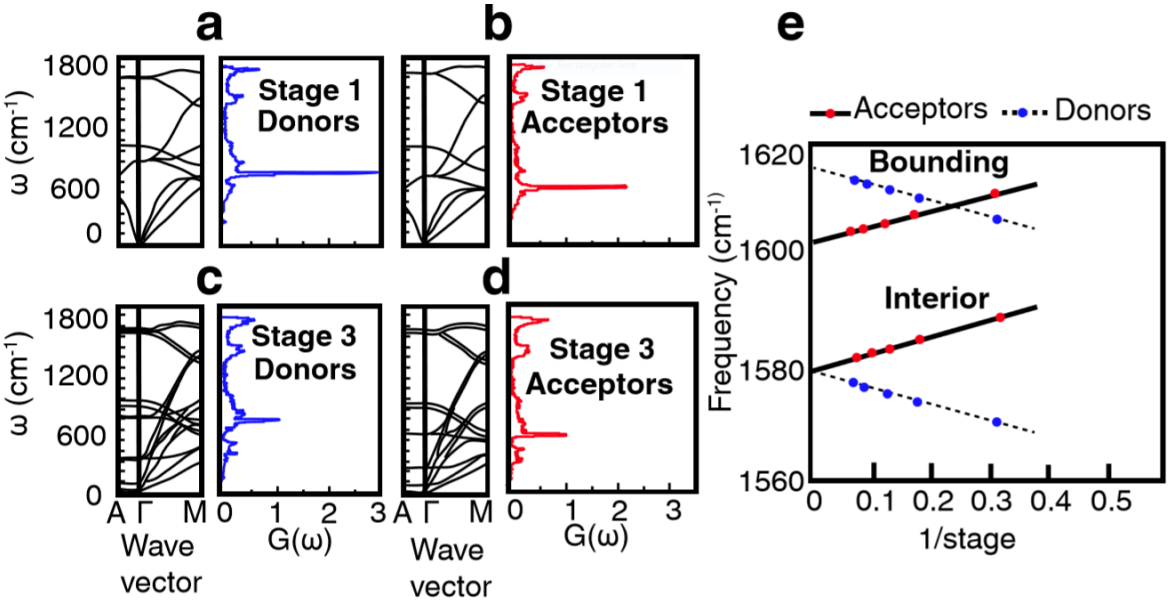


Figure 1-10. Phonon-dispersion and the corresponding DOS plots for stages 1 a) and 3 c) donor-GICs and stages 1 b) and 3 d) acceptor-GICs, based on the model proposed by Leung and Dresselhaus. The DOS shows a strong feature near 600 cm^{-1} for a)-d), which comes from the high DOS near the Brillouin zone edges. Upon intercalation, the intensity of this peak increases with higher degrees of staging. e) The vibrational frequencies of the Raman-active E_{2g} mode for the bounding and interior graphite layers depend on the degree of staging. The solid red circles represent the calculated values for acceptor compounds, while the blue markers represent the values for donors. The solid and dashed lines show the linear correlation between the model developed by Leung and Dresselhaus and the experimental data. For acceptors, as the compound moves toward a higher degree of staging (larger reciprocal stage value), the frequency increases. In donor compounds, a higher degree of staging, results in a lower frequency. Modified and reproduced with permission.[115] Adapted and Reprinted Figure with permission from M. Leung, S.Y., Dresselhaus, G., Dresselhaus, Phys. Rev. B **1981**, 24, 6083. https://doi.org/10.1103/PhysRevB.24.6083. Copyright 1981, American Physical Society.

These findings revealed a general trend for d_{cc} for both donor and acceptor intercalation systems that has been described by MO theory[116], as well as the tight-binding model[117] and DFT calculations[118]. Based on the diffraction measurements by Nixon and Parry[61], Pietronero and Strässler proposed a universal model to estimate the degree of charge transfer as d_{cc} changes.[117] However, at the time of the study, there were not sufficient experimental diffraction data on GICs to verify their calculations. In a later DFT investigation, Chan *et al.* calculated the d_{cc} as a function of charge transfer per atom for both acceptors and donors.[118] Their results showed good agreement with experimental values, and confirmed that a general model exists to estimate CT from contraction or expansion of d_{cc}. In addition, this work also provided insight into how CT influences other properties, such as phonon frequencies or electronic wavefunctions.

To summarize the general trends revealed by these studies: donors such as potassium increase the antibonding character of the graphite bands, weakening bonds, and increasing d_{cc}. Acceptors, such as bisulfate, increase the bonding character of the graphite bands, strengthening bonds and decreasing d_{cc}. More sophisticated models, which take into account the in-plane electrostatic repulsion that accompanies intercalation of both donors and acceptors, give a nearly quantitative agreement to experiment.[117,118]

For donor-type GICs, the general mechanism for CT is fairly well understood.[119] The intercalant bands overlap with the graphite π bands and, as electrons are transferred to the graphite, the Fermi energy shifts to accommodate the added charge. Since the intercalant energy levels overlap fully with graphite's continuum of states, the intercalant levels hybridize strongly with those of graphite. In TMDCs, the transition metal d-bands are the lowest

unoccupied energy levels and can range from empty to partially filled.[120] Upon intercalation, electrons are primarily added to the d-band.

Despite the relative simplicity of the CT mechanism for donor complexes, determining the amount of charge transferred to the host material is more complicated and depends on the intercalant-host band overlap.[116] In particular, the position of the intercalant bands with respect to E_F tends to determine whether a guest species will transfer all or part of its charge to the host. To illustrate the complexity inherent to calculating the degree of CT, we discuss two bulk alkali metal-GICs: LiC_6 and KC_8, which transfer full and partial charge respectively.

When Li intercalates into graphite, one electron is transferred for every Li atom within the layer, since the 2s orbitals of Li do not overlap with graphite's E_F. Although this phenomenon had been previously predicted computationally,[121–123] angle-resolved photoemission spectroscopy (ARPES) experimentally demonstrated full CT from Li to the graphite lattice.[124] **Figure 1-11** shows the photoemission spectrum, DOS, and calculated band structure for LiC_6. The total yield from the photoexcitation of the Li 2s orbital exhibits two peaks, which align with the DOS in the calculated band structure (from Γ to A). It is also similar to the absorption spectrum of Li (2s) and indicates that the 2s orbitals of Li are unoccupied in LiC_6.

In the case of KC_8, however, the intercalant bands lie very close to E_F, making the degree of CT difficult to determine. In the early 1980s, Zanini and Fischer measured the polarized reflectance of stage 2 KC_{24} and observed full CT from K to the graphite layer.[125] Oelhafen contested this result with UPS measurements showing that the K 4s energy levels lie close to the Fermi level and demonstrated partial charge transfer in KC_{24}.[126] Several years later, a theoretical study by DiVencenzo and Rabii calculated the K 4s energy levels to lie close

to the Fermi level and also supported the idea of partial charge transfer in potassium-intercalated graphite.[127] An alternative yet complementary perspective to this debate may be found in an earlier study of the electronic structure of KC_8 by Inoshita *et al*.[128] **Figure 1-12** shows the calculated and experimentally determined DOS plot for KC_8. Near E_F, up to 50% of the DOS is derived from donor states, and there is strong hybridization between the graphite and donor levels. Just below E_F, however, the DOS is almost purely graphitic in character. These observations indicate that hybridization between the donor and graphite depends strongly on energy (y-axis of Figure 1-13).

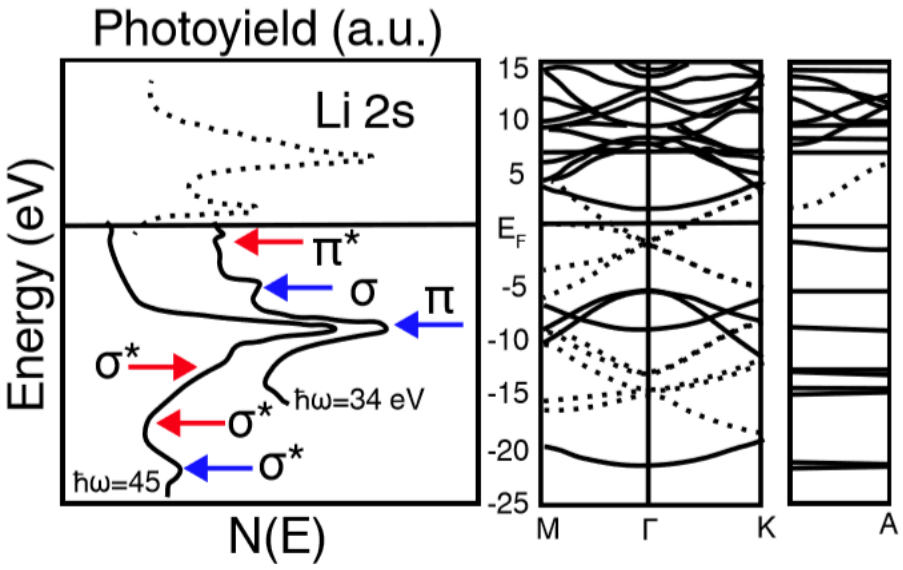


Figure 1-11. Band Structure and Emission spectra for Li-intercalated graphite. Left Upper panel: Core-threshold photoyield spectrum for LiC_6 aligned with the theoretical band structure (Right Panel). The dotted-line shows the total yield from the excitation of the Li s orbital in LiC_6. The two peaks align with the DOS maxima in the band structure. The Li 2s band is not occupied since there is no evidence of absorption at E_F. **Left Lower Panel:** The normal-emission spectra aligned with the calculated band structure for LiC_6. The graphite-like bands are denoted by blue arrows, whereas back-folded bands are represented by red arrows. Right Panel: Calculated band structure of LiC_6. The solid black lines represent the bands of the original graphite. The dotted lines represent the back-folded bands. Modified and reproduced with permission.[124] Adapted and Reprinted Figure with permission from J.

E. Eberhardt, W., McGovern, I.T., Plummer, E.W., Fisher, *Phys. Rev. Lett.* **1980**, *44*, 200. https://doi.org/10.1103/PhysRevLett.44.200. Copyright 1980, American Physical Society.

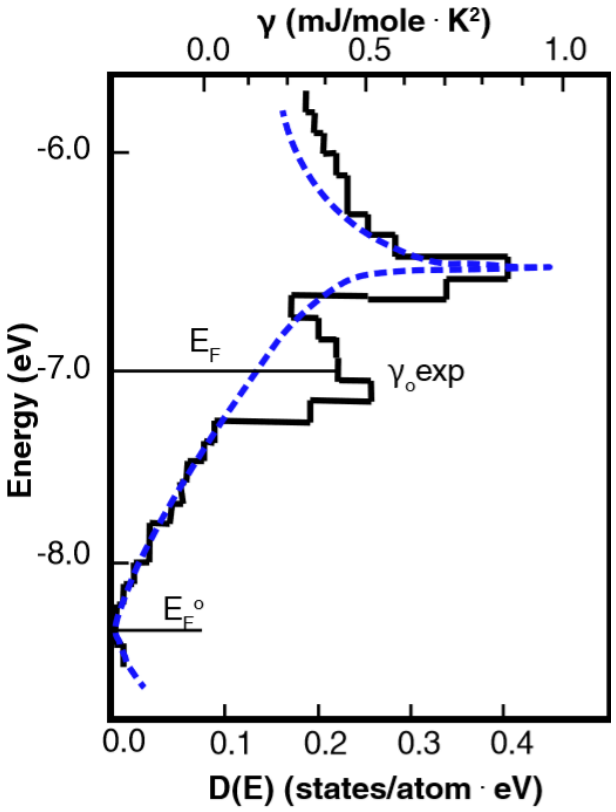


Figure 1-12. The density of states based on the calculated band structure of KC_8 (solid black line) and density of states based on the rigid band model of 2D graphite (dashed blue line). At E_F, there is a large peak resulting from the strong hybridization of the potassium and graphite bands. Adapted and reproduced with permission.[128] Copyright 1977, Physical Society of Japan.

In addition to electron donors, acceptor-type molecules and ions are known to intercalate into graphite. Elucidating the CT mechanism for graphite-acceptor compounds was complicated by the range of intercalants that fall into this category, including halogens, acids, and oxides. Moreover, the earliest proposed mechanisms for CT in acceptor GICs largely ignored the relative positions of host and intercalant bands, focusing instead on oxidation states and degree of charge transfer.[119] Eventually, several important models of charge transfer emerged, including band overlap, disproportionation, and island formation. The band overlap

models consider energetic factors, while disproportionation and island formation describe the dynamics of intercalation.

In 1985, Dresselhaus *et al.* were the first to consider band effects in the CT mechanism for acceptor compounds.[129] To explain CT in the Br_2-GIC system, they proposed a charge transfer mechanism based on the 2D π band structure generally characteristic of acceptor intercalants. Their model suggested that antibonding levels of the intercalant hybridize with the antibonding graphitic π-energy levels. This coupling causes bonding and anti-bonding interactions; the new bonding state accepts electrons and the Fermi level drops. If the bonding interaction is derived primarily from the graphite, then less charge is transferred to the intercalant. This explanation of band structure successfully explained the fractional CT that typically characterizes acceptor-type compounds.

Charge transfer through disproportionation in GICs involves a simultaneous oxidation and reduction of the intercalant, and occurs in systems such as $SbCl_5$, AsF_5, and HNO_3. This reaction mechanism was recently revisited through *ab initio* simulations in the context of doped graphene.[130] **Figure 1-13** illustrates the proposed doping mechanism for the $SbCl_5$-graphene system. When an acceptor molecule is inserted between the layers of graphite, there is incomplete charge transfer, which destabilizes the intercalant molecules. The acceptors then disproportionate into more stable products that inject holes into the graphene layers (Figure 1-14).

Island formation CT is another mechanism that occurs when the GIC structure is incommensurate (*e.g.* in transition metal chloride-GICs). In this system, there is a preferred minimum energy state for the intercalant species within the graphite lattice, typically either above or below the center of the hexagon. As intercalant density increases within a layer, guest

molecules are forced to occupy unfavorable sites within the layer. Eventually, the lattice mismatch between the graphite and the intercalant becomes significant enough that the domain terminates, forming an island of intercalants that transfer charge to the graphite. If intercalation proceeds, it may do so with a different intercalant composition to minimize strain to the lattice. For example, in the intercalation of $NiCl_2$ into graphite in the presence of excess chlorine gas, Cl_2 (g) first oxidizes $NiCl_2$ to form $NiCl_x$ (where $x > 2$) and islands of $NiCl_x$ nucleate at the edges of the graphite before diffusing to the center of the graphite layer. Surrounding each domain, there is an excess of chloride anions, which facilitate the transfer of electrons from the adjacent graphene layers to reduce $NiCl_2$.[131]

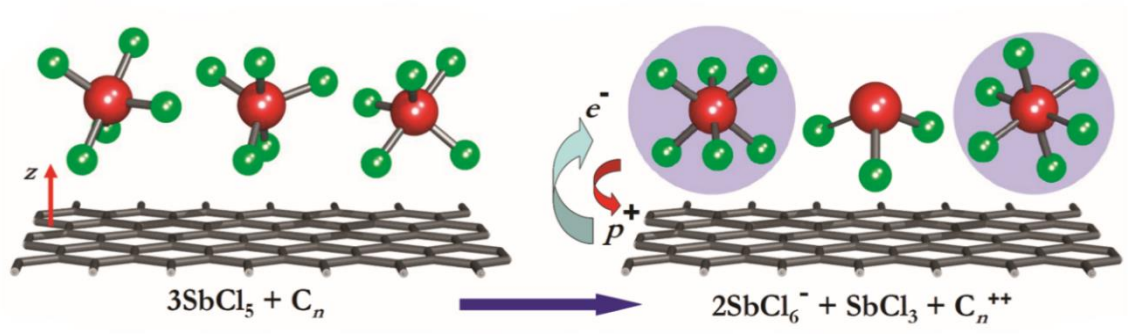


Figure 1-13. The representative mechanism of disproportionation in GICs, using $SbCl_5$ (Sb: red; Cl: green), as an example. Upon insertion into graphite, the molecular intercalant ($SbCl_5$) partially transfers charge to the graphite layers, and is destabilized. $SbCl_5$ then dissociates into $SbCl_6^-$ (highlighted in blue) and $SbCl_3$. $SbCl_6^-$ absorbs minority carriers (electrons) from graphite and transfers holes, which results in a downshift in the Fermi level. Reprinted with permission[130] from ACS Nano **2011**, 5(4). Copyright 2011, American Chemical Society.

Charge transfer in few-layer materials has also been demonstrated with donors and acceptors. Because of its sensitivity to surfaces, Raman spectroscopy is a valuable technique for quantifying CT in 2D materials. The G peak of bulk graphite compounds can be analyzed

to investigate the local environment of each layer. In this analysis, the shift of an individual layer depends on the degree of staging within the material. For example, there is stronger doping in a graphene layer sandwiched between two intercalant layers (Stage 1) compared to a graphene layer adjacent to one graphene and one intercalant layer (Stage 2). Stronger doping corresponds to a larger shift in the Raman G peaks.[132–134]

Jung *et al.* demonstrated this principle through their analysis of Br_2 and I_2 adsorbed or intercalated into one layer (1L) to four layer (4L)- graphene.[18] The resulting Raman spectra for Br_2-and I_2-intercalated graphite are shown in **Figure 1-14**b and c respectively. Upon intercalation with Br_2, the peak for 2L, 4L, and thicker nL shifts close to 1612 cm^{-1}, which is similar to the shift reported for bulk.[135] For 3L, the peak is asymmetric since there are two sets of non-equivalent graphene layers. The higher energy peak (1620 cm^{-1}) indicates stronger doping and represents the outside graphene layers (Figure 1-14a). The peak that occurs at 1612 cm^{-1} is the expected shift for the two interior layers of graphene. Interestingly, the G-vibration for 1L graphene occurs near 1624 cm^{-1}, a shift which the authors note is 30% higher than values obtained by top gating.[132] The large blue shift is due to the strong charge transfer between the adsorbed Br_2 and the graphene layer. The 3L case presents an interesting opportunity to investigate the electronic qualities of an asymmetric intercalation compound and should be explored further.

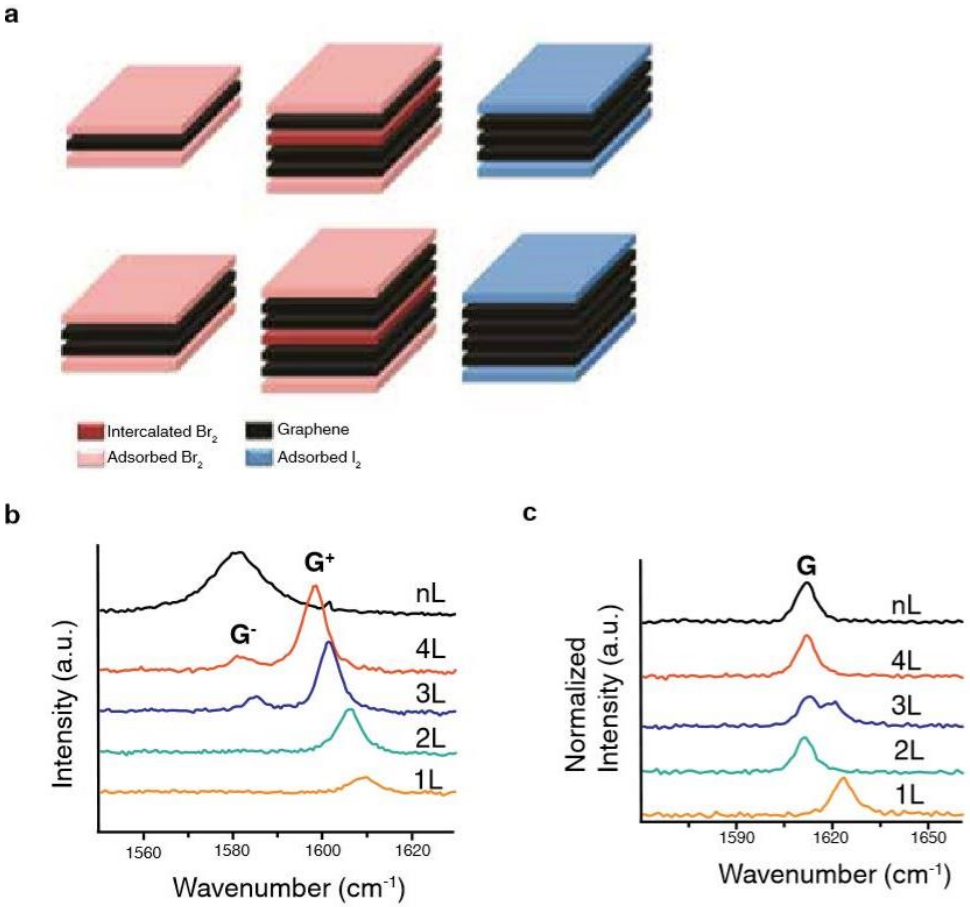


Figure 1-14. Halide intercalation into graphite. a) Left: 1L-4L FLGs exposed to Br_2. All of the structures have layers of Br_2 adsorbed (light pink) to the surface of FLG. Layers of intercalated Br_2 (dark pink) are present only in 3L and 4L structures, since Br_2 cannot intercalate past stage 2. Right: 3L and 4L FLGs exposed to I_2. Unlike Br_2, layers of I_2 (blue) do not intercalate, but rather adsorb to the surface. b) The vertically displaced Raman spectra for 1L-4L and bulk graphite (nL) exposed to Br_2 shows a large blue shift in the G-peak due to strong charge transfer. A doublet appears for 3L, indicating asymmetric intercalation and charge transfer, as shown in a). c) The vertically displaced Raman spectra for 1L to 4L and nL exposed to I_2 vapor. For 1L and 2L, there is one peak, which indicates that I_2 has adsorbed to the layers. The G-peak shifts to higher energies for I_2, but the magnitude of the shift is less than that observed for Br_2, which indicates that the degree of charge transfer is weaker in the case of I_2 doped FLG. Reprinted with permission.[18] from *Nano Lett.* **2009**, *9(12)*, 4133. Copyright 2009, ACS Publications.

Although the Br_2-few layer graphene intercalation compound exhibits strong CT, it cannot achieve a stage 1 structure. Thus, in an effort to prepare fully intercalated few-layer GICs, other groups investigated the 2D counterparts of bulk GICs that are known to reach stage

1. Zhan et al. reported the first synthesis of fully intercalated $FeCl_3$-GIC and analyzed its CT properties through Raman spectroscopy.[136] **Figure 1-15a**-c show the proposed structures of the intercalated FLG. In the diagram, the yellow layer represents graphene that is adjacent to a single intercalant layer while the orange layer shows graphene adjacent to two intercalant layers. To confirm these structures, the Raman spectrum for each compound was obtained (Figure 1-15d). For 1L and 2L, there is only one G peak at 1605 cm^{-1} and 1612 cm^{-1} respectively. At 3L and 4L, however, the G-peak splits into two peaks (labeled G_1 and G_2) since there are now two sets of graphene layers (Figure 1-15a-c) each in a different local chemical environment. In addition, the sharp 2D peak at 2700 cm^{-1} in the Raman spectra reveals that the electronic coupling between the graphene layers is lost. Therefore, the graphene layers have an electronic structure similar to single layer graphene. This loss of electronic coupling was not evident in the Br_2-few layer GIC since there was no evidence of a 2D peak.

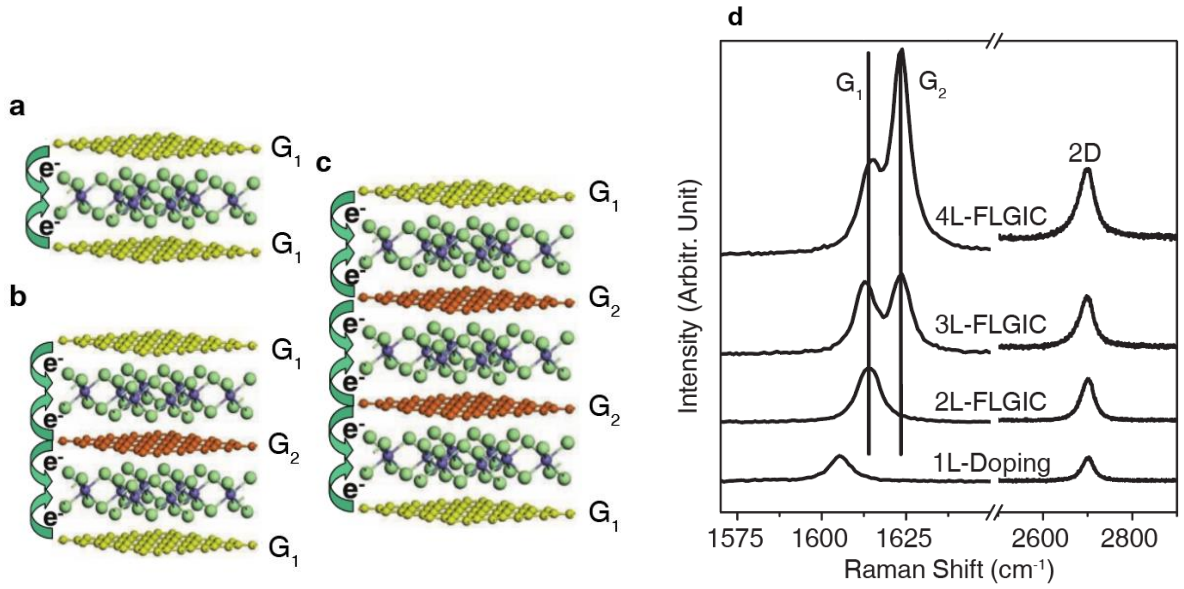


Figure 1-15. $FeCl_3$ intercalation into graphite. a)-c) show 2L, 3L, and 4L graphite intercalated with $FeCl_3$. The yellow graphene layers are only in contact with one layer of intercalant and are represented by the lower energy Raman G_1 peaks in d). The orange graphene layers are sandwiched between two intercalant layers and the Raman shifts are given by the higher energy G_2 peaks. Electrons are transferred from the graphene layers to $FeCl_3$. For all of the GICs, the peak intensity increases with the number of layers. Reproduced with permission.[136] Copyright 2010, John Wiley & Sons Inc.

1.4.2 Conductivity

Upon intercalation, charge transfer from the intercalant species to the host material shifts E_F, which can have a significant effect on the electronic structure, and therefore the conductivity and optical properties of the host. Since the effect of intercalation on the electronic structure of bulk materials has been detailed in several excellent reviews,[120,137] here we highlight the general trends for graphite.

Graphite has strong in-plane bonding from the covalent interactions of the 2s, $2p_x$, and $2p_y$ carbon orbitals. Near E_F, however, the band structure is dominated by the π states,

which are derived from the carbon $2p_z$ orbitals (**Figure 1-16a**). Undoped graphite is a semimetal with a vanishing DOS at the Fermi level. Upon insertion of a donor species, electron density is donated to the conduction band and E_F shifts up in order to accommodate the added charge. In contrast, acceptor intercalants remove electrons from the valence band, and therefore lower E_F. (Figure 1-16b). In addition to characterizing the Fermi level shift, it is important to note other aspects of the electronic structure of GICs, specifically the DOS at E_F, the total and local DOS of the valence and conduction band, and the electronic character close to E_F.[137] Figure 1-16c shows the UPS measurements for CsC_8 GICs.[126] From the spectrum of pristine HOPG, four distinct peaks appear at 3.0, 4.7, 8.0, and 12.3 eV.[126] These structures reflect the π- and σ-bands of the graphite band structure. Close to E_F, however, the spectrum of the donor-GIC differs significantly from that of HOPG, with an intense peak emerging upon intercalation. This feature is primarily derived from the s-orbitals of the alkali metal. The large contribution to the DOS near E_F indicates that hybridization between the donor and the graphite depends strongly on energy. Below E_F, hybridization is negligible and the DOS is almost purely graphitic in nature.

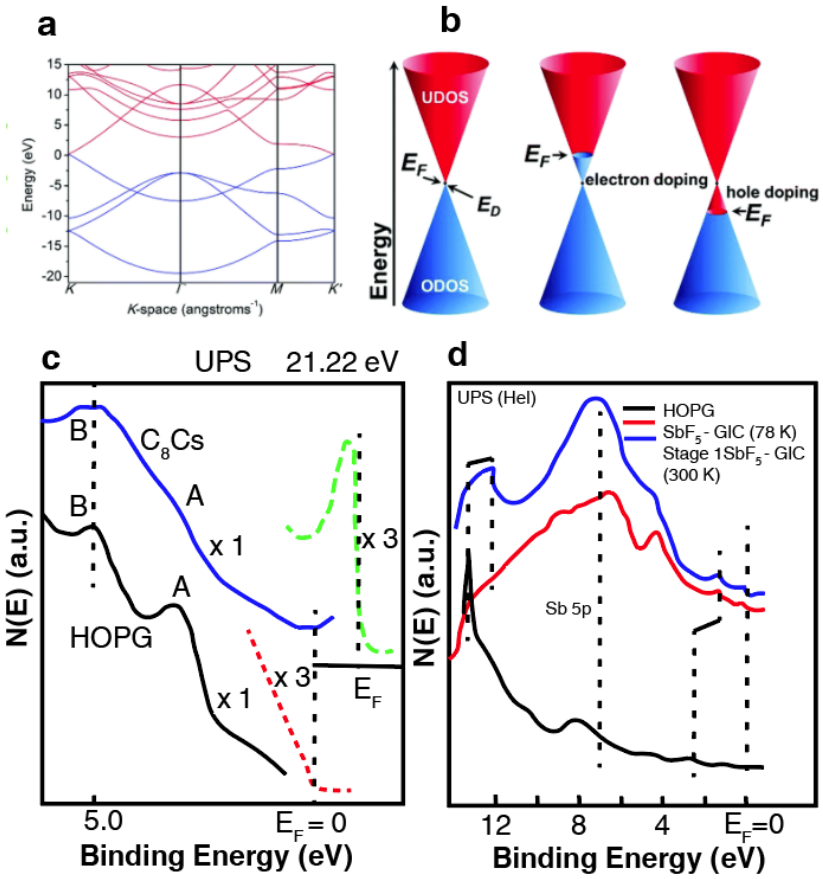


Figure 1-16. UPS for donor and acceptor species. a) Calculated band structure for graphene. b) Illustration of the Dirac cone to show the linear dispersion of the conduction and valence bands at the K-point in a). E_F shifts to lower energies when graphite or graphene is hole-doped (acceptor). Electron-doping (donor) shifts E_F to higher energies. Reproduced with permission.[138] Copyright 2014, Royal Society of Chemistry. c) Ultraviolet Photoemission Spectroscopy (UPS) measurements of Cs-intercalated graphite (donor) compared to HOPG. Adapted and reprinted figure[126] with permission from P. Oelhafen, P. Pfluger, E. Hauser, H. J. Guntherodt, Phys. Rev. Lett. **1980**, 44, 197. https://doi.org/10.1103/PhysRevLett.44.197. Copyright 1980, American Physical Society. d) UPS spectra of SbF_5-GIC (acceptor) compared to HOPG. Adapted and reprinted by permission[139] from Springer. R. Schlögl, in Graph. Intercalation Compd. II Transp. Electron. Prop., **1992**, pp. 53–102. Copyright 1992, Springer.

In contrast to donors, acceptor intercalants lower E_F by removing electrons from the valence band. (Figure 1-16b). Although obtaining reliable photoemission measurements of acceptor compounds traditionally presented experimental challenges, R. Schlögel obtained

UPS spectra for a series of stage 1 acceptors, including $AlCl_3$-, $CuCl_2$-, and SbF_5-GICs.[139] Figure 1-16d shows a representative spectrum for stage 1 SbF_5-GIC. Near 2.8 eV, there is a peak in pristine HOPG that has shifted to lower binding energies in the stage 1 acceptor-compound. This change indicates that HOPG undergoes a metallic transition, as electron density is removed from the valence band. In addition, the secondary electron emission structure shows a shift in the peak at 8.6 eV (HOPG) to 7.2 eV (stage 1), further indicating that E_F has shifted to lower energies.

Conductivity in intercalation compounds has been studied in bulk graphite[33,140–143] , as well as in TMDCs[120,144–146], and other layered materials[147,148]. Intercalation offers an attractive pathway to enhance the conductivity of layered materials by increasing the carrier concentration through CT. Developing materials with conductivities comparable to that of copper[33], while reducing the mass density is essential for a variety of technological applications, such as transparent conductors or electrically tunable displays.

Electronic transport in graphite is characterized in terms of its large in-plane carrier mobility (1.3×10^5 cm^2 V^{-1} s^{-1})[149]. However, graphite has a moderate basal plane conductivity (2.5 x 10^4 S/cm)[149] due to a low carrier concentration. In 1977, Vogel and coworkers synthesized AsF_5 and SbF_5 acceptor GICs with remarkably high electrical conductivities[140], on the order of 10^6 S/cm, which is close to that of pure copper (5.85 x 10^5 S/cm). This observation stimulated intense experimental and theoretical investigations into the conductivity of other GICs, as researchers attempted to explain and achieve comparable electrical conductivities in other intercalated materials.

Intercalation usually increases the carrier concentration of graphite, since the intercalant layer injects carriers and graphite's DOS increases as either holes or electrons are

added. In general, intercalated materials possess a high basal plane electrical conductivity (σ_a) and a relatively low c-axis conductivity (σ_c).[29] The magnitude of the conductivity and anisotropy depend on the nature of the intercalant. For both donor-and acceptor-GICs, there is an increase in σ_a with respect to the in-plane conductivity of pristine graphite. Since most intercalant layers have low carrier mobilities, they do not contribute appreciably to σ_a.[121,122]

In GICs, charge screening by the host limits the amount of charge transferred to bounding layers, which are adjacent to the guest species. Bounding layers have significantly higher values of σ_a because the screening length is approximately the width of a single layer of graphite.[150,151] However, interior layers that are not adjacent to the intercalant, can make a significant contribution to the conductivity when CT is accompanied by a decrease in the carrier mobility of the bounding layers.[20] Whereas acceptor compounds typically reach their maximum conductivity for stage 2,[20] the maximum conductivities of K-, Rb-,and Cs-GICs occur with stages 3-5.[152] This finding is consistent with the degree of hybridization of graphite with donors, which leads to a decrease in mobility. Although acceptor-GICs have lower carrier concentrations, they have higher conductivities due to the decrease in mobility that generally occurs in donor systems.[129]

Conductive, flexible, and mechanically strong, few-layer graphene is a candidate material for developing ultrathin optoelectronic devices. Despite its high mobility, however, pristine FLG has a sheet resistance (R_{sq}=30 Ω/□)[153,154] that is three times higher than that of commercial indium tin oxide (ITO).[155] This resistivity prevents FLG from being employed in many medium-to high-current device applications. Several groups doped graphene sheets with nitric acid[153,156] in an attempt to reduce R_{sq}. Although the transparency of graphene increased to 97.7 %, R_{sq} increased to 125 Ω/□ for a single layer of graphene, since the methods

of stacking resulted in defects within the graphene sheets. To improve R_{sq} in FLG, Khrapach et al. intercalated FLG with $FeCl_3$ through the two-zone vapor transport method and measured the corresponding electrical properties as a function of temperature and sample thickness (**Figure 1-17**a).[7] Pristine FLG demonstrates non-metallic characteristics (Figure 1-17b), with resistance decreasing as temperature increases. In thicker intercalated samples (3L-5L), however, the material behaves as a metal, with higher temperatures resulting in increased resistance. The decrease in resistivity with heating observed for 2L $FeCl_3$-FLGIC is due to the partial deintercalation that occurred during the conductivity measurements. In addition to the resistivity, Hall coefficient measurements indicated that the intercalation compound possessed superior mobilities and charge densities that were higher than those obtained by both liquid electrolyte[157] and ionic gating[158].

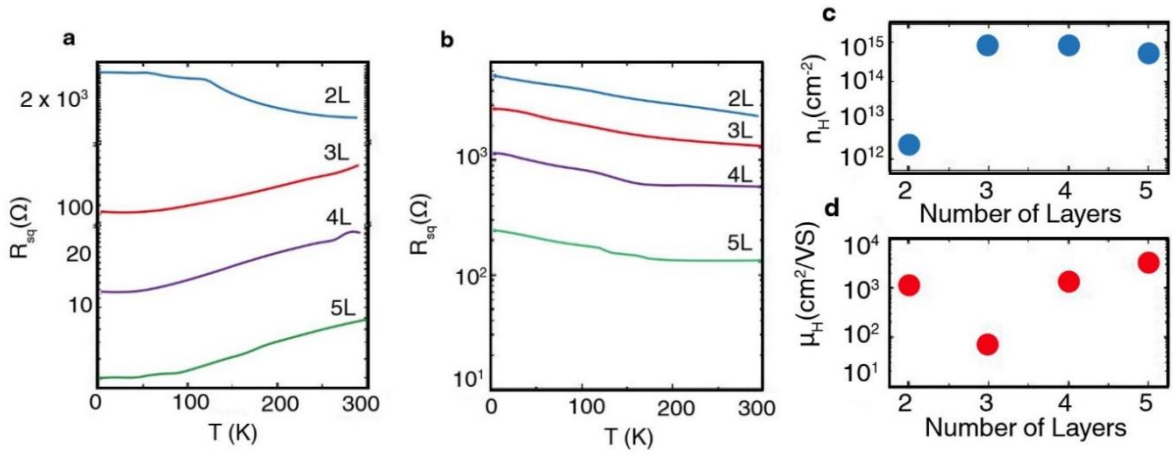


Figure 1-17. Thickness dependence of Rs for GICs. a) R_s as a function of temperature for $FeCl_3$ –FLG from 2L-5L. R_s increases with T for 3L-5L $FeCl_3$-FLGs. For 2L, R_s shows a continual decrease from 0 K-300 K. b) R_s as a function of temperature for pristine 2L-5L FLG. Thickness dependence of the carrier concentration c) and mobility d) for $FeCl_3$ –FLG. Reproduced with permission.[7] Copyright 2012, John Wiley and Sons Inc.

1.5 Optical Properties

The optical properties of a material depend strongly on its electronic structure. In

general, information about the properties of intercalation compounds is derived from the electronic structures of both the host material and the intercalant. Bulk layered materials with metallic characteristics have a high concentration of free charge carriers, which interact strongly with light. Therefore, optical studies can reveal subtle yet significant differences, such as free carrier effects or optical anisotropy, in the electronic responses of pristine and intercalated compounds.

Optical reflectivity and transmission are two fundamental methods of determining the dielectric constant of a material. These techniques often provide information about the degree of charge transfer in an intercalated material and its electronic band structure. A key feature of frequency-dependent reflectance measurements is the plasma frequency (ω_p), which occurs when the frequency of light exceeds the frequency at which the free carriers can respond. At this characteristic frequency, the real part of the dielectric becomes zero and the material switches from a reflecting metal to a transmitting dielectric. In compounds with a high degree of intercalation, the Drude model can describe the plasma frequencies determined from transmission and reflection measurements: [20]

$$\omega_p{}^2 = \frac{4\pi n_c e^2}{\varepsilon_L m}$$

where e is the charge of a single carrier and m is the effective carrier mass. In reflectivity measurements, there is also a dramatic decrease in reflectance, known as the plasma edge, that is observed when ω is less than or equal to ω_p. Since the number of free carriers is proportional to ω_p, monitoring shifts in the plasma edge provides insight into changes in the degree of charge transfer and free carrier density within intercalation compounds. Upon intercalation, the

relative magnitudes of plasma edge shifts and absorption mechanisms change drastically as the number of free carriers within the material increases.[20]

Optical anisotropy is another significant characteristic of intercalation compounds. Since the contribution of free carriers to the dielectric constant is larger when the electric field is in-plane than when it is out-of-plane, intercalation compounds demonstrate substantial optical anisotropy in response to polarized light. The degree of anisotropy depends on the nature of the intercalant. In general, acceptor-type compounds electronically isolate individual host layers, making the bulk material behave like a collection of monolayers. Donors tend to couple adjacent layers because of greater hybridization. Thus, acceptors often exhibit greater optical anisotropy than donors.[20] The bulk and 2D materials highlighted in this review are highly anisotropic and therefore their corresponding intercalation compounds should demonstrate a considerable degree of optical anisotropy in the in-plane vs. out of plane axes. HOPG for example, is highly reflective when **E**||a but transmits strongly when **E**||c.[159] Based on this finding, the optical anisotropy in GICs synthesized from HOPG has been studied in order to elucidate distinctive features of the reflectance and transmission.[125]

In 1965, Hennig pioneered studies on the optical densities of donor- and acceptor-type GICs.[30] In the far-IR, the absorption coefficients of the intercalation compounds were higher than that of pristine graphite. This increase was ascribed to changes in the carrier concentration that induced shifts in the plasma frequency. In addition, at longer wavelengths, there was a transmission maximum in each of the spectra. Since the plasma frequency is known to occur when the electric field transfers a minimum amount of energy to the charge carriers, Hennig predicted that the enhanced transmission observed at lower energies was due to ω_p, and suggested optical reflectivity studies to confirm that the dielectric passes through zero at

this point.

These early observations initiated a cascade of investigations into the optical properties of intercalated layered materials, particularly graphite and TMDCs, described below. Studies in bulk, together with emerging investigations in 2D intercalation compounds provide a unique opportunity to compare optical properties as we approach atomically thin materials. In this section, we emphasize how shifts in the plasma edge, inter- and intra-band transitions, and optical anisotropy reveal interesting properties of bulk-intercalated materials, such as increased free carrier density or enhanced transparency, which are particularly relevant for optoelectronic applications. We also highlight several promising studies in 2D and few-layer materials and recommend future research directions in the optical properties of intercalated compounds, which remain largely unexplored.

The optical properties of GICs have been of particular interest, due to the high mobility of graphite and the useful frequency of its plasma resonance. In the near IR and visible regions of the electromagnetic spectrum, pristine graphite exhibits a continual decrease in reflectivity, as wavelength decreases. The vast majority of GICs demonstrate characteristic plasma edge shifts, with enhanced transmission near ω_p, which is expected for metallic free carrier absorption. Upon intercalation with donor or acceptor species in the low frequency regime, the free carrier contribution to the dielectric constant increases, while the interband component decreases due to the shift in E_F. In addition, the absolute reflectivity magnitude for the low-frequency region (when $\omega << \omega_p$), increases as the compound moves toward higher degrees of intercalation.[20] Similarly, there is a decrease in the minimum reflectivity value for a lower stage index. The plasma frequency also occurs at lower energies for acceptors compared to donors.[20] This reveals that the free carrier density for donors is higher than for

acceptors and indicates the fractional charge transfer that is characteristic of acceptor-type GICs.

In the late 1970s and 80s, many groups characterized acceptor-type compounds in terms of their optical reflectivity. **Figure 1-18**a-c shows the reflectance spectra of $SbCl_5$-, AsF_5-, and HNO_3-intercalated graphite. It is important to note that the position of the plasma edge strongly depends on the identity of the acceptor. For example, while stage 2 AsF_5-GIC demonstrates a plasma frequency of 1.43 eV, the ω_p of $SbCl_5$-GIC occurs near 1 eV. As a compound moves toward lower stages, ω_p shifts to shorter wavelengths. Another particularly important acceptor system that has been characterized through in-situ reflectance measurements is that of bisulfate-graphite.[30,55] Since the intercalation can be electrochemically controlled, this compound provides an interesting opportunity to study how the optical properties change as charge is transferred to the graphitic layers.

Zanini and Fischer were the first to characterize optical anisotropy in the alkali metal GICs. In their first study, they measured the reflectance spectra of MC_8 (stage 1) and MC_{24} (stage 2) when the light is incident on the c-face of the graphite sample and $\mathbf{E}||a$.[160] Reflectance spectra for stages 1-3 of Rb-GIC are depicted in **Figure 1-19**a. When $\omega<\omega_p$, the compound exhibits high reflectance, but as ω approaches ω_p, the reflectivity decreases to a minimum near $\omega= \omega_p$, provided that there are no interband effects. The minimum reflectance shifts to higher energies as the concentration of free carriers increases. In addition, the minimum reflectivity in stage 3 alkali metals occurs at a higher value than for either stage 1 or 2. Interband transitions near 1 eV interfere with the plasma frequency in stage 3, since the compound retains some of its graphitic character.[125]

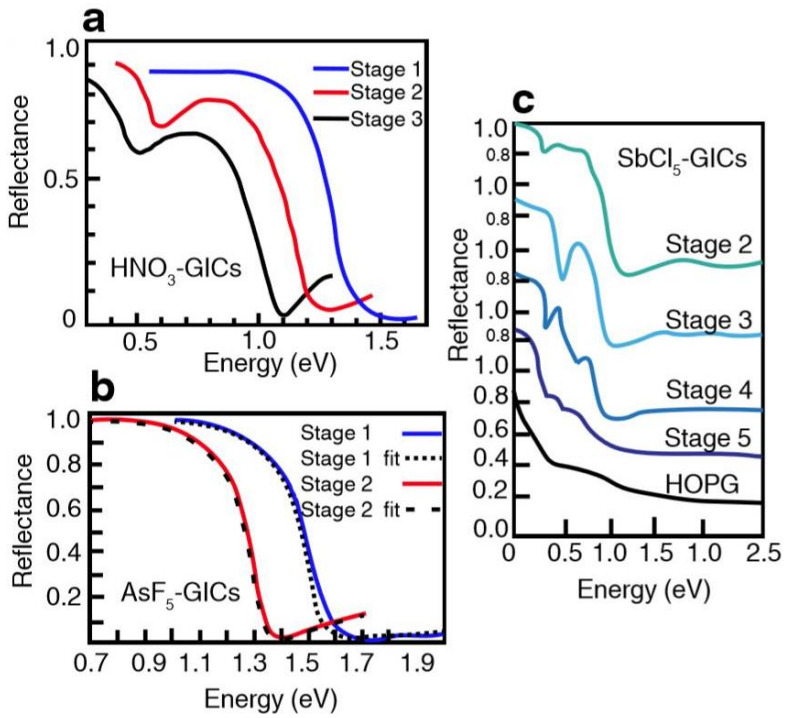


Figure 1-18. Plasma frequency shifts for acceptor GICs. a). Reflectivity measurements of Stages 1-3 HNO_3–GICs. The plasma frequency occurs at the reflectivity minimum between 1.0 and 1.5 eV for each compound and blue-shifts with higher degrees of staging. Adapted and reprinted figure[161] with permission from J. E. Fischer, T. E. Thompson, G. M. T. Foley, D. Guérard, Hoke, M, F. L. Lederman, *Phys. Rev. Lett.* **1976**, 37, 769. https://doi.org/10.1103/PhysRevLett.37.769. Copyright 1976, American Physical Society. b) Comparison of experimental reflectivity measurements (solid lines) with the calculated reflectance (dashed lines) for Stages 1 and 2 AsF_5–GICs. The plasma frequency shifts to higher energies from Stage 2 to Stage 1. Reproduced with permission.[162] Adapted from L. R. Hanlon, E. R. Falardeau, J. E. Fischer, *Solid State Commun.* **1977**, 17, 377 with permission from Elsevier. Copyright 1977, Elsevier. c) Reflectivity measurements of Stages 2-5 $SbCl_5$–GICs. As the material reaches higher degrees of staging, the plasma edge becomes sharper, but does not exhibit pronounced shifts in energy. Reproduced with permission.[163] Adapted from P. C. Eklund, D. S. Smith, V. R. K. Murthy, *Synth. Met.* **1981**, *3*, 111 with permission from Elsevier. Copyright 1981, Elsevier.

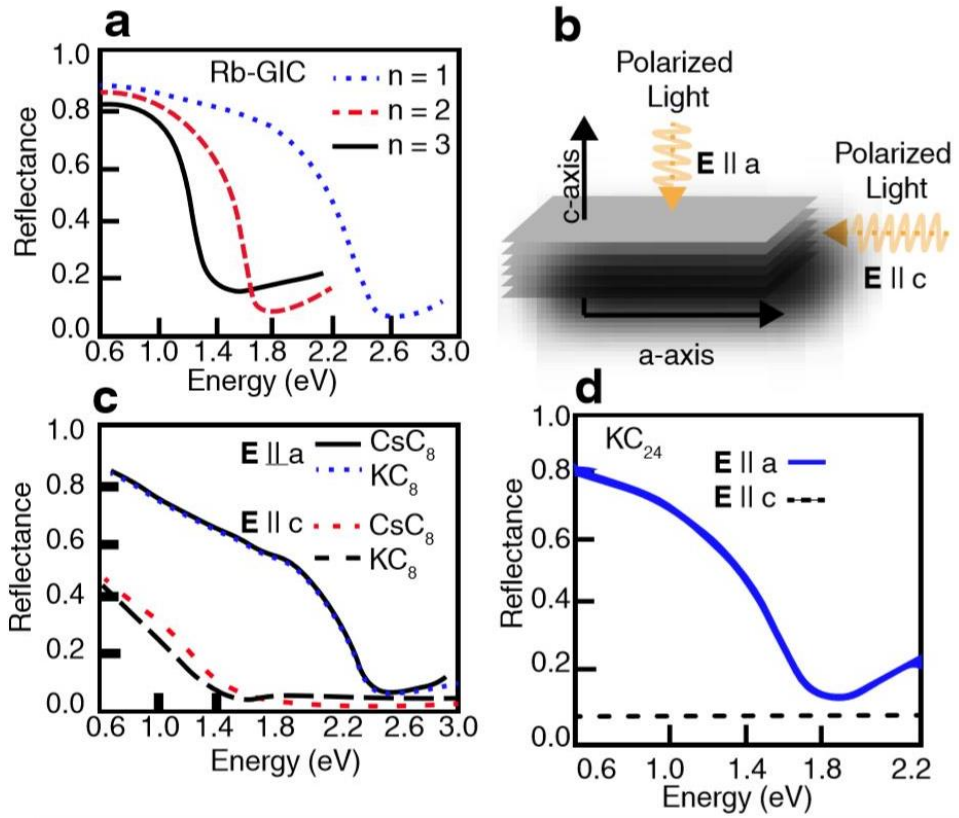


Figure 1-19. Plasma frequency shifts for donor GICs a) Reflectivity measurements for Stages 1-3 of Rb-GICs. The plasma frequency shifts from ~1.4 to 2.6 eV as the degree of staging increases from Stage 3 to Stage 1. Reproduced with permission.[160] Adapted and reprinted by permission from Springer: Il Nuovo Cimento B D. Guérard, G. M. T. Foley, M. Zanini, J. E. Fischer, *Nuovo Cim.* **1977**, 38, 410. Copyright 1977, Springer. b) Schematic illustrating light incident on a layered material in the **E**||a and **E**||c directions. c) Comparison of polarized reflectance spectra for KC_8 and CsC_8. When **E** is perpendicular to c, a larger blue-shift in the plasma frequency is observed for both compounds. When **E** is parallel to c, the plasma frequency occurs at lower energies. d) Polarized reflectance spectra for KC_{24}, showing plasma frequency near 1.8 eV for **E** perpendicular to c, but no observed reflectance when **E** is parallel to c. Reproduced with permission.[125] Reprinted from M. Zanini, J. E. Fischer, *Mater. Sci. Eng.* **1977**, 31, 169 with permission from Elsevier. Copyright 1977, Elsevier.

A critical finding of this study demonstrated that for these intercalation compounds, there is a distinct plasma frequency for different polarizations of light. Thus, each axis can be treated independently when considering plasma frequency effects. In order to compare the dielectric response of the material for **E**||a and **E**||c, the normalized reflectance spectra for both KC_8 and CsC_8 when **E**||**a** and **E**||**c** were measured. The **E**||a spectra remain unchanged from

those collected at the c-face. Interestingly, however, a metallic edge emerges when **E**||c. The reflectance minimum for **E**||c also shifts to lower energies, from 2.7 eV to 1.8 eV. The shift that occurs upon polarization demonstrates that the dielectric response of the material is highly anisotropic. To study the anisotropy in higher stages, they measured the reflectance of KC_{24} cleaved on the a-face (Figure 1-20b). As expected, **E**||a is almost identical to the response of KC_{24} at the c-face. When the electric field was parallel to the c-face, the stage 2 compound exhibited non-metallic characteristics over the range of energies and possessed a spectrum similar to that of pristine graphite for **E**||c. The authors noted that this absence of metallic reflectance above 0.5 eV in KC_{24} with **E**||c indicated that the carriers are more anisotropic in MC_{24} than in MC_8 compounds. In particular, they modeled the 2D and 3D carriers within the GICs, and found that the 2D carriers do not contribute to the reflectance or c-axis conductivity when ||c. An analysis of the band structure of MC_8 was useful for explaining these results. As the compound transitions from stage 1 to stage 2, the density of metal atoms decreased, which lowered E_F. Thus, E_F only intersected with the π bands that are 2D in character. Since there are two adjacent graphite layers between each layer of metal atoms, however, there may also be c-axis dispersion in the π bands. This distribution would induce partial 3D character into MC_{24}. Only a fraction of the carriers contributes to the c-axis conductivity. Thus, there are most likely mixed 2D and 3D electronic states in the material. In addition, 2D carriers were more efficient for conduction along the a-axis compared to 3D carriers. This observation could explain the higher conductivity values in acceptor GICs, which are known to be more electronically isolated than donor GICs.

In 2D, unusual optical properties emerge. Few-layer GICs are of particular interest due to the possibility of simultaneously inducing high conductivity and greater transparency. This

trend results from a high degree of charge transfer to the graphite layer, which upshifts E_F and effectively suppresses interband optical transitions. As the optical transmission increases, there should be a concurrent enhancement in conductivity from the increased carrier concentration.

However, there is a limit to the increase in transparency. At sufficiently high doping levels, coupling between the electrons and longitudinal optical phonons becomes significant and intraband transitions begin to inhibit transmission. Recently, several groups have demonstrated the effect of intercalation on the transparency of FLG.[6,7] In the first investigation of transmission in lithium-doped ultrathin graphite, in-situ Raman and transmission measurements indicated that the transparency of the flakes depends strongly on the degree of staging, wavelength of light, and sample thickness.[6] **Figure 1-20**a-c show the percent transmission of the flakes with thicknesses ranging from 8 to 83 layers at wavelengths spanning 400 to 800 nm. As expected, transmission is higher for thinner flakes. Since the interband optical transitions are suppressed in highly doped FLG (Figure 1-20f), higher stages should also correspond to greater transmittance values. Indeed, for stage 2 Li FL-GIC, the transmittance increased over all wavelengths. Although 8 L LiC_6 achieved 91.7 % transmittance, the thicker flakes did not follow the same trend. For 18 L to 83 L stage 1 Li FL-GIC, transmission increased from 400 to 500 nm and decreased from 600 to 800 nm (Figure 1-20c). To account for this behavior, the authors modeled the transmission of lithiated graphite (Figure 1-20d,e) and proposed that the transmission will increase only when the photon energies are within the following range: $\hbar/\tau < \hbar\omega_f < 2\ E_F$, where τ is the carrier relaxation time and ω_f is the photonic frequency. When $\omega < \tau^{-1}$, intraband transitions occur and transmission is reduced. This model allows the limits of transparency to be predicted for other highly doped FLG systems.

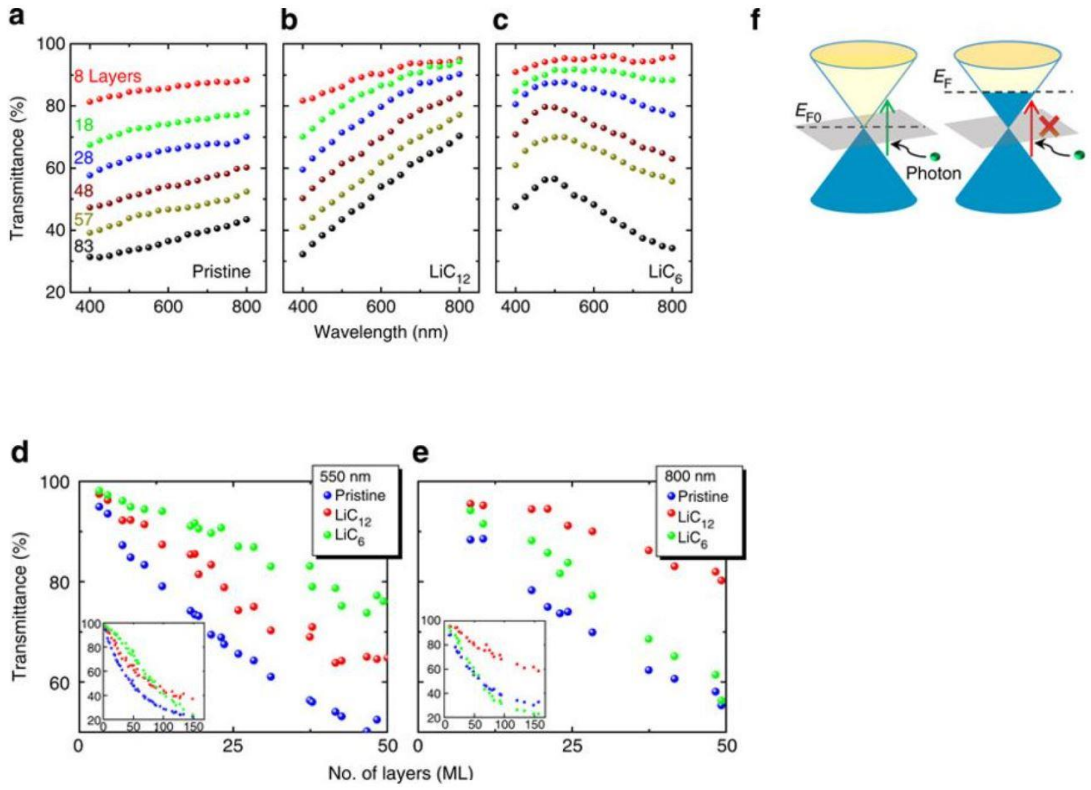


Figure 1-20. Transmittance as a function of wavelength for LiC_6 a) pristine graphite, b) LiC_{12}, and c) LiC_6. The thicknesses of the graphite samples range from 8L-83L. Thinner samples are more transparent, while thicker flakes have lower transmittance values. The transmittance increases linearly with increasing wavelength in a) and b) across all thicknesses. In c) transmission increases at shorter wavelengths and decreases at longer wavelengths for 18L-83L. The transmission of 8L generally increases over the range of wavelengths. Transmittance as a function of thickness for pristine (blue circles), LiC_{12} (red circles), and LiC_6 (green circles) at d) 550 nm and e) 800 nm. Stage 1 LiC_6 exhibits the highest transmittance across all thicknesses at 550 nm. Stage 2 LiC_{12} compounds have greatest transmittance across all thicknesses at 800 nm. f) Illustration of the band structure of graphene showing that optical transitions are suppressed when E_F is raised due to n-type doping. Reproduced with permission.[6] Reprinted by permission from Springer Nature. W. Bao, J. Wan, X. Han, X. Cai, H. Zhu, D. Kim, D. Ma, Y. Xu, J. N. Munday, H. D. Drew, M. S. Fuhrer, L. Hu, *Nat. Commun.* **2014**, 5, 4224. Copyright 2014, Springer Nature.

Extrinsic optical switching highlights the useful properties of 2D intercalation compounds. In particular, the capability of a material to transition from reflective and

absorbing to highly transparent opens up exciting avenues to develop a variety of optoelectronics applications, such as conductive and transparent electrodes and tunable thin-film displays.

1.6 Conclusions and Outlook

This review aims to provide a historical perspective of intercalation in bulk layered materials in order to interpret recent advances in few-layer intercalation compounds. To this end, we have highlighted scaling relationships that describe the current state of knowledge in understanding how intercalation kinetics, structure, and electronic and optical properties depend on material thickness and lateral dimension, with a particular emphasis on few-layer and monolayer materials. In this final section, we will discuss several key challenges in developing few-layer intercalated materials for energy storage devices, promote strategies for designing functional hybrid materials, and propose research directions for emerging optoelectronic applications.

Currently, one of the key energy storage challenges for few-layer materials is to access capacities and cycling performances comparable to or surpassing state-of-the-art bulk electrodes. Recent work suggests that capacities surpassing bulk electrodes may be attainable[164], but it will be important to ascertain whether these findings are generalizable. The scaling relationships indicate that 2D materials tend to suffer from lower capacities and cyclability compared to bulk electrodes. Although these drawbacks could severely limit the role of 2D materials in energy storage devices, they also pose an interesting design challenge for researchers: to develop innovative strategies that enable the fundamental scaling limits to be circumvented. Since 2D materials or 2D heterostructures present exciting opportunities to

create electrodes with rapid diffusion, this problem merits consideration. For example, engineering 2D materials with ultrafast diffusion could dramatically extend the size scale at which pseudocapacitance occurs. Few-layer materials could also enable electrodes with shorter timescales for in-plane diffusion than grain boundary transport, since the length-scale for in-plane transport can be three to five orders of magnitude greater than the length-scale of the grain boundary.[165]

Heterostructures also present an attractive pathway to capture or engineer favorable properties in a restacked hybrid material. With the emergence of vdW heterostructures, there are substantial opportunities to expand the class of few-layer and bulk layered materials beyond the traditional graphene/TMDCs, through creative synthetic approaches. For example, in 2015, Cui *et al.* synthesized a graphene/BP hybrid conversion material for sodium ion batteries through liquid exfoliation.[166] The resulting material demonstrated a high specific capacity, minimized volume expansion, and good cyclability.[166] If this method were generalizable to other layered materials, it could allow for the rapid synthesis of functional hybrid materials for a variety of applications beyond energy storage. Ion-bombardment, ion-exchange, and numerous other techniques also open the exciting possibility of synthesizing heterostructures from substitutionally doped 2D materials or surfaces. While incorporating doped materials into a heterostructure may modify the optoelectronic properties, subsequent intercalation of these doped heterostructures could further enable distinct carrier concentrations and transport properties, expanding the possibilities of these structures. Another interesting approach to synthesize unique heterostructures is through intercalation. Intercalating ions or molecules into a host material generates a secondary layer in the interlayer space, resulting in the formation of a heterostructure. For example, Koski *et al.*[167,168] created layered heterostructures by

intercalating an anion followed by a cation into the interlayer space of various TMDCs. These methods could be relevant for expanding the class of vdW heterostructures. It would also be of interest to synthesize heterostructures for Si electrode materials. Although Si electrodes demonstrate high capacities[169], silicene is unstable and difficult to synthesize.[170] Thus, alternative synthetic methods are necessary to create a Si-based heterostructure. Another possible route is to identify a Si-rich layered material, etch away the other elements, and restack the layers to form a hybrid material. To assess the performance of these new heterostructures in functional devices, it will be important to isolate the mechanism of intercalation and engineer the formation of the solid-electrolyte interphase. Thus, further developing *in-situ* characterization techniques, such as STEM[171], cryo-TEM[99], and X-ray reflectivity[172] will offer valuable insight into intercalation in few-layer heterostructures. Although we have presented several methods for synthesizing and characterizing vdW heterostructures for electrode materials, this discussion is far from comprehensive. To inform experimental work in this area, it will be particularly critical to further explore computational methods that predict interlayer interactions, intercalation voltages, and charge transfer in vdW heterostructures.

For optoelectronic applications, few-layer intercalation compounds are promising optical switches, color filters, and tunable displays. Here we describe several promising research directions for exploring the optical properties of these materials. First, with the emerging class of intercalated vdW heterostructures, it will be important to characterize their optical properties through *in-situ* techniques. As we discuss in this review, planar devices enable a variety of *in-situ* optical measurements, such as UV-vis reflectance, transmittance, Raman and FT-IR spectroscopies for visualizing intercalation. These techniques will offer valuable insight into how the optical properties change during intercalation in vdW

heterostructures, as well as other systems such as twisted bilayer graphene. Another interesting direction is to utilize intercalation to simulate 2D properties in bulk compound. Recently, Wang *et al.* electrochemically intercalated a quaternary ammonium compound into bulk layered crystals.[173] Surprisingly, the fully-intercalated materials behaved as a collection of monolayers, since the large size of the intercalant electronically isolated the layers. This work provides a unique platform to study how the optical properties change from bulk to 2D *in-situ*. For example, identifying a material that is non-fluorescent in bulk, but fluoresces as a monolayer could lead to interesting studies that probe fluorescence *in-situ* as the monolayers are isolated through electrochemical intercalation. In addition, it may also be possible to expand many of the exciting properties of ionic liquid-gated 2D materials[174–176] to few- or multi-layered materials by using intercalation, since ionic-liquid gating is largely limited to 2D monolayers because of electrostatic screening. It should be possible to achieve similar carrier concentrations in few- or multi-layer materials through electrochemical intercalation for applications that require stronger absorption, higher current densities, and tunable properties.

As we have highlighted, 2D intercalation is a rapidly developing area and has realized a series of rapid breakthroughs in recent years. These breakthroughs are offering insight into both the essential scaling relationships that govern structure-property relationships, but also highlighting exciting examples of how scaling relationships can be circumvented to achieve higher performance in energy storage, optics, and electronics. And yet, despite this recent progress, we believe that many fundamental advances and promising applications will yet emerge.

REFERENCES

[1] M. S. Stark, K. L. Kuntz, S. J. Martens, S. C. Warren, *Adv. Mater.* **2019**, *31*, 1.

[2] L. Oakes, R. Carter, T. Hanken, A. P. Cohn, K. Share, B. Schmidt, C. L. Pint, *Nat. Commun.* **2016**, *7*, 11796.

[3] D. K. Bediako, M. Rezaee, H. Yoo, D. T. Larson, S. Y. F. Zhao, T. Taniguchi, K. Watanabe, T. L. Brower-Thomas, E. Kaxiras, P. Kim, *Nature* **2018**, *558*, 425.

[4] Z. Dai, X. Xiao, W. Wu, Y. Zhang, L. Liao, S. Guo, J. Ying, C. Shan, M. Sun, C. Jiang, *Light Sci. Appl.* **2015**, *4*, e342.

[5] N. Jung, B. Kim, A. C. Crowther, N. Kim, C. Nuckolls, L. E. Brus, *ACS Nano* **2011**, *5*, 5708.

[6] W. Bao, J. Wan, X. Han, X. Cai, H. Zhu, D. Kim, D. Ma, Y. Xu, J. N. Munday, H. D. Drew, M. S. Fuhrer, L. Hu, *Nat. Commun.* **2014**, *5*, 4224.

[7] I. Khrapach, F. Withers, T. H. Bointon, D. K. Polyushkin, W. L. Barnes, S. Russo, M. F. Craciun, *Adv. Mater.* **2012**, *24*, 2844.

[8] F. Xiong, H. Wang, X. Liu, J. Sun, M. Brongersma, E. Pop, Y. Cui, *Nano Lett.* **2015**, *15*, 6777.

[9] V. K. Sangwan, D. Jariwala, I. S. Kim, K. S. Chen, T. J. Marks, L. J. Lauhon, M. C. Hersam, *Nat. Nanotechnol.* **2015**, *10*, 403.

[10] R. Zhang, J. Waters, A. K. Geim, I. V Grigorieva, *Nat. Commun.* **2017**, *8*, 1.

[11] A. Koh, D. Kang, Y. Xue, S. Lee, R. M. Pielak, J. Kim, T. Hwang, S. Min, A. Banks, P. Bastien, M. C. Manco, L. Wang, K. R. Ammann, K.-I. Jang, P. Won, S. Han, R. Ghaffari, U. Paik, M. J. Slepian, G. Balooch, Y. Huang, J. A. Rogers, *Sci. Transl. Med.* **2016**, *8*, 366ra165.

[12] X. Huang, T. Leng, M. Zhu, X. Zhang, J. Chen, K. Chang, M. Aqeeli, A. K. Geim, K. S. Novoselov, Z. Hu, *Sci. Rep.* **2015**, *5*, 18298.

[13] G. S. Kulkarni, K. Reddy, Z. Zhong, X. Fan, *Nat. Commun.* **2014**, *5*, 4376.

[14] S. K. Ameri, R. Ho, H. Jang, Y. Wang, L. Wang, D. M. Schnyer, D. Akinwande, N. Lu, *ACS Nano* **2017**, *11*, 7634.

[15] N. Youngblood, M. Li, *Nanophotonics* **2017**, *6*, 1205.

[16] J. Wan, S. D. Lacey, J. Dai, W. Bao, M. S. Fuhrer, L. Hu, *Chem. Soc. Rev.* **2016**, *45*, 6742.

[17] Y. Jung, Y. Zhou, J. J. Cha, *Inorg. Chem. Front.* **2016**, *3*, 452.

[18] N. Jung, N. Kim, S. Jockusch, N. J. Turro, P. Kim, L. Brus, *Nano Lett.* **2009**, *9*, 4133.

[19] L. B. Ebert, *Annu. Rev. Mater. Sci.* **1976**, *6*, 181.

[20] M. S. Dresselhaus, G. Dresselhaus, *Adv. Phys.* **1981**, *51*, 1.

[21] A. R. Beal, W. Y. Liang, *Philos. Mag.* **1973**, *27*, 1397.

[22] P. Schaufhäutl, *J. für Prakt. Chemie* **1841**, *21*, 155.

[23] M. S. Whittingham, A. J. Jacobson, Eds. , *Intercalation Chemistry*, Academic Press, New York City, USA, **1982**.

[24] M. Noel, R. Santhanam, *J. Power Sources* **1998**, *72*, 53.

[25] U. Hoffmann, A. Frenzel, *Z. Elektrochem.* **1931**, *37*.

[26] A. Schleede, M. Wellmann, *Zeits. Phys. Chem.* **1932**, *1*, 1.

[27] F. L. Vogel, *Bull. Am. Phys. Soc.* **1976**, *21*.

[28] F. L. Vogel, *J. Mater. Sci.* **1977**, *12*, 982.

[29] A. R. Ubbelohde, *Proc. R. Soc. A* **1972**, *327*, 289.

[30] G. R. Hennig, *J. Chem. Phys.* **1965**, *43*, 1201.

[31] W. Luo, J. Wan, B. Ozdemir, W. Bao, Y. Chen, J. Dai, H. Lin, Y. Xu, F. Gu, V. Barone, L. Hu, *Nano Lett.* **2015**, *15*, 7671.

[32] N. Daumas, A. Hérold, *C.R. Hebd. Seances Acad. Sci., Ser. C* **1969**, *268*, 373.

[33] M. Inagaki, *J. Mater. Res.* **1989**, *4*, 1560.

[34] N. Watanabe, M. Fukuda, *Primary Cell for Electric Batteries*, **1968**, 3536532.

[35] S. Flandrois, J. M. Masson, J. C. Rouillon, *Synth. Met.* **1981**, *3*, 195.

[36] M. Winter, J. O. Besenhard, M. E. Spahr, P. Novák, *Adv. Mater.* **1998**, *10*, 725.

[37] K. S. Novoselov, A. K. Geim, S. V. Morozov, D. Jiang, Y. Zhang, S. V. Dubonos, I. V. Grigorieva, A. A. Firsov, *Science (80-.).* **2004**, *306*, 666.

[38] K. F. Mak, C. Lee, J. Hone, J. Shan, T. F. Heinz, *Phys. Rev. Lett.* **2010**, *105*, 2.

[39] B. Radisavljevic, A. Radenovic, J. Brivio, V. Giacometti, A. Kis, *Nat. Nanotechnol.* **2011**, *6*, 147.

[40] A. Splendiani, L. Sun, Y. Zhang, T. Li, J. Kim, C. Y. Chim, G. Galli, F. Wang, *Nano Lett.* **2010**, *10*, 1271.

[41] A. H. Woomer, T. W. Farnsworth, J. Hu, R. A. Wells, C. L. Donley, S. C. Warren, *ACS Nano* **2015**, *9*, 8869.

[42] S. Zhang, J. Yang, R. Xu, F. Wang, W. Li, M. Ghufran, Y.-W. Zhang, Z. Yu, G. Zhang, Q. Qin, Y. Lu, *ACS Nano* **2014**, *8*, 9590.

[43] L. Liang, J. Wang, W. Lin, B. G. Sumpter, V. Meunier, M. Pan, *Nano Lett.* **2014**, *14*, 6400.

[44] Y. Takao, H. Asahina, A. Morita, *J. Phys. Soc. Jpn.* **1981**, *50*, 3362.

[45] V. Tran, R. Soklaski, Y. Liang, L. Yang, *Phys. Rev. B* **2014**, *89*, 235319.

[46] Y. Akahama, S. Endo, S. Narita, *J. Phys. Soc. Jpn.* **1983**, *52*, 2148.

[47] K. Kanetani, K. Sugawara, T. Sato, R. Shimizu, K. Iwaya, T. Hitosugi, T. Takahashi, *Proc. Natl. Acad. Sci. U. S. A.* **2012**, *109*, 19610.

[48] J. Wan, W. Bao, Y. Liu, J. Dai, F. Shen, L. Zhou, X. Cai, D. Urban, Y. Li, K. Jungjohann, M. S. Fuhrer, L. Hu, *Adv. Energy Mater.* **2015**, *5*, 1401742.

[49] N. Kim, K. S. Kim, N. Jung, L. Brus, P. Kim, *Nano Lett.* **2011**, *11*, 860.

[50] T. H. Bointon, I. Khrapach, R. Yakimova, A. V Shytov, M. F. Craciun, S. Russo, *Nano Lett.* **2014**, *14*, 1751.

[51] J. Hui, M. Burgess, J. Zhang, J. Rodríguez-López, *ACS Nano* **2016**, *10*, 4248.

[52] J. G. Hooley, W. P. Garby, J. Valentin, *Carbon N. Y.* **1965**, *3*, 7.

[53] W. Zhao, P. H. Tan, J. Liu, A. C. Ferrari, *J. Am. Chem. Soc.* **2011**, *133*, 5941.

[54] J. G. Hooley, *Mater. Sci. Eng.* **1977**, *31*, 17.

[55] A. Metrot, J. E. Fischer, *Synth. Met.* **1981**, *3*, 201.

[56] K. Fredenhagen, G. Cadenbach, *Z. Anorg. Allg. Chem.* **1926**, *158*.

[57] H. Thiele, *Z. Anorg. Allg. Chem.* **1932**, *207*, 340.

[58] M. S. Dresselhaus, *Intercalation in Layered Materials*, **1986**.

[59] M. Naguib, V. N. Mochalin, M. W. Barsoum, Y. Gogotsi, *Adv. Mater.* **2014**, *26*, 992.

[60] T. Enoki, M. Suzuki, M. Endo, *Graphite Intercalation Compounds and Applications*, Oxford University Press, **2003**.

[61] D. E. Nixon, G. S. Parry, *J. Phys. C Solid State Phys.* **1969**, *2*, 1732.

[62] S. K. Khanna, E. R. Falardeau, A. J. Heeger, J. E. Fischer, *Solid State Commun.* **1978**, *25*, 1059.

[63] W. Müller-Warmuth, R. Schöllhorn, *Progress in Intercalation Research*, Springer Science & Business Media, **1994**.

[64] W. Rüdorff, W.-F. Siecke, *Chem. Ber.* **1958**, *91*, 1348.

[65] M. J. Bottomley, G. S. Parry, A. R. Ubbelohde, D. A. Young, *J. Chem. Soc.* **1963**, 5674.

[66] D. Horn, H. P. Boehm, *Mater. Sci. Eng.* **1977**, *31*, 87.

[67] W. Rüdorff, U. Hofmann, *Z. Anorg. Allg. Chem.* **1938**, *238*, 1.

[68] E. R. White, J. J. Lodico, B. C. Regan, *Nat. Commun.* **2017**, *8*, 1969.

[69] M. Yoo, C. W. Frank, S. Mori, S. Yamaguchi, *Polymer (Guildf).* **2003**, *44*, 4197.

[70] J. Zhao, X. Zou, Y. Zhu, Y. Xu, C. Wang, *Adv. Funct. Mater.* **2016**, *26*, 8103.

[71] R. Carter, B. Huhman, C. T. Love, I. V Zenyuk, *J. Power Sources* **2018**, *381*, 46.

[72] J. Zou, C. Sole, N. E. Drewett, M. Velicky, L. J. Hardwick, *J. Phys. Chem. Lett.* **2016**, *7*, 4291.

[73] H. Sun, A. Varzi, V. Pellegrini, D. A. Dinh, R. Raccichini, A. E. Del Rio-Castillo, M. Prato, M. Colombo, R. Cingolani, B. Scrosati, S. Passerini, F. Bonaccorso, *Solid State Commun.* **2017**, *251*, 88.

[74] M. D. Levi, D. Aurbach, *J. Phys. Chem. B* **1997**, *101*, 4630.

[75] D. Aurbach, B. Markovsky, I. Weissman, E. Levi, Y. Ein-Eli, *Electrochim. Acta* **1999**, *45*, 67.

[76] M. Winter, J. O. Besenhard, M. E. Spahr, P. Novák, *Adv. Mater.* **1998**, 725.

[77] T. Placke, G. Schmuelling, R. Kloepsch, P. Meister, O. Fromm, P. Hilbig, H.-W. Meyer, M. Winter, *Z. Anorg. Allg. Chem.* **2014**, *640*, 1996.

[78] X. Y. Song, K. Kinoshita, T. D. Tran, *J. Electrochem. Soc.* **1996**, *143*, L120.

[79] M. S. Whittingham, A. H. Thompson, *J. Chem. Phys.* **1975**, *62*, 1588.

[80] A. R. Kamali, D. J. Fray, *Nanoscale* **2015**, *7*, 11310.

[81] G. Yoon, D.-H. Seo, K. Ku, J. Kim, S. Jeon, K. Kang, *Chem. Mater.* **2015**, *27*, 2067.

[82] H. Wang, Z. Lu, S. Xu, D. Kong, J. J. Cha, G. Zheng, P.-C. Hsu, K. Yan, D. Bradshaw, F. B. Prinz, Y. Cui, *Proc. Natl. Acad. Sci.* **2013**, *110*, 19701.

[83] C. Liu, Z. G. Neale, G. Cao, *Mater. Today* **2016**, *19*, 109.

[84] M. Okubo, E. Hosono, J. Kim, M. Enomoto, N. Kojima, T. Kudo, H. Zhou, I. Honma, *J. Am. Chem. Soc.* **2007**, *129*, 7444.

[85] G. A. Muller, J. B. Cook, H. S. Kim, S. H. Tolbert, B. Dunn, *Nano Lett.* **2015**, *15*, 1911.

[86] E. Peled, *J. Electrochem. Soc.* **1979**, *126*, 2047.

[87] M. Gauthier, T. J. Carney, A. Grimaud, L. Giordano, N. Pour, H.-H. Chang, D. P. Fenning, S. F. Lux, O. Paschos, C. Bauer, F. Maglia, S. Lupart, P. Lamp, Y. Shao-Horn, *J. Phys. Chem. Lett.* **2015**, *6*, 4653.

[88] Y.-M. Liu, B. G. Nicolau, J. L. Esbenshade, A. A. Gewirth, *Anal. Chem.* **2016**, *88*, 7171.

[89] Y. Park, S. H. Shin, H. Hwang, S. M. Lee, S. P. Kim, H. C. Choi, *J. Mol. Struct.* **2014**, *1069*, 157.

[90] M. G. S. R. Thomas, P. G. Bruce, J. B. Goodenough, *J. Electrochem. Soc.* **1985**, *132*, 1521.

[91] C.-M. Park, H.-J. Sohn, *Adv. Mater.* **2007**, *19*, 2465.

[92] D. Guyomard, J. M. Tarascon, *J. Electrochem. Soc.* **1993**, *140*, 3071.

[93] N. Yabuuchi, K. Yoshii, S.-T. Myung, I. Nakai, S. Komaba, *J. Am. Chem. Soc.* **2011**, *133*, 4404.

[94] K. Edström, T. Gustafsson, J. O. Thomas, *Electrochim. Acta* **2004**, *50*, 397.

[95] K. Xu, *Chem. Rev.* **2014**, *114*, 11503.

[96] E. Peled, S. Menkin, *J. Electrochem. Soc.* **2017**, *164*, A1703.

[97] K. Leung, J. Budzien, *Phys. Chem. Chem. Phys.* **2010**, *12*, 6583.

[98] C.-F. Chen, P. P. Mukherjee, *Phys. Chem. Chem. Phys.* **2015**, *17*, 9812.

[99] Y. Li, Y. Li, A. Pei, K. Yan, Y. Sun, C.-L. Wu, L.-M. Joubert, R. Chin, A. L. Koh, Y. Yu, J. Perrino, B. Butz, S. Chu, Y. Cui, *Science (80-.).* **2017**, *358*, 506.

[100] R. Deshpande, M. Verbrugge, Y.-T. Cheng, J. Wang, P. Liu, *J. Electrochem. Soc.* **2012**, *159*, A1730.

[101] S. Shi, P. Lu, Z. Liu, Y. Qi, L. G. Hector, H. Li, S. J. Harris, *J. Am. Chem. Soc.* **2012**, *134*, 15476.

[102] H. L. Zhang, F. Li, C. Liu, J. Tan, H. M. Cheng, *J. Phys. Chem. B* **2005**, *109*, 22205.

[103] A. J. Smith, J. C. Burns, X. Zhao, D. Xiong, J. R. Dahn, *J. Electrochem. Soc.* **2011**, *158*, A447.

[104] J. Christensen, J. Newman, *J. Electrochem. Soc.* **2004**, *151*, A1977.

[105] S. J. Harris, P. Lu, *J. Phys. Chem. C* **2013**, *117*, 6481.

[106] E. Peled, D. Golodnitsky, G. Ardel, *J. Electrochem. Soc.* **1997**, *144*, L208.

[107] P. B. Balbuena, Y. Wang, Eds. , *Lithium-Ion Batteries - Solid-Electrolyte Interphase*, Imperial College Press, London, **2004**.

[108] D. Pan, S. Wang, B. Zhao, M. Wu, H. Zhang, Y. Wang, Z. Jiao, *Chem. Mater.* **2009**, *21*, 3136.

[109] J. B. Goodenough, Y. Kim, *Chem. Mater.* **2010**, *22*, 587.

[110] J. E. Fischer, in *Intercalated Layer. Mater.* (Ed.: F.A. Levy), D. Reidel, Boston, U.S.A., **1979**, pp. 481–530.

[111] A. W. Moore, A. R. Ubbelohde, D. A. Young, *Proc. R. Soc. A* **1964**, *280*, 153.

[112] L. C. F. Blackman, J. F. Mathews, A. R. Ubbelohde, *Proc. R. Soc. A* **1960**, *A258*, 339.

[113] W. A. Kamitakahara, J. L. Zarestky, P. C. Eklund, *Synth. Met.* **1985**, *12*, 301.

[114] P. C. Eklund, E. T. Arakawa, J. L. Zaretsky, W. A. Kamitakahara, G. D. Mahan, *Synth. Met.* **1985**, *12*, 97.

[115] S. Y. Leung, G. Dresselhaus, M. S. Dresselhaus, *Phys. Rev. B* **1981**, *24*, 6083.

[116] P. C. Eklund, in *Intercalation Layer. Mater.* (Ed.: M.S. Dresselhaus), Springer, New York City, USA, **1986**, pp. 337–344.

[117] L. Pietronero, S. Strässler, *Phys. Rev. Lett.* **1981**, *47*, 593.

[118] C. T. Chan, W. A. Kamitakahara, K. M. Ho, *Phys. Rev. Lett.* **1987**, *58*, 1528.

[119] S. Flandrois, C. Hauw, R. B. Mathur, *Synth. Met.* **1989**, *34*, 399.

[120] R. H. Friend, A. D. Yoffe, *Adv. Phys.* **1987**, *36*, 1.

[121] N. A. W. Holzwarth, S. Rabii, L. A. Girifalco, *Phys. Rev. B* **1978**, *18*, 5190.

[122] N. A. W. Holzwarth, L. A. Girifalco, S. Rabii, *Phys. Rev. B* **1978**, *18*, 5206.

[123] N. A. W. Holzwarth, S. G. Louie, S. Rabii, *Phys. Rev. B* **1984**, *30*, 2219.

[124] W. Eberhardt, I. T. McGovern, E. W. Plummer, J. E. Fischer, *Phys. Rev. Lett.* **1980**, *44*, 200.

[125] M. Zanini, J. E. Fischer, *Mater. Sci. Eng.* **1977**, *31*, 169.

[126] P. Oelhafen, P. Pfluger, E. Hauser, H. J. Guntherodt, *Phys. Rev. Lett.* **1980**, *44*, 197.

[127] D. P. DiVincenzo, S. Rabii, *Phys. Rev. B* **1982**, *25*, 4110.

[128] T. Inoshita, K. Nakao, H. Kammura, *J. Phys. Soc. Japan* **1977**, *43*, 1237.

[129] M. S. Dresselhaus, G. Dresselhaus, *Synth. Met.* **1985**, *12*, 79.

[130] R. A. Nistor, D. M. Newns, G. J. Martyna, *ACS Nano* **2011**, *5*, 3096.

[131] S. Flandrois, J.-M. Masson, J.-C. Rouillon, J. Gaultier, C. Hauw, *Synth. Met.* **1981**, *3*, 1.

[132] A. Das, S. Pisana, S. Piscanec, B. Chakraborty, S. K. Saha, U. V. Waghmare, R. Yiang, H. R. Krishnamurhthy, A. K. Geim, A. C. Ferrari, A. K. Sood, *Nat. Nanotechnol.* **2008**, *3*, 210.

[133] S. Pisana, M. Lazzeri, C. Casiraghi, K. S. Novoselov, A. K. Geim, A. C. Ferrari, F. Mauri, *Nat. Mater.* **2007**, *6*, 198.

[134] M. Lazzeri, F. Mauri, *Phys. Rev. Lett.* **2006**, *97*, 266407.

[135] A. C. Ferrari, *Solid State Commun.* **2007**, *143*, 47.

[136] D. Zhan, L. Sun, Z. H. Ni, L. Liu, X. F. Fan, Y. Wang, T. Yu, Y. M. Lam, W. Huang, Z. X. Shen, *Adv. Funct. Mater.* **2010**, *20*, 3504.

[137] U. Gubler, J. Krieg, P. Oelhafen, P. Pfluger, H.-J. Guntherodt, E. Cartier, F. Heinrich, in *Phys. Intercalation Compd.* (Eds.: L. Pietronero, E. Tosatti), Springer, Berlin, Germany, **1981**, pp. 69–79.

[138] B. J. Schultz, R. V. Dennis, V. Lee, S. Banerjee, *Nanoscale* **2014**, *6*, 3444.

[139] R. Schlögl, in *Graph. Intercalation Compd. II* (Eds.: H. Zabel, S.A. Solin), Springer-Verlag, Berlin, Germany, **1992**, pp. 53–102.

[140] F. L. Vogel, G. M. T. Foley, C. Zeller, E. R. Falardeau, J. Gan, *Mater. Sci. Eng.* **1977**, *31*, 261.

[141] E. McRae, J. F. Marêché, *J. Mater. Res.* **1988**, *3*, 75.

[142] R. S. Markiewicz, *Solid State Commun.* **1986**, *57*, 237.

[143] L. Piraux, J.-P. Issi, J. F. Marêché, E. McRae, *Synth. Met.* **1989**, *30*, 245.

[144] A. M. Hermann, R. Somoano, V. Hadek, A. Rembaum, *Solid State Commun.* **1973**, *13*, 1065.

[145] M. Sarma, A. R. Beal, S. Nulsen, R. H. Friend, *J. Phys. C Solid State Phys.* **1981**, *15*, 4367.

[146] Y. Ōnuki, R. Inada, S. Tanuma, S. Yamanaka, H. Kamimura, *J. Phys. Soc. Japan* **1982**, *51*, 880.

[147] Y. Maruyama, S. Suzuki, K. Kobayashi, S. Tanuma, *Phys. B* **1981**, *105*, 99.

[148] T. Nishii, Y. Maruyama, T. Inabe, I. Shirotani, *Synth. Met.* **1987**, *18*, 559.

[149] I. L. Spain, in *Chem. Phys. Carbon* (Eds.: P.L. Walker, P.A. Thrower), Marcel Dekker, New York City, USA, **1973**, pp. 105, 110.

[150] L. Pietronero, S. Strässler, H. R. Zeller, *Solid State Commun.* **1979**, *30*, 399.

[151] L. Pietronero, S. Strässler, H. R. Zeller, M. J. Rice, *Phys. Rev. Lett.* **1978**, *41*, 763.

[152] E. McRae, D. Billaud, J. F. Marêché, A. Hérold, *Phys. B* **1980**, *99*, 489.

[153] S. Bae, H. Kim, Y. Lee, X. Xu, J.-S. Park, Y. Zheng, J. Balakrishnan, T. Lei, H. R. Kim, Y. Il Song, Y. Kim, K. S. Kim, B. Özyilmaz, J.-H. Ahn, B. H. Hong, S. Iijima, *Nat. Nanotechnol.* **2010**, *5*, 574.

[154] Y. Wang, S. W. Tong, X. F. Xu, B. Özyilmaz, K. P. Loh, *Adv. Mater.* **2011**, *23*, 1514.

[155] S. De, J. N. Coleman, *ACS Nano* **2010**, *4*, 2713.

[156] A. Kasry, M. A. Kuroda, G. J. Martyna, G. S. Tulevski, A. A. Bol, *ACS Nano* **2010**, *4*, 3839.

[157] D. K. Efetov, P. Kim, *Phys. Rev. Lett.* **2010**, *105*, 256805.

[158] J. Ye, M. F. Craciun, M. Koshino, S. Russo, S. Inoue, H. Yuan, H. Shimotani, A. F. Morpurgo, Y. Iwasa, *Proc. Natl. Acad. Sci.* **2011**, *108*, 13002.

[159] G. Rupprecht, D. M. Ginsberg, J. D. Leslie, *J. Opt. Soc. Am.* **1962**, *52*, 665.

[160] D. Guérard, G. M. T. Foley, M. Zanini, J. E. Fischer, *Nuovo Cim.* **1977**, *38*, 410.

[161] J. E. Fischer, T. E. Thompson, G. M. T. Foley, D. Guérard, Hoke, M, F. L. Lederman, *Phys. Rev. Lett.* **1976**, *37*, 769.

[162] L. R. Hanlon, E. R. Falardeau, J. E. Fischer, *Solid State Commun.* **1977**, *17*, 377.

[163] P. C. Eklund, D. S. Smith, V. R. K. Murthy, *Synth. Met.* **1981**, *3*, 111.

[164] M. Kühne, F. Börrnert, S. Fecher, M. Ghorbani-Asl, J. Biskupek, D. Samuelis, A. V. Krasheninnikov, U. Kaiser, J. H. Smet, *Nature* **2018**, *564*, 234.

[165] K. Persson, V. A. Sethuraman, L. J. Hardwick, Y. Hinuma, Y. S. Meng, A. van der Ven, V. Srinivasan, R. Kostecki, G. Ceder, *J. Phys. Chem. Lett.* **2010**, *1*, 1176.

[166] J. Sun, H. Lee, M. Pasta, H. Yuan, G. Zheng, Y. Sun, Y. Li, Y. Cui, *Nat. Nanotechnol.* **2015**, *10*, 980.

[167] K. P. Chen, F. R. Chung, M. Wang, K. J. Koski, *J. Am. Chem. Soc.* **2015**, *137*, 5431.

[168] K. J. Koski, C. D. Wessells, B. W. Reed, J. J. Cha, D. Kong, Y. Cui, *J. Am. Chem. Soc.* **2012**, *134*, 13773.

[169] C. K. Chan, H. Peng, G. Liu, K. McIlwrath, X. F. Zhang, R. A. Huggins, Y. Cui, *Nat. Nanotechnol.* **2008**, *3*, 31.

[170] B. Feng, Z. Ding, S. Meng, Y. Yao, X. He, P. Cheng, L. Chen, K. Wu, *Nano Lett.* **2012**, *12*, 3507.

[171] S. Hwang, Z. Yao, L. Zhang, M. Fu, K. He, L. Mai, C. Wolverton, D. Su, *ACS Nano* **2018**, *12*, 3638.

[172] C. Cao, H. G. Steinrück, B. Shyam, K. H. Stone, M. F. Toney, *Nano Lett.* **2016**, *16*,

7394.

[173] C. Wang, Q. He, U. Halim, Y. Liu, E. Zhu, Z. Lin, H. Xiao, X. Duan, Z. Feng, R. Cheng, N. O. Weiss, G. Ye, Y.-C. Huang, H. Wu, H.-C. Cheng, I. Shakir, L. Liao, X. Chen, W. A. Goddard III, X. Duan, *Nature* **2018**, *555*, 231.

[174] D. Costanzo, S. Jo, H. Berger, A. F. Morpurgo, *Nat. Nanotechnol.* **2016**, *11*, 339.

[175] K. Ueno, S. Nakamura, H. Shimotani, A. Ohtomo, N. Kimura, T. Nojima, H. Aoki, Y. Iwasa, M. Kawasaki, *Nat. Mater.* **2008**, *7*, 855.

[176] Y. Yu, Y. Yu, L. Huang, H. Peng, L. Xiong, L. Cao, *Nano Lett.* **2017**, *17*, 3613.

CHAPTER 2 – METHODS

2.1 Introduction

In this Chapter, I will present a series of methods that I have developed over the course of my Ph.D. in the hope that these techniques will be useful to future lab members who pursue intercalation research. These methods will include: device design (Section 2.2), electrochemistry (Section 2.3), materials synthesis (2.4), nanosphere lithography (Section 2.5), and thin flake intercalation (Section 2.6). The content in this Chapter will: 1) present unpublished techniques, and 2) provide notes specific to Warren Lab instrumentation. Occasionally, I will refer the reader to other chapters for specific figures that appear in those sections to further clarify a technique.

2.2 Electrochemical Device Design

To characterize intercalation reactions *in-situ*, I designed a planar electrochemical cell that can be used for observing intercalation in bulk and few-layer materials, in both electrolyte- and electrolyte-free environments. The electrolyte and electrolyte-free devices are similar in design, but the electrolyte-free device is more complicated and contains an additional compartment, as described below.

Figures 3-1 and 3-2 (in Chapter 3) show the general steps for fabricating the electrolyte- and electrolyte-free devices. In the first step, we cut SPV-224PR-MJ surface protection tape (Nitto) into strips, and placed them on a standard glass slide (75 mm x 25 mm x 1 mm, VWR)

to form a mask. Then, using a K.J. Lesker PVD Sputter system, we sputtered 10 nm of titanium followed by 100 nm of platinum onto a glass slide. The titanium served to better adhere the platinum to the surface. After sputtering, we removed the tape (Figure 2-2a), rinsed the surface with isopropyl alcohol (VWR), and dried it with N_2. To prepare the highly oriented pyrolytic graphite (HOPG), we cleaved thin strips (100 μm) using tweezers and a razor blade to peel segments off of the bulk crystal. For this step, the razor blade can be used to gently roughen the surface of the HOPG slightly. Scotch tape is also useful for creating splinters of HOPG on the surface that can be grasped with tweezers and pulled away from the surface. It is important to peel the HOPG away slowly, with constant tension, since rapid or inconsistent movements can tear the graphite before a sizeable flake is obtained. Next, we adhered a small piece of conductive carbon double-sided tape to the working electrode side of the Pt substrate. We placed the HOPG on the conductive carbon tape and gently pressed the HOPG with the end of the tweezers (Figure 3-1a and 3-2b). platinum to the surface. After sputtering, we removed the tape (Figure 3-2a), rinsed the surface with isopropyl alcohol (VWR), and dried it with N_2. To prepare the highly oriented pyrolytic graphite (HOPG), we cleaved thin strips (100 μm) using tweezers and a razor blade to peel segments off of the bulk crystal. For this step, the razor blade can be used to gently roughen the surface of the HOPG slightly. Scotch tape is also useful for creating splinters of HOPG on the surface that can be grasped with tweezers and pulled away from the surface. It is important to peel the HOPG away slowly, with constant tension, since rapid or inconsistent movements can tear the graphite before a sizeable flake is obtained. Next, we adhered a small piece of conductive carbon double-sided tape to the working electrode side of the Pt substrate and gently pressed the HOPG flake onto conductive tape with the tweezers.

The main difference between the electrolyte-free and electrolyte devices is the compartment design. For the electrolyte-free device, we sandblasted three sets of coverslips (24 mm x 40 mm x 0.17 mm, Thermo Fisher Scientific) (Figure 3-1a-c). The first set of two coverslips (CA) had the centers sandblasted out with a rim of ~5 mm and a small notch at the end adjacent to the graphite (Figure 3-1a and 3-2c). The second set of five coverslips (CB) had the centers sandblasted with a rim of ~ 5 mm (Figure 3-1b). The final coverslip (CC) had a hole sandblasted approximately 10 mm from the edge of the slide (Figure 3-1c).

For the electrolyte device, only the CB and CC were required (Figure 3-1b, c). We used seven to ten coverslips of CB and one CC. In both devices, these components were adhered over the surface of the microscope slide using epoxy (Hysol 9340, Loctite) and cured at 80 ^{o}C for 2 hours or at 160 ^{o}C for 30 minutes. Generally, it is helpful to first adhere the corners of the electrolyte well and cure. Then, with the corners stable, the edges are easier to epoxy and cure. In addition, an aluminum foil sheet placed on the surface of the hot plate prevents the devices from sticking to the hot plate as they cure.

To fabricate the electrolyte-free device (Figure 3-2e), one important consideration is that creating a barrier between the electrolyte and electrolyte-free compartments requires a thin strip of epoxy across the surface of graphite. Although the epoxy can be applied directly to the surface of graphite, the epoxy is not compressible as the graphite expands during intercalation. Thus, there is significant strain that results when ions intercalate into the graphite directly under the barrier. To overcome this problem, we took a small piece of Kapton tape, rolled it to form a thin cylinder and placed it on the graphite at the intersection of the two compartments. Then, the electrolyte well can be assembled by placing CA, CB, and CC over the surface of the microscope slide, sealing with epoxy and curing.

Next, the electrolyte-free well consisted of seven coverslips (CD) sandblasted as depicted in Figure 3-1d. Another coverslip (CE) (Figure 3-1e) was placed on top of these coverslips and these components were adhered over the surface of the microscope slide using epoxy (Figure 3-1f, 3-2e). We found that in an oxygen environment, the graphite reached stage 2 and then began to over-oxidize and degrade in the electrolyte-free compartment. In an oxygen-free environment, however, the material readily transformed from stage 2-1 in the electrolyte-free region. Thus, we sealed the electrolyte-free region in the glovebox before bringing the device out for intercalation. To summarize, the ordering for the electrolyte-free device is: electrolyte compartment: CA (Figure 3-1a), Kapton barrier (Figure 3-2c), CB (Figure 2-1b), CC (Figure 3-1c), seal and cure. Then, the ordering for compartment 2 in the glovebox is: CD (Figure 3-1d), CE (Figure 3-1e), seal and cure. For both the electrolyte and electrolyte-free devices, we applied electrical contacts on the working, counter, and reference electrodes using copper tape and covered the contacts with electrical tape (Figure 3-2d). Occasionally, there may be some issues with the copper tape adhesion. If this occurs, epoxy can be applied over the surface of the copper tape and cured before proceeding to the next step.

To fill the electrolyte well, we prepared a solution of 15 M H_2SO_4, by slowly adding 98 % sulfuric acid (VWR) to the DI water in a 10 mL vial. Then, we pipetted ~ 2 mL into the hole on the electrolyte side. We then sealed the hole with a square glass coverslip (24 mm x 24 mm, Thermo Fisher Scientific) and epoxy (Hysol 9340, Loctite). We did not cure the epoxy this time, since electrolyte was present. Instead, we covered over the wet epoxy with electrical tape and it dried naturally during intercalation.

2.3 Electrochemical techniques

For electrochemical measurements, we performed both galvanostatic and potentiostatic experiments. In particular, chronopoteniometry (CP) provided helpful insight into the staging dynamics observed during intercalation. Here, I will present a description of the CP technique we used for bulk materials, respectively. The electrochemical characterization of ultrathin flakes is described in Section 2.6.

2.3.1 Setting up the Electrochemical Measurement

For electrochemical measurements, we used a Bio-Logic SP-300 or SP-200 instrument to apply a constant current or linear voltage ramp, depending on thte technique. We used a 3-electrode measurement and connected the leads to the (red to working, blue to counter, and white to reference). If using a two electrode measurement, there is a port behind the head of the blue cable to connect the reference. If the potentiostat is having trouble connecting to the laptop, there maybe several issues. 1) The potentiostat may not be plugged in or have power. Try plugging in the potentiostat or flipping the power switch. 2) The laptop might be connected to Wifi and the IP address of the potentiostat is no longer recognized. In order to connect, the IP address of the laptop must match the IP address of the potentiostat. Occasionally, when connected to Wifi, the IP address will change and the laptop no longer can communicate with the potentiostat. In general, it is advisable to keep the computer attached to the potentiostat off-line, since the IP address of the computer is dynamic and changes periodically. Turn off the Wifi and find the new IP address of the computer by opening the command prompt, running ipconfig, and writing down the IP address provided. Then, set-up a new device and for the IP address of the potentiostat, type in the new IP address of the computer and add a "1" to the end of the address. If the problem is with the IP address communication, this solution should take

care of the issue. Once the potentiostat is connected to the laptop, the experiment can be set-up to run automatically.

2.3.2 Intercalation of Bulk Graphite using CP

For CP, we applied a current between 0.07 mA – 0.09 mA for 2 hours for the electrolyte intercalation and 24 hours for the electrolyte intercalation. Since the electrolyte-free intercalation can take up to 24 hours, it may be useful to remotely-control the experiment from home, depending on the measurements of interest.

In the intercalation of bisulfate into graphite, graphite is oxidized when HSO_4^- intercalates through an anodic reaction. Since this reaction is slightly non-spontaneous at room temperature[1], it is necessary to employ electrolysis to drive the intercalation by positively biasing the graphite working electrode. To form well-staged compounds electrochemically in the bisulfate-GIC, a low current density can be applied and the resulting voltage output measured over time.[2] This chronopotentiometric technique has been widely used to characterize staging in bulk intercalation compounds.[2–4] Figure 2-1 shows the chronopotentiogram for the intercalation of bisulfate into bulk HOPG.[2] The graph shows a series of plateaus (B-C) and linear voltage ramps (A-B and C-E), which indicate staging within the material. The plateau regions correspond to a biphasic equilibrium mixture between two stages.[5] For example, in B-C, stages 2 and 1 are at equilibrium with each other as the stage 2 compound is being converted to stage 1. At the inflection points (A and C), the mixture has been completely converted to a pure stage compound. The subsequent increase in voltage is due to the process of overcharging the pure stage. In the region A-B, overcharging of stage 2 results from the deprotonation of the sulfuric acid molecules in-between the layers to form

bisulfate and further oxidize the graphite.[2,5] A similar process occurs for stage 1 in the C-E regime. However, beyond D, all of the sulfuric acid has been converted to HSO_4^-. Thus, in this case, it has been suggested[2] that overcharging from D-F consists of the peroxidation of HSO_4^- to $S_2O_8^{2-}$. To deintercalate the material, a negative current can be applied to the system, and a chronopotentiogram with a series of plateaus that decrease, rather than increase in voltage over time as the graphite is reduced. CP can be used to intercalate (deintercalate) other species, using a positive (negative) current for acceptors and a negative (positive) current for donors. The optical microscopy and spectroscopic results obtained during CP are discussed in Chapter 3.

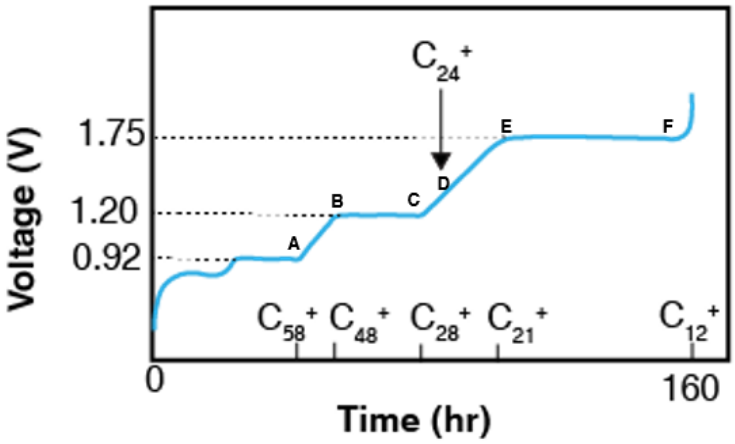


Figure 2-1: Chronopotentiogram for bulk HSO4- GIC. At point A) Pure stage 2 forms. A)-B) represents the overcharging region where H_2SO_4 molecules deprotonate to form HSO_4^- and H^+ is expelled. In this regime, the potential increases as the working electrode becomes more positively charged. The plateau in B)-C) shows the biphasic equilibrium between a mixture of stage 2 and stage 1. At C), the compound is completely converted to stage 1. C)-D) is the stage 1 overcharging region. Point D) indicates the formation of C_{24}^+, all H_2SO_4 has been converted to HSO_4^-. From D)-F) the peroxidation of HSO_4^- to $S_2SO_8^{2-}$ occurs. **(Chronopotentiogram reproduced from Reference[2]).**

2.4 Synthesis of CVD graphite

Although we were able to intercalate bulk graphite in the electrolyte-free device, mechanically-exfoliated flakes are not compatible with electrolyte-free intercalation, since their lateral sizes are insufficient to span the barrier required to separate the two compartments. Thus, to perform electrolyte-free intercalation using the device we designed in 2.2, we turned to chemical vapor deposition (CVD), a synthetic technique that is well-known for creating large-area, wafer-scale graphene.[6–9] My colleagues, Jack Sundberg and Adi Pillai, designed the general synthesis route that I used to synthesize the FLG (Section 2.4.1) and I will briefly summarize their procedure. Once I synthesized the FLG, I developed a set of procedures to transfer the FLG to a new substrate (Section 2.4.2) and intercalated the transferred material (Section 2.4.3). Due to the transfer process, intercalation of the CVD FLG presented unique challenges, which I also discuss in Section 2.4.3.

2.4.1 Substrate Preparation

For CVD synthesis of monolayer graphene, the standard substrate is copper[7], since the low carbon solubility (<0.001 % atomic weight) of polycrystalline Cu contributes to a surface-controlled growth mechanism[7,10]. However, with a Ni catalyst, the growth mechanism is a 2-step process[10]. In the first step, the carbon atoms diffuse into the Ni substrate and in the second step, the carbon difuuses out as the substrate cools. This mechanism facilitates growth of few-layer to multilayer graphite synthesis[9,10]. We selected Ni metal (99.99 % purity), and cut the metal into pieces approximately 2 in x 0.5 in. Before synthesizing the FLG, it was important to etch the surface of the Ni substrate. The cleaning solution consisted of a 1:1:1 solution of ethanol:acetic acid:DI water. Since each substrate must be etched before synthesis,

the solution can be made in larger quantities (50-100 mL or larger) and stored until needed. We poured the solution into a 10 mL vial and placed the Ni substrate in the solution. The vial was sonicated for 15 minutes. Then, the Ni was removed, rinsed with DI water, and dried with a Kim wipe. To prevent any surface layers from forming after the cleaning process, the substrate was transferred immediately into the CVD set-up before synthesis.

2.4.2 Few-layer graphite synthesis

To set-up the CVD system, the vacuum pump below the hood was turned on and the butterfly valve was kept closed (vacuum only pulled up to the butterfly valve at this point). Then, the Ni substrate was placed into the glass boat inside the quartz tube, and the magnet was used to pull the substrate to the far end of the quartz tube (on the side closer to the MFC flow controllers). Then, the connection was tightened over the left end of the quartz tube (finger tight). With the MFCs closed, we opened the Argon/H_2 and methane valves on the gas cylinder. The butterfly valve was opened followed by the MFC controller valve to purge the quartz tube with Argon/H_2 before synthesis for 5 minutes. After 5 minutes, we opened the CVD interface to set the Ar/H_2 flow rate and closed the butterfly valve to allow the pressure to reach atmospheric pressure. The pressure will be modulated by the needle valve during the rest of the synthesis. The furnace was turned on and allwed to ramp up to 1000 ^{o}C over 45 minutes. During this step, the Ni substrate was not in the furnace. After 45 minutes, the substrate was moved into the furnace using the magnet. Note, care should be taken to avoid cracking the tube with the magnet, as Ar/H_2 passes through the tube. Also, full PPE should be worn including heat-resistant gloves. The substrate was annealed in the furnace for 15 minutes. Then, the methane flow was set to 100 sccm and the growth occurred over 1 hour and 15 minutes. After

the growth period, the furnace was allowed to cool down. The methane was kept flowing during the cool-down process to prevent desorption. After the furnace had cooled to approximately 400 ^{o}C, the furnace was opened, proppped open with heat resisant insulation, and allowed to cool down to room temperature. Once the furnace had cooled, the methane flow was turned off, the valve to the quartz tube was opened, and the Ar/H_2 was turned off. Then, the vacuum pump can be turned off along with gas cylinder valves and the substrate removed.

Importantly, the FLG synthesis described above did not result in few-layer graphite, as we discovered with AFM. Instead, the thicknesses were on the order of 450-950 layers and would be considered bulk graphite rather than few-layer or even ultrathin graphite. For the sake of continuity, however, I will continue to refer to the synthezied material as FLG, but the reader should know that it was actually multilayer graphite.

2.4.3 Transfer to new substrate

Substrate transfer is a standard process after CVD synthesis, since the original substrate is not generally useful for most applications[6]. For electrochemical intercalation of bisulfate into graphite, Ni is unsuitable as a substrate, since sulfuric acid oxidizes Ni to form Ni^{2+} and H_2 (g).[11] Therefore, the FLG must first be transferred to a Pt substrate (See Section 2.2 for a description of the Pt substrate) to create the working electrode before fabricating the electrochemical cell. The transfer technique involves a 5-step process: 1) Coat PMMA on FLG 2) Dissolve away the original substrate, 3) Clean the synthesized graphite, 4) Transfer the graphite to the new substrate, 5) Remove the PMMA layer.

In the first step, I placed the FLG/Ni substrate on the spin coater, under vacuum and cleaned the surface with the Gust 360 Duster. Then, I added 1-2 drops of a 2% PMMA (MW

950,000) solution in anisole (950 PMMA A2) to the surface. For smaller substrates, 1 drop may be sufficient, whereas for a larger substrate 2 drops may be required. The PMMA serves to stabilize the FLG and prevent it from fragmenting throughout the transfer process. After pippetting the PMMA, I spin-coated the substrate at 2500 rpm for 60 seconds to give a target thickness of 78 nm for the PMMA. The thickness of the PMMA can be tuned by changing the RPM of the spin coater, if necessary.[12] However, I found that the PMMA thickness this method produced was thick enough to stabilize the FLG during transfer, yet thin enough to be removed in step 4. After spin-coating, the PMMA was cured at 110 ^{o}C for 30-45 minutes, before proceeding with subsequent transfer steps.

Next, we selected a 2 M iron (III) chloride ($FeCl_3$) solution as the dissolving agent for Ni. To create this solution, we added 10 g of $FeCl_3$ to DI water in a 50 mL jar to create a 2 M solution, placed the jar on a stir plate, and heated the mixture at 70 ^{o}C to dissolve the $FeCl_3$. After 30 minutes of stirring, the $FeCl_3$ was dissolved and I poured the $FeCl_3$ into a medium glass petri dish, about two-thirds of the way up the sides of the glass. Then, I placed the PMMA/FLG/Ni wafer on the surface of the solution, with the Ni side immersed in the solution (Figure 2-2a). Since Ni is magnetic, it was attracted to the stir plate or stir bar and stuck to the bottom of the petri dish. Therefore, I placed it on a non-magnetic hotplate at 70 ^{o}C without stirring. Due to the thickness of the Ni foil and the lack of stirring, the dissolution process can take up to 24 hours. Consequently, the petri dish can be covered with a watch glass to allow the dissolution to complete overnight. It is important to note that the $FeCl_3$ solution readily contaminates surfaces, particularly glass. Even after extensive cleaning procedures, the beakers and petri dishes still show residual $FeCl_3$. Thus, only designated beakers and petri dishes should be used for the transfer procedure.

Once the Ni was dissolved, I removed any remaining $FeCl_3$ solution via pipetting and then added 3 M HCl to the petri dish (Figure 2-2b). Then, I removed the HCl and replaced it 3-5 times, until the solution no longer had a yellow color. Finally, I repeating the pipetting steps using DI water 3 times to remove any remaining chlorine contaminants. At this point, the PMMA/FLG is fragile, so care should be used when adding and removing HCl or water.

After cleaning the PMMA/FLG, a new substrate was placed in the petri dish and oriented under the PMMA/FLG. Then, the HCl was slowly pipetted out of the petri dish until the PMMA/FLG settled on the surface of the new substrate. Residual solution was still present between the FLG and the substrate. To remove the it, I allowed the PMMA/FLG to dry in air for ~30 minutes to 1 hour. If the transfer process is successful, the film will adhere to the substrate. If it is unsuccessful, the PMMA/FLG may crack or tear as the film dries. Annealing exacerbated the cracking, but room temperature drying showed the best results (Figure 2-2b).

To clean the PMMA off of the FLG, I soaked the substrate in electronic grade acetone for ~4 hours. It should be obvious by eye when the PMMA has dissolved, since the FLG will no longer have a visible film on the surface. After the PMMA was removed, I rinsed the FLG with electronic grade acetone followed by IPA and dried it with N_2.

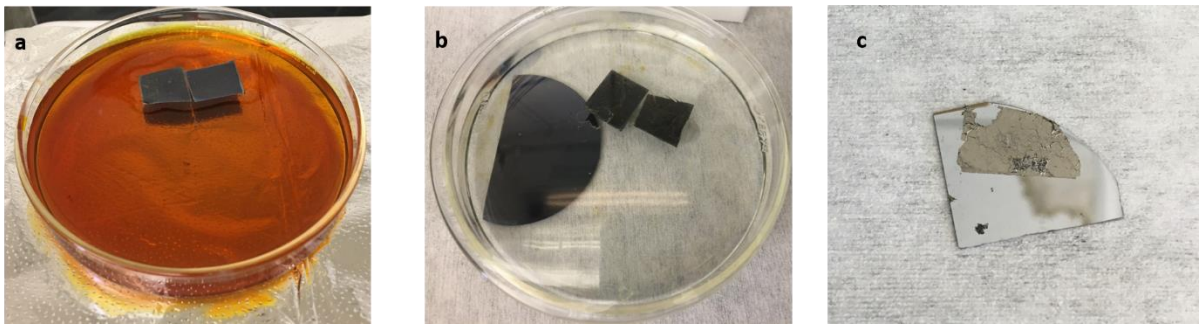


Figure 2-2: Transfer process for FLG. a) PMMA/FLG/Nickel substrates float on the surface of $FeCl_3$. b) New substrate sits underneath the PMMA/FLG after cleaning with DI water. c) FLG on a Si substrate after transfer and annealing.

2.4.4 Characterizing the transferred film

With only 1-2 rinsing steps, the transfer process resulted in iron and chlorine contamination, based on X-ray photoelectron spectroscopy (XPS) (Figure 2-3a,b). Therefore, it is recommended to we cleaned the substrate 3-5 times with HCl, and rinse with DI water 3 times, to further clean the substrates. In addition to contaminants, we also looked at the surface of the FLG using scanning electron microscopy (SEM) to observe whether there were large holes or tears in the material (Figure 2-4). Finally, we characterized the thickness using AFM (450-950 layers) and performed Raman spectroscopy at multiple points on the surface of the graphite to determine if the transfer process had induced defects in the FLG (Figure 2-5). Although several of the spectra taken near the edges of the material had a prominent D-peak near 1330 cm^{-1} (Figure 2-6a), most did not have a D-peak (Figure 2-6b), indicating regions of high quality graphite.

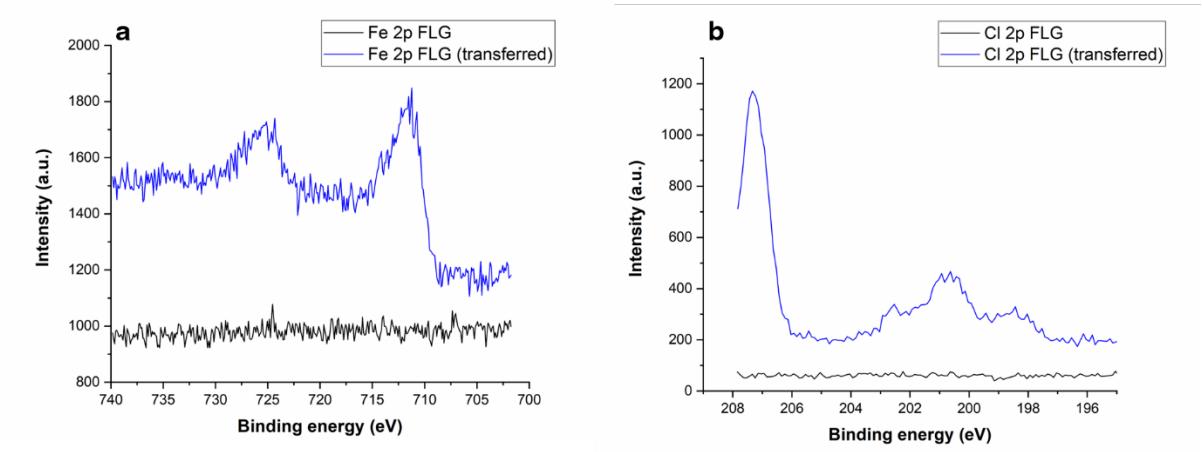


Figure 2-3: XPS spectra of FLG surface showing the presence of a) iron and b) chlorine on the surface of the FLG.

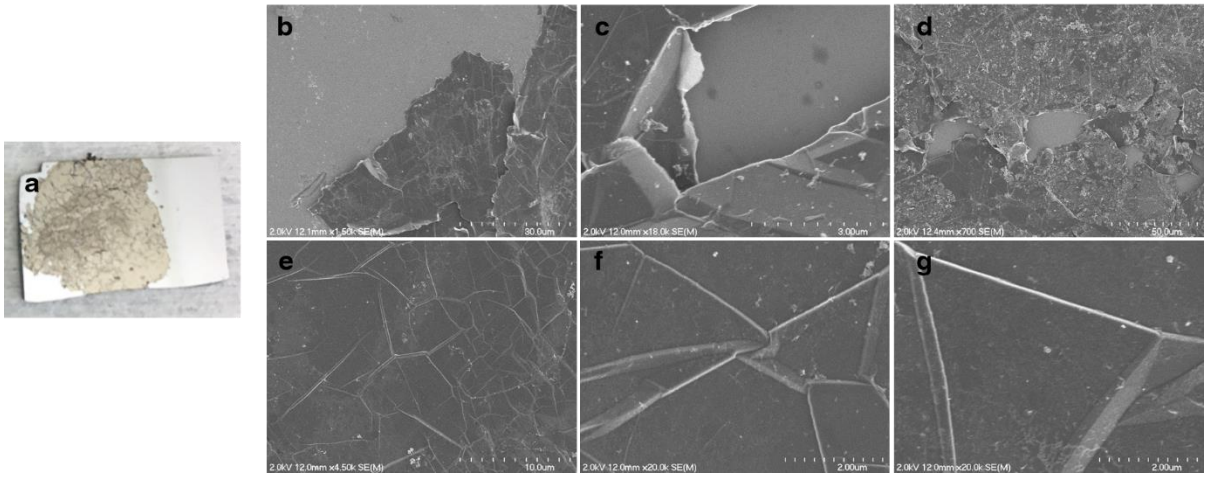


Figure 2-4: Characterizing the FLG after transfer. a) image of transferred FLG on a Si substrate before SEM characterization. SEM images of the b),c) edges, d) defective regions, and e)-g) center of the transferred FLG.

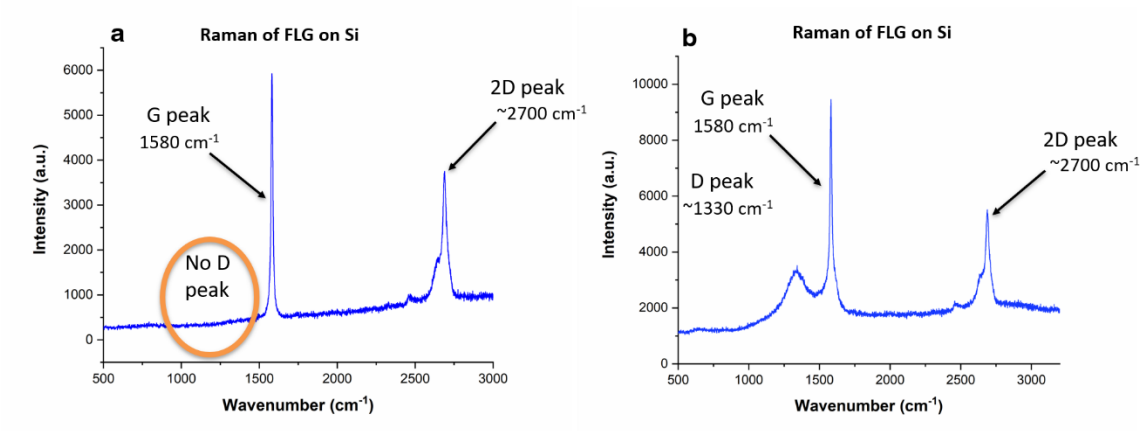


Figure 2-5: Raman spectra of transferred FLG with a) center of the transferred FLG, showing the absence of a D-peak and the b) edges and visibly defective regions showing the presence of a D-peak.

2.4.5 Initial intercalation results

Once I transferred the FLG to the Pt substrate, I fabricated an electrochemical cell (as described in section 2.2) to characterize intercalation in the thin film. Figure 2-7 shows a series of optical microscopy images of bisulfate intercalation in FLG. As these images demonstrate, the color sequence appeared to represent that of bulk rather than ultrathin graphite, which agreed with our AFM measurements. However, the color sequence is slightly different, with some regions going directly from the yellow orange color to blue without the intermediate steps. Other regions, however pass through the full sequence of colors, but more rapidly, indicating that local structure, potential, and thickness likely affect the stage transition. Moreover, there were significantly more wrinkles and rippling that occurred during intercalation. These effects were likely due to partial delamination of the graphite, which we observed macroscopically. Based on the initial results and observations, there are several opportunities to optimize the procedures to advance this project further. For example, it would be important to adjust the methane flow parameters to tune the number of layers down to

ultrathin. Using a thinner Ni substrate could also promote synthesis of a thinner graphite sample. Moreover, the adhesion between the Pt substrate and the graphite must be improved, so that the graphite does not delaminate during intercalation.

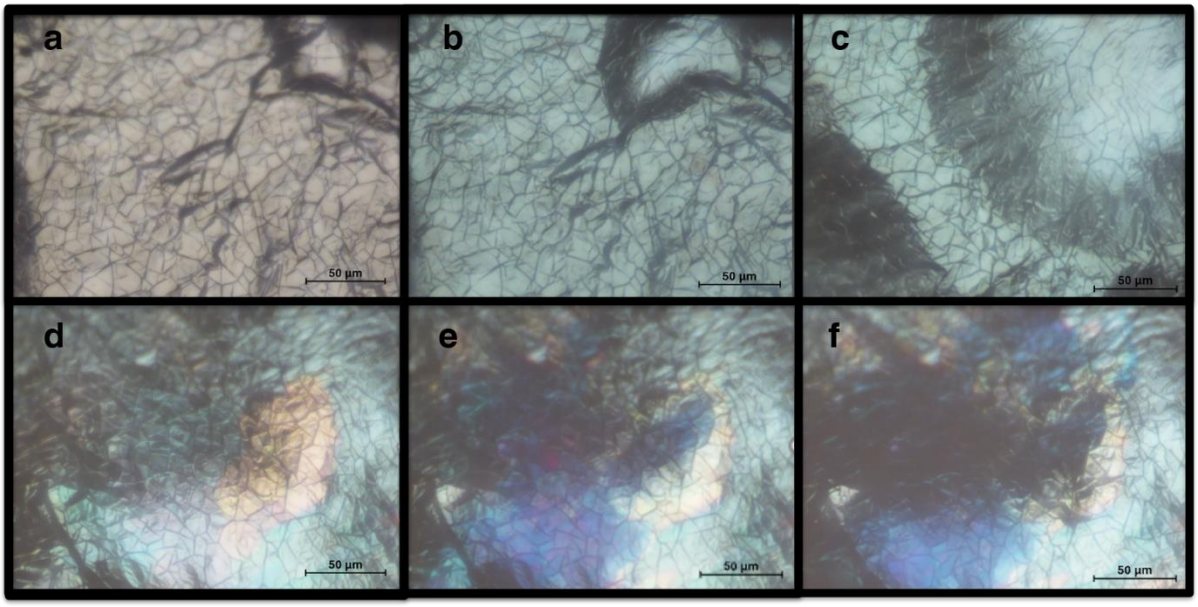


Figure 2-6: Optical microscopy images of the intercalation of transferred graphite. a) Before intercalation, b) Stage 2, c) bubble forming during stage 2, d)-e) stage 2-1, and f) incomplete intercalation.

2.5 Nanosphere Lithography (NSL)

Nanosphere lithography is a method that is developed by the Van Duyne group at Northwestern University[13]. In general, this patterning process enables the fabrication of plasmonic nanostructures without the complexities of e-beam lithography or polymer techniques. We attempted to use this method to fabricate holes in few-layer graphene to observe how intercalation tunes the plasmonic response. We modified a synthesis route that

has been described in a paper by the Liu group[14]. This method involves a 7-step process (Figure 2-7): 1) FLG synthesis (Section 2.4.2), 2) Nanosphere deposition, 3) Alumina deposition, 4) Nanosphere removal, 5) O_2 plasma etch, 6) Alumina removal, 7) h-FLG transfer (Section 2.4.3). It should be noted that SEM characterization before and after each step of the process for each substrate is paramount to ensure that the process is working. XPS is also informative for steps 6) and 7) to reveal any contaminants or oxidation induced by those steps.

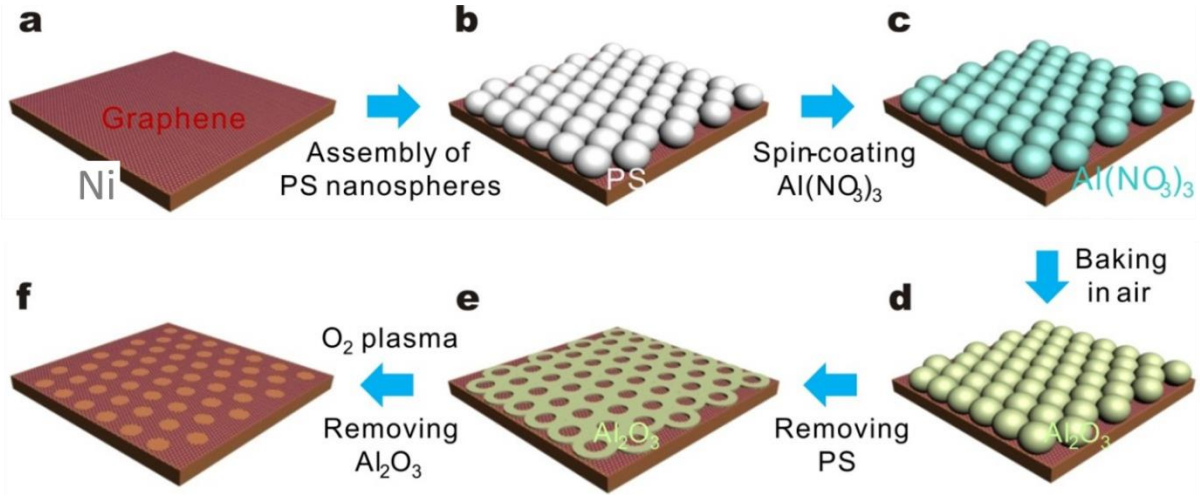


Figure 2-7: Sequence of steps to make h-FLG a) CVD of FLG on Ni substrate, b) spin-coating PS spheres on the surface of the FLG, c) spin-coating aluminum nitrate over the spheres, d) annealing to form alumina, e) Removing the PS spheres in a toluene bath, f) O_2 plasma to etch the graphite and phosphoric acid bath to remove the alumina. (Adapted and Reproduced from Reference [14]).

The FLG synthesis is described in Section 2.4.2. After synthesis, we deposited nanospheres on the surface of the FLG. After testing several other methods (LB Trough, controlled liftoff), we decided to use spin-coating to deposit the nanospheres on the surface of FLG, since it seemed to be more reproducible, based on our observations. To make the solution

of PS spheres, we added a solution of methanol/triton-X-100 (400:1 ratio of methanol: triton-X-100 (a stabilizer) to untreated polystyrene spheres (300 μm diameter) in a 1:1 ratio. The FLG/Ni substrate was placed on spin-coater under vacuum and 50 μL of the PS solution were pipetted on the surface of the FLG. Table 2-1 shows the steps that we found gave the best results, based on literature[15]. Ideally, the PS will form a monolayer with surface coverage greater than 90%. Using the method described in Table 2-1, we observed good monolayer coverage although it was less than 90 % (Figure 2-8).

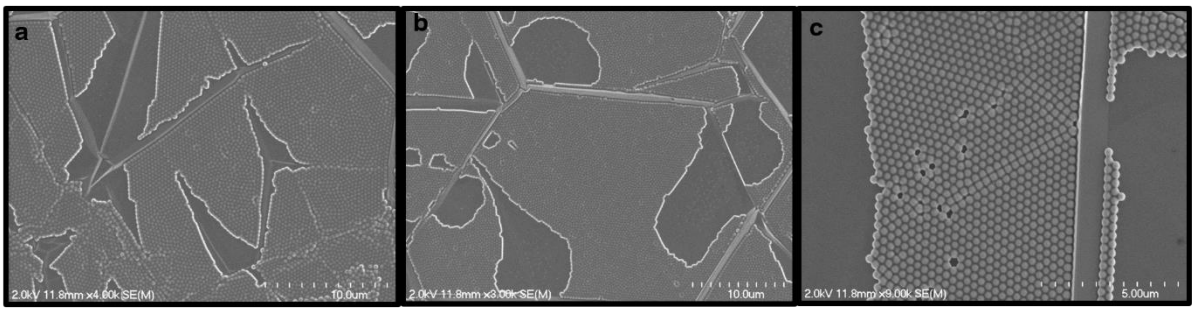


Figure 2-8: SEM images of the PS spheres on the surface of the FLG. The coverage is monolayer, rather than bilayer observed in other deposition methods.

After depositing the PS spheres, we then deposited the alumina layer using spin-coating. We made a 0.25 M $Al(NO_3)_3$ solution consisting of 400:1 H_2O/Triton-X as the solvent and pipetted 50-100 μL on the surface of the PS/FLG/Ni. The parameters for spin-coating were 35 s at 8000 rpm with an acceleration of 600 rpm/s. Then we oxidized the aluminum nitrate on a hot plate at 80 ^oC for 30 minutes. Once the alumina had been formed, we removed the PS spheres by soaking the substrate in toluene bath for 5 minutes. Soaking the substrate for too long resulted in the alumina being completely destroyed, whereas a shorter time left residual PS spheres on the surface. In this case, the toluene etched away the PS, leaving a holey alumina mask on the surface of the graphite (Figure 2-9).

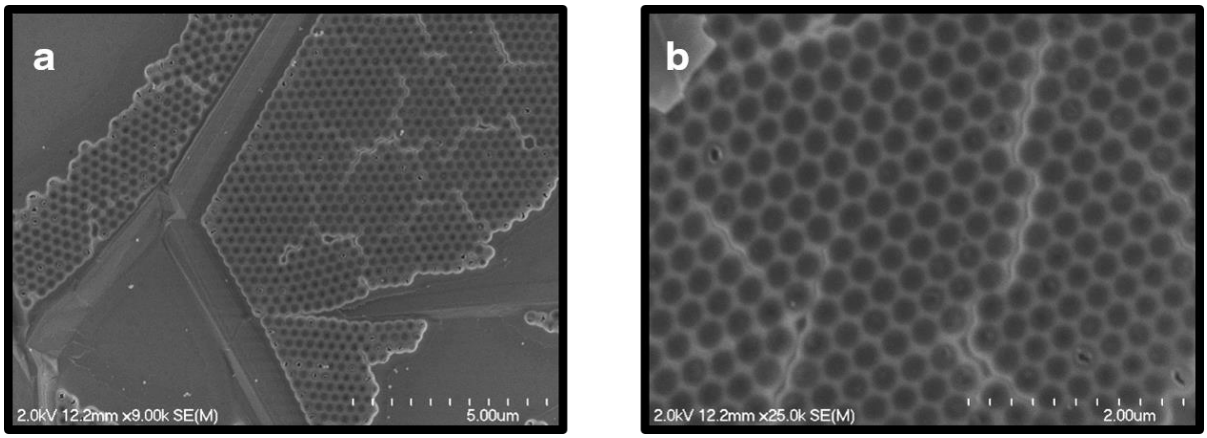


Figure 2-9: SEM images of the alumina mask after removal of the PS spheres on the surface of the FLG. The magnification is a) 9.00 k and b) 25.0 k.

The exposed graphite surface can then be etched away using O_2 plasma. Unfortunately, we were unable to accomplish this step, due in part to variable conditions in the O_2 plasma environment in the cleanroom as well as the fact that our CVD graphite was actually bulk, rather than few-layer graphite. However, with some of the recommendations described in Section 2.4.5, we might be able to obtain CVD graphite that approaches few-layer. Moreover, our new ALD setup in lab will also offer an O_2 plasma attachment, enabling us to finely control the etch rate for graphite and form a holey mesh. Therefore, we continued to develop a protocol for the subsequent steps so that once the O_2 plasma attachment was ready for use and the CVD parameters were optimized, the synthesis could easily be completed. Once the FLG is etched by the O_2 plasma, the alumina mask can be removed. Before removing the alumina, we characterized the surface with XPS (Figure 2-10), to ensure that the alumina was present. Then, we prepared an 8% solution of phosphoric acid in water and soaked the substrate for 1 hour at 80 ^{o}C and then rinsed them with IPA. We took XPS spectra at the Al 2p energies (Figure 2-

10a) to determine whether the alumina had been removed. The spectra show that the Al peak was present when alumina was present on the surface, as expected (red line). After removing the alumina with phosphoric acid, the Al peak disappears (blue line) to match the spectra of FLG (black line). To observe whether the phosphoric acid was still present after soaking in the solution, we took measurements at the P 2p energies (Figure 2-10b). The appearance of the P 2p peak (blue line) indicated that the rinsing process after the soak was likely not sufficient and that phosphate groups were present on the surface of the FLG. We also looked at the C 1s (Figure 2-10c) peak to determine whether either the alumina deposition or removal had oxidized the surface of the graphite. There was a broad feature near 290 eV, which could correspond to an oxidized carbon shift, but it was not intense in any of the spectra. Based on these observations, we determined that the phosphoric acid removal was successful, we needed to use a shorter soak time to minimize bubble formation on the surface of the graphite (Figure 2-10a, inset). We repeated the deposition and removal process, selecting 30 minutes for the soak time and using a more rigorous rinsing procedure. Importantly, the shorter soak time did not induce any bubble formation (Figure 2-11, Inset). Moreover, the XPS spectra showed no alumina on the surface (Figure 2-11a) and a less intense P 2p peak (Figure 2-11b). This indicates that shorter soak times combined with better rinsing results in alumina removal and less contamination.

Once the holey FLG has been fabricated, it can be transferred using the methods described in Section 2.4.3. Although we were unable to complete the full synthesis, due to the challenges listed above, the methods described here have the potential to enable another student to finish it in the future, provided the CVD and O_2 plasma parameters are optimized.

Table 2-1: Spin-coating procedure for NSL, outlining the RPM, acceleration, and durations[15].

Stage	RPM	Acceleration (s^{-1})	Duration (s)	Phase	Dominant Force	Effect
A	150	200	120	Spin-up	gravity	solution spreads over substrate.
A2	250	200	120	Spin-up	_____	coverage improvement
B	800	200	60	Spin off	centrifugal force	disordered monolayer partially forms.
C	2500	200	20	Spin off	_____	solvent volume reduction. NPs adhere to surface.
C2	5000	200	20	Self-ordering	Surface tension	Hexagonal packing
D	8000	1000	360	Drying	_____	Monolayer; hexagonal packing

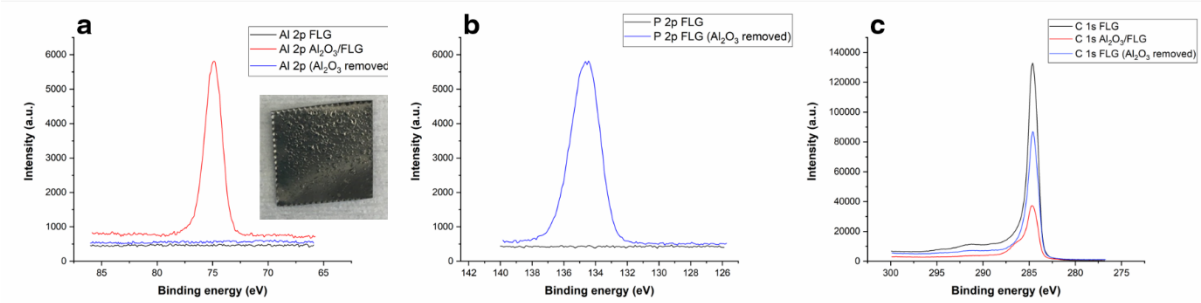


Figure 2-10: XPS for the alumina mask before and after removal using a 1-hour soak. a) The Al 2p peaks on FLG with no alumina deposited (black), after alumina deposition (red), and after alumina removal with phosphoric acid (blue). Inset: image of FLG surface after alumina removal. b) P 2p peaks on FLG before alumina deposition (black) and after removal of alumina with phosphoric acid (blue). c) C 1s peaks for FLG with no alumina (black), with alumina (red), and after alumina removal (blue).

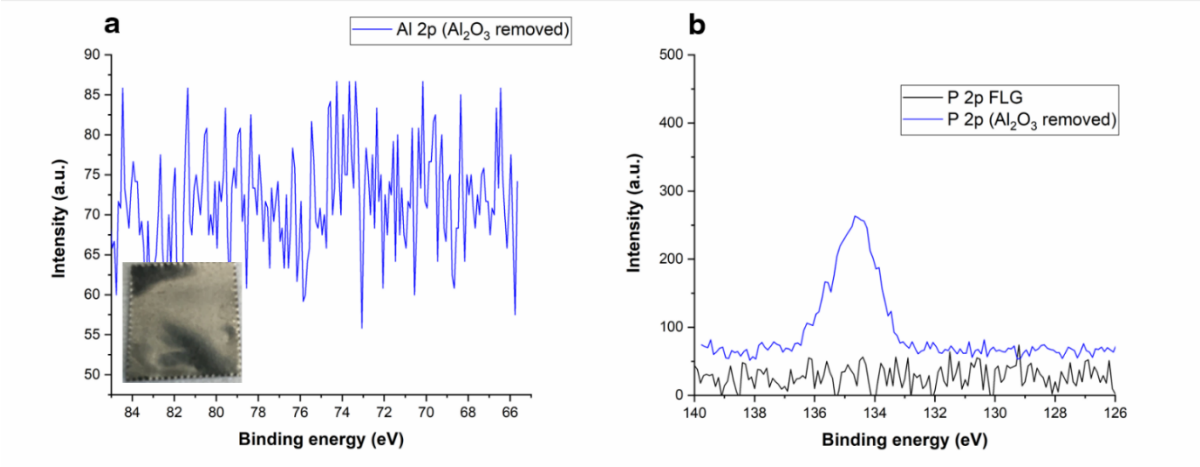


Figure 2-11: XPS for the alumina mask after removal using a 30-minute soak. a) Al 2p peaks after alumina removal. Inset: image of FLG surface after alumina removal. b) P 2p peaks on FLG before alumina deposition (black) and after removal of alumina with phosphoric acid (blue).

2.6 Ultrathin Flake Intercalation

2.6.1 Mechanical exfoliation to form the working electrode

To fabricate the working electrode, graphite flakes were mechanically-exfoliated using the Scotch Tape Method[16]. This technique takes advantage of the weak interlayer (vdW) forces between the layers of graphite and mechanically peels the layers of graphite apart, through successive exfoliations. To accomplish this, a piece of Scotch tape was pressed, sticky-side down onto the surface of the HOPG. Then, the tape was peeled away, removing the surface layers of the HOPG. At this point, the graphite flakes were still thick, albeit thinner than the bulk crystal. To make the flakes thinner, the piece of tape was folded in half and and then peeled apart. Repeating this process 10-12 times resulted in flakes in the ultrathin to few-layer regime. After mechanical exfoliation, the tape pressed onto the sputtered Pt surface (described in Section 2.2) to form the working electrode.

In our original exfoliation method, we pressed the tape onto the surface of the Pt and rubbed for several seconds with tweezers to transfer the flakes. Generally, this technique did not result in a large number of exfoliated flakes (Figure 2-15a), since it was difficult to ensure that each region of the tape received the same level of pressure. To solve this problem, we cut the piece of tape containing the graphite flakes into a smaller piece, (about the size of the Pt surface comprising the base of the working electrode) before placing it directly on the Pt surface. Then, we used a longer transfer time and rubbed the back of the tape with the tip of a pair of tweezers, using small, circular motions for several minutes. It was also helpful to monitor the exfoliation process under the optical microscope to ensure that the flakes were being transferred and identify regions that required targeted pressure. After transfer, the

cleaning steps outlined in the methods remained unchanged. Figure 2-15 shows the optical microscopy results using the original method (Figure 2-15a) and using the new exfoliation method (Figure 2-15b). The modified technique provides a clear advantage over the original, with a larger number of flakes consistently present.

Many of the flakes had tape residue remaining after exfoliation, which interfered with optical measurements. To minimize the amount of residue, we washed the flakes in a 3:1 acetone:toluene bath. The solution was prepared by adding 3 parts acetone to 1 part toluene in a graduated cylinder, with a cap. Then, the cylinder was shaken gently before pouring the solution into a medium-sized glass petri dish on a stir plate. Next, the electrode was added along with a medium stir bar. (Note: multiple electrodes can be washed at one time, provided the petri dish and stir bar are large enough and there is sufficient cleaning solution). The stir plate was set to a medium speed to keep the solution moving across the surface of the electrodes. It was important to stir the solution constantly to help remove the tape residue and keep it from resettling onto the surface of the electrode. After 10-15 minutes, we removed the electrode from the dish using tweezers and rinsed it immediately with IPA to wash off any residual tape before it re-adheres. Then, the electrode was washed again at the sink with acetone and dried with N_2. After the electrode was washed, we checked the surface under the optical microscope to make sure that tape residue was not readily visible and to ensure that flakes were still present.

2.6.2 Device design and electrochemistry

The details for the electrochemical device are described in Section 2.2. No structural modifications were required for the electrolyte device. We performed cyclic voltammetry (CV)

to observe the electrochemical processes in the cell, using the following parameters for the best results: Scan rate: 10 mV/s, Voltage ranges: 0 – 1.0 V. The number of cycles ranged from 1 to 10 cycles, depending on the characterization techniques.

2.6.3 Optical microscopy

Optical images and videos were acquired *in-situ* using a Nikon Eclipse E600 microscope, equipped with a Nikon T Plan 50X SLWD objective with an N.A. of 0.40. Videos were recorded at 1 fps, with an MJPEG compression to reduce the file size.

2.6.4 Raman spectroscopy

Raman spectra of the ultrathin bisulfate-graphite intercalation compounds were obtained *in-situ* using a Renishaw Raman instrument, a 633 nm laser line, and a Nikon T Plan 50X SLWD objective with an N.A. of 0.40. Since the flakes intercalate rapidly, we performed static scans centered at 1580 cm^{-1} during intercalation. We also performed chronoamperometry during the Raman measurements, selecting the constant voltage values to correspond to peaks in the cyclic voltammogram.

2.6.5 Characterizing the intercalation of ultrathin flakes

To fabricate the ultrathin electrode, we mechanically exfoliated HOPG flakes onto a conductive Pt substrate. Then, we fabricated an electrochemical cell to monitor intercalation events *in-situ*, with optical microscopy and spectroscopy. To electrochemically intercalate the flakes, we performed cyclic voltammetry (CV), enabled us to observe electrochemical processes with cycling. For our initial CV scans, we applied a voltage ramp from 0 to 2.0 V

with a scan rate of 10 mV/s to identify the voltage window of intercalation. Figure 2-12 shows the corresponding current output. Although large peaks in current have been detected during both the anodic scan (intercalation) and the cathodic scan (deintercalation) of bulk graphite[17], we did not observe these peaks during our preliminary CV scans for the ultrathin flakes (Figure 2-12). However, when we coupled CV with *in-situ* optical microscopy, we observed distinct changes in both the color and morphology of the flakes with cycling (Figure 2-13), which suggested a series of intercalation events.

To investigate why we did not observe peaks in the cyclic voltammogram, we took a series of optical microscopy images of the electrode surfaces (Figure 2-14a). These images revealed that the flake coverage across all electrodes was sparse, consisting mostly of isolated flakes with a few larger clusters of flakes interspersed. Thus, we hypothesized that the electrochemical signal of the flakes was overwhelmed by background current, because of the low flake surface area to Pt area ratio. To test this hypothesis, we developed a modified mechanical exfoliation protocol (See above) that produced enhanced surface coverage (Figure 2-14b) and increased the signal observed in CV (Figure 2-15).

Using the alternate exfoliation technique, we performed CV and identified ~4 distinct peaks on the anodic scan (Figure 2-15), which correspond to (de)intercalation events, based on Raman data (Figure 2-16, Figure 2-17). In addition, there are discrete, reproducible color changes in optical microscopy (Figure 2-18), as the flakes transition from tan (pristine HOPG), to dark brown (stage 4, stage 3), to red (stage 2) to yellow (stage 1). With cycling, the voltammograms show peaks appearing at similar voltages every cycle and the flakes pass through the same color sequence. Interestingly, the voltammograms indicate that the intercalation process is not completely reversible, since the deintercalation peaks are separated

by more than 59 mV from the intercalation peaks (Figure 2-18). Based on this observation, it was possible that the flakes were not deintercalating completely from cycle to cycle, which would explain the smaller deintercalation peaks and slightly lower intercalation peaks over time. The optical microscopy images appeared to corroborate this idea, since after the first cycle, the color does not return to that of pristine graphite (Figure 2-19e,f). One reason for this observation could be that we allowed the voltage to ramp to 1.0 V vs. Pt, which is 0.2 V beyond that of the highest peak (~0.7 V vs. Pt) for stage 1. Thus, the flakes could become overoxidized and would require a lower voltage to completely deintercalate. Even when we performed intercalation from 0 – 0.8 V during chronoamperometry, a more negative potential was still required to deintercalate the flakes (Figure 2-18e,f), which indicates that there may be other factors at play, such as structural changes induced during intercalation or deintercalation that trap bisulfate ions.

Interestingly, although the D-peak was absent from the Raman spectra during intercalation, it became prominent for some of the flakes at ~1330 cm^{-1} during deintercalation. However, we also observed spectra for flakes in which the D-peak was absent during deintercalation. This distinction suggests that the deintercalation process can produce disorder in individual flakes.

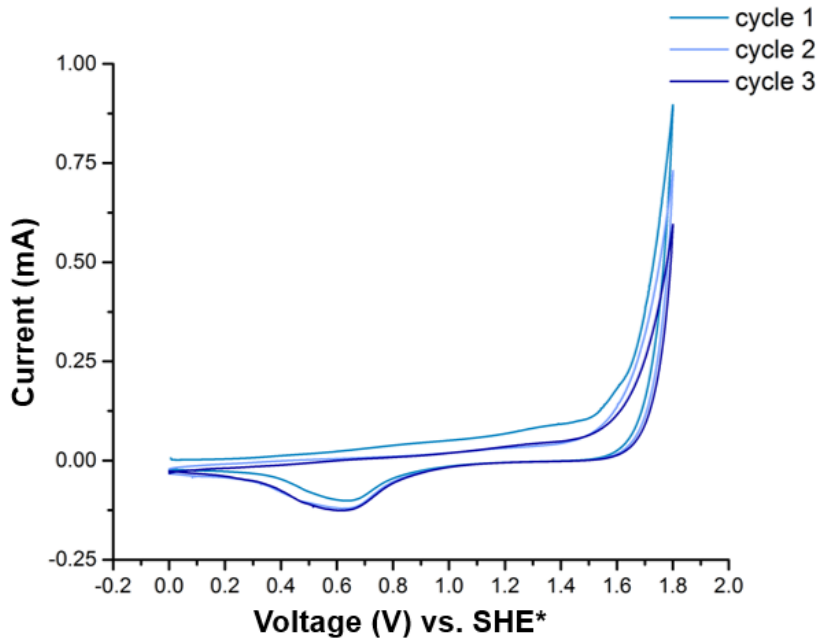


Figure 2-12: Cyclic voltammetry of graphite flakes. The potential was ramped from 0.0 V to 1.8 V with a scan rate of 10 mV/s for 3 cycles. There were no distinct redox peaks to indicate intercalation during the scan**.**

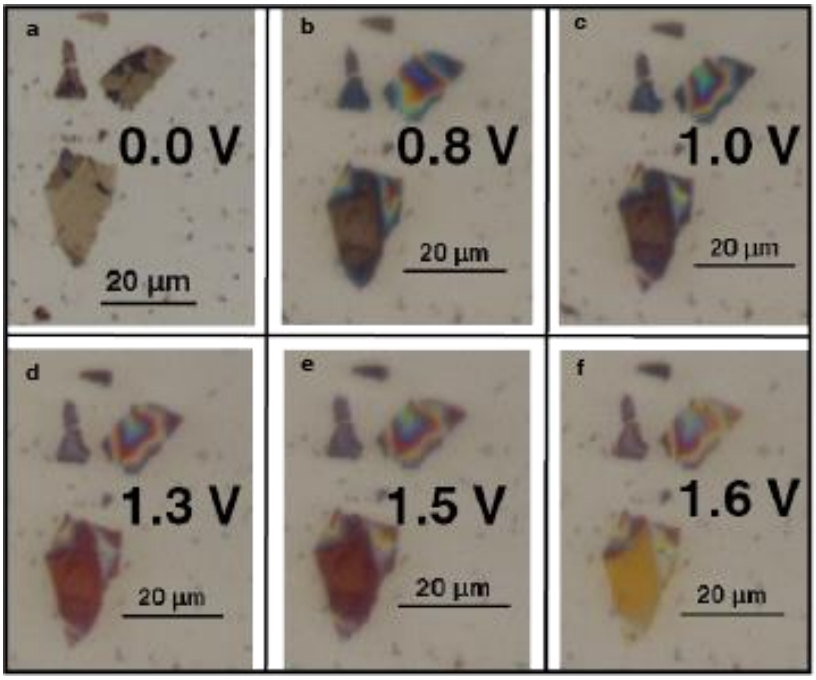


Figure 2-13: Optical images of graphite flakes acquired during cyclic voltammetry. The potential was ramped from 0.0 V to 1.8 V with a scan rate of 10 mV/s for 3 cycles. Images were acquired under an optical microscope in reflectance mode. a) at 0.0 V, b) 0.8 V, c) 1.0 V, d)-e) from 1.3 V – 1.5 V, f) At 1.6 V.

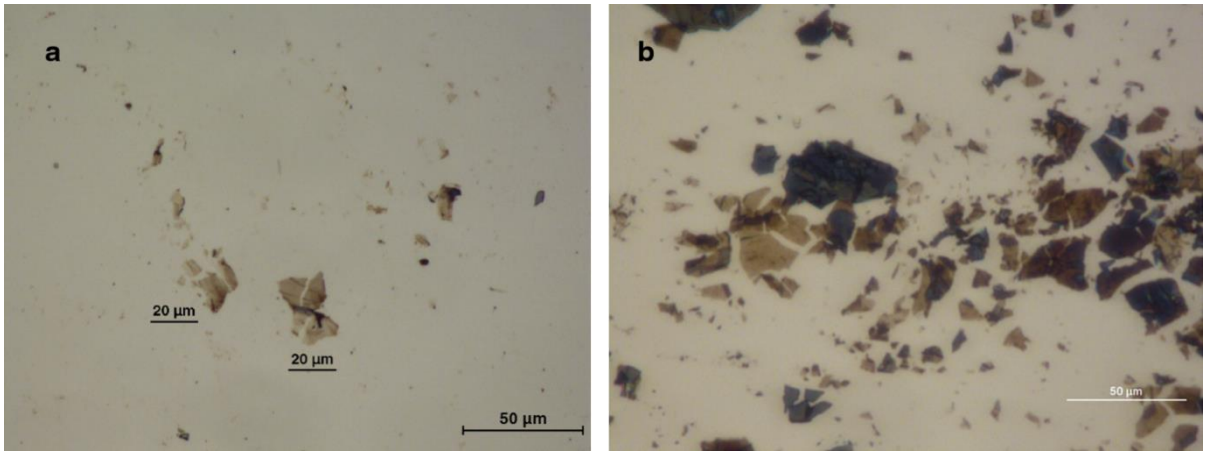


Figure 2-14: Optical microscopy images of mechanically-exfoliated HOPG flakes on a platinum substrate using a) the original exfoliation method and b) the new exfoliation method.

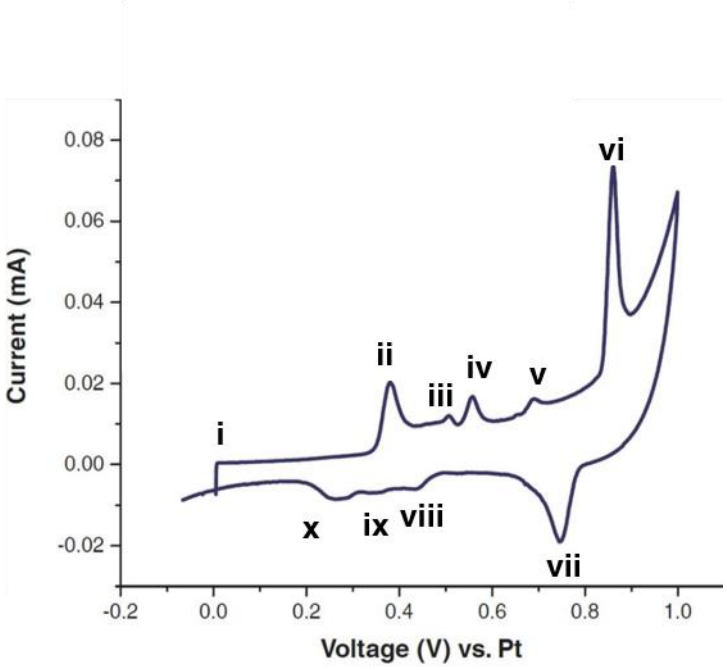


Figure 2-15: CV of the ultrathin flakes using the modified exfoliation method with i) before, ii)-vi) intercalation peaks on the anodic scan and vii)-x) deintercalation peaks on the cathodic scan.

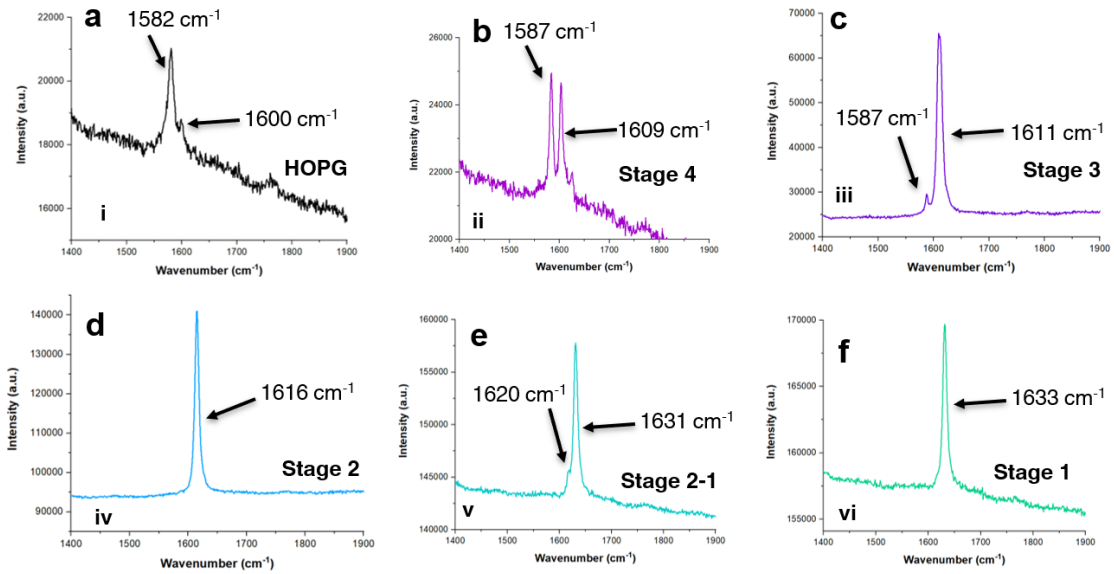


Figure 2-16: Raman spectroscopy of an ultrathin graphite flake during intercalation. The labels i-v represent the point on the CV where the Raman spectra was acquired (from Figure 5-5a). The stage numbers were estimated from Figure 5-9.

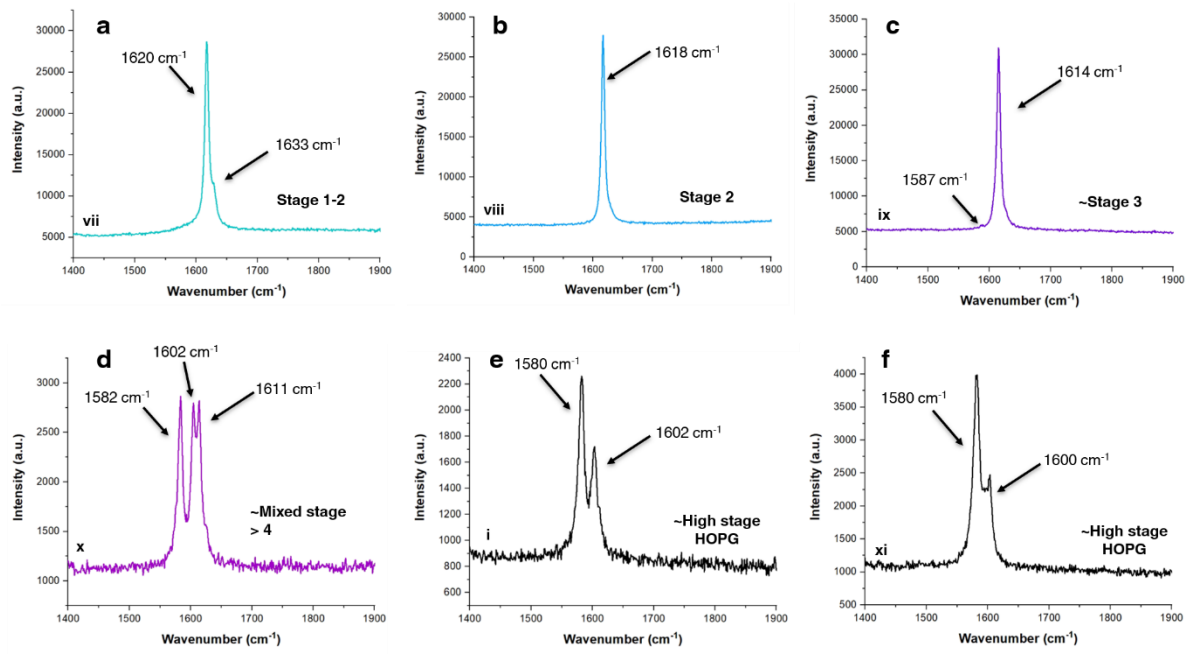


Figure 2-17: Raman spectroscopy of an ultrathin graphite flake during deintercalation. The labels vii-xi represent the point on the CV where the Raman spectra were acquired (from Figure 5-5a). The stage numbers were estimated from Figure 5-9.

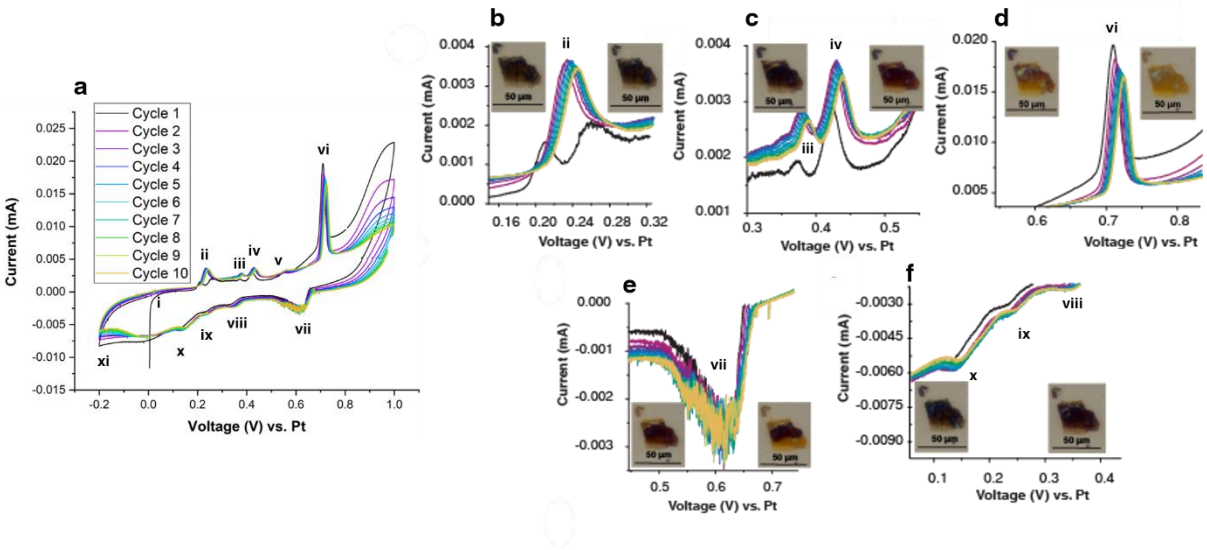


Figure 2-18: CV of the graphite flakes for 10 cycles. a) CV showing the electrochemical response of the graphite flakes over time at 10 mV/s for 10 cycles. In a), the labels delineate graphite i) before intercalation, ii)-vi) during intercalation, and vii)-xi) during deintercalation. b)-d) show the optical microscopy images of a representative flake that correspond to the peaks in a). e) and f) show the optical microscopy images that correspond to the deintercalation peaks in a).

REFERENCES

[1] G. Aronson, S, Frishberg, C, Frankl, *Carbon N. Y.* **1971**, *9*, 715.

[2] A. Metrot, J. E. Fischer, *Synth. Met.* **1981**, *3*, 201.

[3] J. O. Besenhard, H. P. Fritz, *ZAAC - J. Inorg. Gen. Chem.* **1975**, *416*, 106.

[4] J. O. Besenhard, H. Mohwald, J. J. Nickl, *Synth. Met.* **1981**, *3*, 187.

[5] A. Metrot, M. Tihli, *Synth. Met.* **1985**, *12*, 517.

[6] R. Muñoz, C. Gómez-Aleixandre, *Chem. Vap. Depos.* **2013**, *19*, 297.

[7] C. Mattevi, H. Kim, M. Chhowalla, *J. Mater. Chem.* **2011**, *21*, 3324.

[8] K. S. Kim, Y. Zhao, H. Jang, S. Y. Lee, J. M. Kim, K. S. Kim, J. H. Ahn, P. Kim, J. Y. Choi, B. H. Hong, *Nature* **2009**, *457*, 706.

[9] Y. Zhang, L. Zhang, C. Zhou, *Acc. Chem. Res.* **2013**, *46*, 2329.

[10] M. Losurdo, M. M. Giangregorio, P. Capezzuto, G. Bruno, *Phys. Chem. Chem. Phys.* **2011**, *13*, 20836.

[11] M. Pourbaix, *Natl. Assoc. Corros.* **1974**.

[12] Lopez, Gerald G., M. Azadi, *Protoc. Reports* **2016**, 1.

[13] C. L. Haynes, R. P. Van Duyne, *J. Phys. Chem. B* **2001**, *105*, 5599.

[14] M. Wang, L. Fu, L. Gan, C. Zhang, M. Ru, A. Bachmatiuk, K. Huang, *Sci. Rep.* **2013**, *3*, 1.

[15] A. Chandramohan, N. V Sibirev, V. G. Dubrovskii, M. C. Petty, A. J. Gallant, D. A. Zeze, *Sci. Rep.* **2017**, *7*, 1.

[16] K. S. Novoselov, A. K. Geim, S. V. Morozov, D. Jiang, Y. Zhang, S. V. Dubonos, I. V. Grigorieva, A. A. Firsov, *Science (80-.).* **2004**, *306*, 666.

[17] D. C. Alsmeyer, R. L. Mccreery, *Anal. Chem.* **1992**, *64*, 1528.

CHAPTER 3 – ELECTROLYTE-FREE SPECTROSCOPY AND IMAGING OF INTERCALATION IN GRAPHITE ELECTRODES[1]

*Madeline S. Stark[§], Judy Cheng[§#], Hailey Kim[§#], Kaci L. Kuntz[§#], and Scott C. Warren[§±]**

[§]Department of Chemistry, and Department of Applied Physical Sciences, [±]University of North Carolina at Chapel Hill, Chapel Hill NC, 27599. USA.

[#]These authors contributed equally.

3.1 Introduction

Understanding electrode-electrolyte interactions in layered electrodes provides a powerful motivation to obtain time- and spatially-resolved information in-situ. However, it is challenging[2] to combine high spatial resolution with in-situ capabilities to probe structural changes[3], electronic properties[4], or the evolution of a solid-electrolyte interphase (SEI)[5]. Thus, the mechanisms of intercalation, ion transport, and stage transitions are not well-understood for even the most common electrode materials. For example, although graphite intercalation compounds (GICs) have been heavily studied since the mid-1900s, questions about mechanisms, charge transfer, and the influence of host structure still remain.[6,7]

Optical techniques, in particular, can complement traditional electrochemical methods to understand intercalation in GICs. Many GICs exhibit colorful stages and stage transitions, providing a platform to elucidate the mechanisms of staging and ion transport optically.[8–10] Recently, Dimiev et al. described the stage transitions in the graphite-H_2SO_4/$(NH_4)_2S_2O_8$ system during chemical intercalation and deintercalation.[11] Importantly, they identified the

colorful regions during the stage 2-1 transition as intercalant islands coalescing at localized regions within HOPG, consistent with the Daumas-Herold model of staging.[12] In addition, they observed preferential deintercalation of certain domains due to strain[11], which could be relevant to electrochemical systems. These results prompt additional questions about the composition, tunability, and optical properties of these intercalant domains in GICs, as well as their application in an electrochemical context.

Spectroscopic tools, such as UV-vis or infrared spectroscopy, could also offer complementary insight into a GIC's optical properties or composition in-situ. However, it is challenging to combine high spatial resolution with in-situ capabilities to probe electrode materials since these techniques often suffer from scattering due to organic, aqueous, or solid-electrolytes. Previously, researchers have explored a variety of methods to minimize electrolyte interference for in-situ measurements of intercalation compounds. For example, in layered materials, the material can be suspended above the electrolyte, being either partially immersed[13] or floating on the surface of the electrolyte[14] Then, during intercalation, the material can be probed spectroscopically above the line of electrolyte. However, these geometries are often fragile and difficult to implement. In contrast, planar devices offer a more attractive platform for probing materials[4,15] in-situ, since the cells are completely sealed, enable in-situ electrical measurements, and can be transferred between instruments. One disadvantage of a planar device is that the electrolyte would normally cover the surface of the material, resulting in lower intensities and reduced signal.

To address the challenges of both electrolyte interference and device design, we fabricated a planar device in which we probe an area of the electrode that is laterally separated from the electrolyte. This electrolyte-free geometry enables us to probe visible absorption

characteristics and changes in chemical functionality. We also monitor ion transport dynamics without electrolyte interference using optical microscopy. In the visible, we observe plasma frequency shifts that occur due to charge transfer. In addition, we examine vibrational signatures in the mid-IR, a region previously difficult to access due to electrolyte absorption. Finally, we compare the properties of this electrolyte-free device with a traditional geometry in which electrolyte covers the entire surface of the electrode.

As a model for electrolyte-free intercalation, we selected the bisulfate-graphite compound for both its electrochemical and optical behavior. In terms of electrochemistry, the system exhibits well-defined staging[16–18] and reversible cycling[19], paralleling battery technologies but in an aqueous environment[16,20]. Moreover, the plasma frequency of graphite is highly sensitive to charge transfer[6,7,9] offering tunable optoelectronic properties.[4,7] This system also provides a platform to highlight the advantage of the electrolyte-free device in the IR. Since the vibrational features of the bisulfate species occur in the mid-IR[21] but are overwhelmed by absorption from the electrolyte, the electrolyte-free geometry enables us study the absorption of the intercalated bisulfate species in the mid-IR.

3.2 Methods

3.2.1 Device Design

Figures 3-1 and 3-2 show the general steps for fabricating the electrolyte- and electrolyte-free devices. In the first step, we cut SPV-224PR-MJ surface protection tape (Nitto) into strips, and placed them on a standard glass slide (75 mm x 25 mm x 1 mm, VWR) to form a mask. Then, using a K.J. Lesker PVD Sputter system, we sputtered 10 nm of titanium

followed by 100 nm of platinum onto the glass slide. The titanium served to better adhere the platinum to the surface. After sputtering, we removed the tape (Figure 3-2a), rinsed the surface with isopropyl alcohol (VWR), and dried it with N_2. To prepare the highly oriented pyrolytic graphite (HOPG), we cleaved thin strips (100 μm) using tweezers and a razor blade to peel segments off of the bulk crystal. Then, we adhered the HOPG to the Pt with conductive carbon tape to form the working electrode (Figure 3-1a and 3-2b). To fabricate the electrochemical cell (Figure 3-1 and 3-2), we first ensured that the device components would be stable toward oxidation and highly acidic conditions. Thus, we selected platinum as the conductive substrate since it is known to be stable over the voltage window and the H_2SO_4 concentration range at which intercalation occurs.[22]

To form the electrolyte well, we sandblasted three sets of coverslips (24 mm x 40 mm x 0.17 mm, Thermo Fisher Scientific) (Figure 3-1a-c). The first set of two coverslips had the centers cut out with a rim of ~5 mm and a small notch at the end adjacent to the graphite (Figure 3-1a and 3-2c). The second set of five coverslips had the centers cut out with a rim of ~ 5 mm (Figure 3-1b). The final coverslip had a hole cut approximately 10 mm from the edge of the slide (Figure 3-1c). These components were adhered over the surface of the microscope slide using epoxy (Hysol 9340, Loctite) and cured at 80 ^{o}C for 2 hours. After creating the electrolyte well, we applied electrical contacts on the working, counter, and reference electrodes using copper tape, and covered the contacts with electrical tape (Figure 3-2d). To fabricate the electrolyte-free side, (Figure 3-2e), we created another well in a N_2 glovebox. The electrolyte-free well consisted of seven coverslips cut as depicted in Figure 3-1d. Another coverslip (Figure 3-1e) was placed on top of these coverslips and these components were adhered over the surface of the microscope slide using epoxy (Figure 3-1f, 2-2e). We found that in an oxygen

environment, the graphite reached stage 2 and then began to over-oxidize and degrade. In an oxygen-free environment, however, the material readily transformed from stage 2-1 in the electrolyte-free region. Thus, we sealed the electrolyte-free region in the glovebox before bringing the device out for intercalation.

To fill the electrolyte well, we prepared a solution of 15 M H_2SO_4, and pipetted ~ 2 mL into the hole on the electrolyte side. We then sealed the hole with a square glass coverslip (24 mm x 24 mm, Thermo Fisher Scientific) and epoxy (Hysol 9340, Loctite). It is important to note that this device can easily be adapted to other electrolytes by changing the identity of the counter and reference electrodes and host material. We have tested the stability of the epoxy in aqueous solutions, with sulfuric acid, ammonium sulfate, and iron (III) chloride. We have also observed that the epoxy is compatible with organic solvents (e.g. propylene carbonate and ethylene carbonate), which is relevant for extending our work to other electrolyte systems, including alkali metal ions. As long as the reference and counter electrodes are compatible, the device should be broadly applicable for intercalation in a variety of electrolyte solutions.

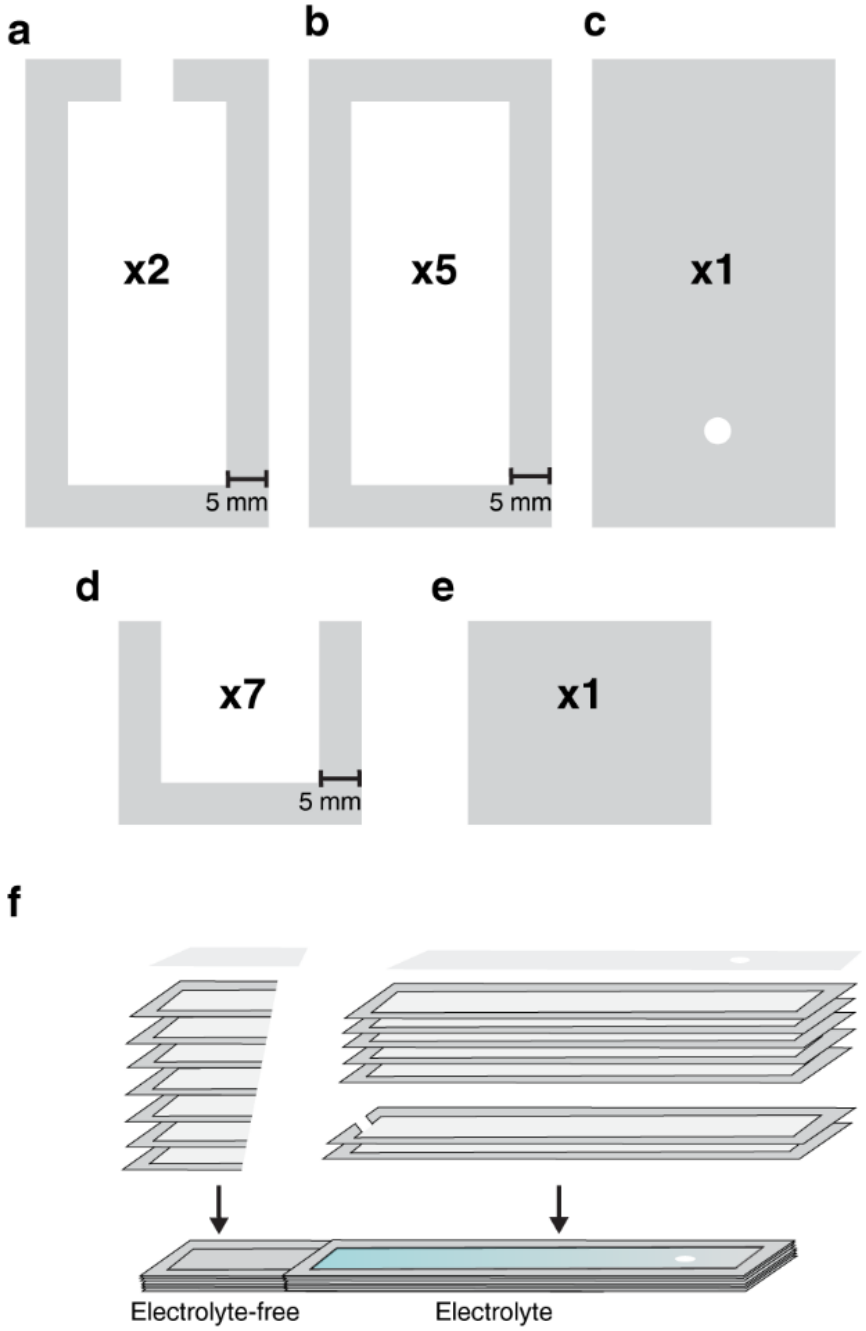


Figure 3-1: Fabricating the electrolyte-free device. The electrolyte-well consists of (a) two notched coverslips with the centers cut out followed by (b) five coverslips with the centers cut out. Another coverslip (c) with a hole was placed over the sets in (a) and (b). The electrolyte-well consisted of seven coverslips cut as shown in (d). The cover glass depicted in (e) was sealed over the top of the electrolyte-free region. (f) shows the order of the coverslips as they were adhered over the electrodes to form the electrolyte and electrolyte-free wells.

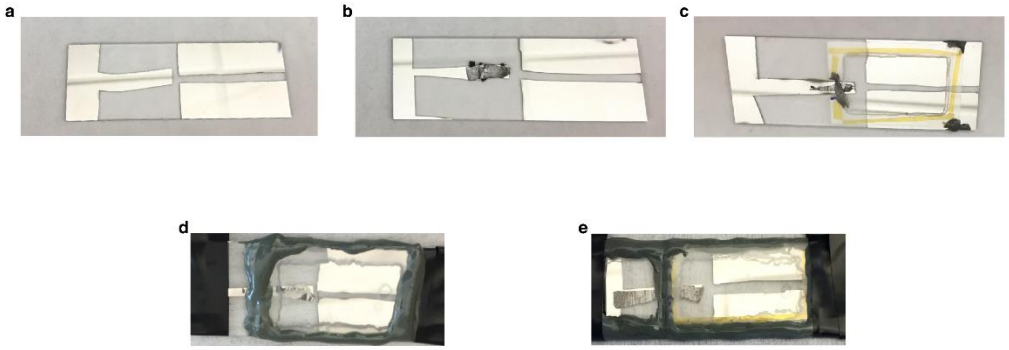


Figure 3-2: Fabricating the electrolyte and electrolyte-free devices. (a) Pt is patterned onto a glass slide to form working, reference, and counter electrodes. (b) HOPG adhered to the surface of Pt forms the working electrode. (c) Sandblasted coverslips form the electrolyte-well. All components in the (d) electrolyte and (e) electrolyte-free devices are sealed with epoxy.

A note on the applicability of this device for other in-situ experiments (Table 2-1): As we state in the manuscript, this device is widely applicable to microscopy and spectroscopic techniques. It could also be used for X-ray diffraction, as long as the window on the electrolyte-free side is adapted to be X-ray transparent (e.g. Kapton). We do not recommend the device as it stands for TEM techniques since the components are not electron transparent and we believe that there are other more suitable in-situ designs for TEM. For techniques involving measurements under vacuum, the device will need to be tested in a vacuum environment to ensure that it is capable of withstanding the vacuum levels required for characterization. We are currently working toward studying how the cell and epoxy respond under vacuum, but we anticipate that there will need to be minor adaptations to the cell for these types of experiments.

Table 3-1: Outlining the techniques where the electrolyte-free device could be applicable.

Technique	This work	Will this device work?	Additional considerations/modifications
Optical Microscopy	Yes	Yes	None
Raman spectroscopy	Yes	Yes	None
UV-vis spectroscopy	Yes	Yes	None
FT-IR spectroscopy	Yes	Yes	IR transparent window (e.g. CaF_2)
X-ray diffraction	No	Yes	X-ray transparent window (e.g. Kapton)
SEM	No	Yes, with adaptations	No window over the electrolyte-free region. *It would also be necessary to ensure the epoxy and glass components are viable at the required vacuum levels. Other potential adaptations include using a vacuum compatible epoxy and thicker glass over the electrolyte.
TEM	No	No	*Other device designs would most likely be better suited for this technique. Creative modifications could be possible, but we can't recommend them at this time.
XPS/UPS	No	Yes, with adaptations	No window over the electrolyte free region. *It would also be necessary to ensure the epoxy and glass components are viable at the required vacuum levels. Other potential adaptations include using a vacuum compatible epoxy and thicker glass over the electrolyte.

3.2.2 Electrochemistry

Figures 3-3 and 3-4 show the voltage vs. time curves for a traditional planar electrochemical cell and our new device geometry, containing a barrier to laterally separate part of the material from the electrolyte. In both devices, the resulting voltage vs. time curves exhibit a series of steps and plateaus corresponding to staging events. For example, during the stage 3-2 plateau (Figure 3-3), the voltage remains relatively constant as the stage 3 compound converts to stage 2. At the end of the plateau, the material has been converted to stage 2, and the voltage begins to increase to the potential of the next stage. Once the voltage reaches the potential for stage 1, the stage 2-1 transition takes place. It is important to note the main difference that occurs between the chronopotentiogram of the traditional electrochemical cell and the electrolyte-free device geometry. Specifically, the number of plateaus observed in the electrolyte-free geometry (Figure 3-4) was greater than in the electrolyte cell (Figure 3-3). We attributed this difference to the two different environments of the electrolyte-free device. The device consisted of HOPG in an electrolyte region and in an electrolyte-free region. Based on our observations under the optical microscope, the electrolyte side intercalated completely to stage 1 before the ions began to pass under the barrier to the electrolyte-free side. In Figure 3-4, the plateau that appeared between 0.6 and 0.8 V vs. Pt corresponded to the stage 2-1 transition in the electrolyte region. Near 42000 s on the graph, there is an inflection point. This point indicates that the voltage is sufficient for the material under the barrier to undergo the stage 2-1 transition. After the graphite under the barrier transitions from stage 2-1, the electrolyte-free region begins to undergo the stage 2-1 transition around 60000 s.

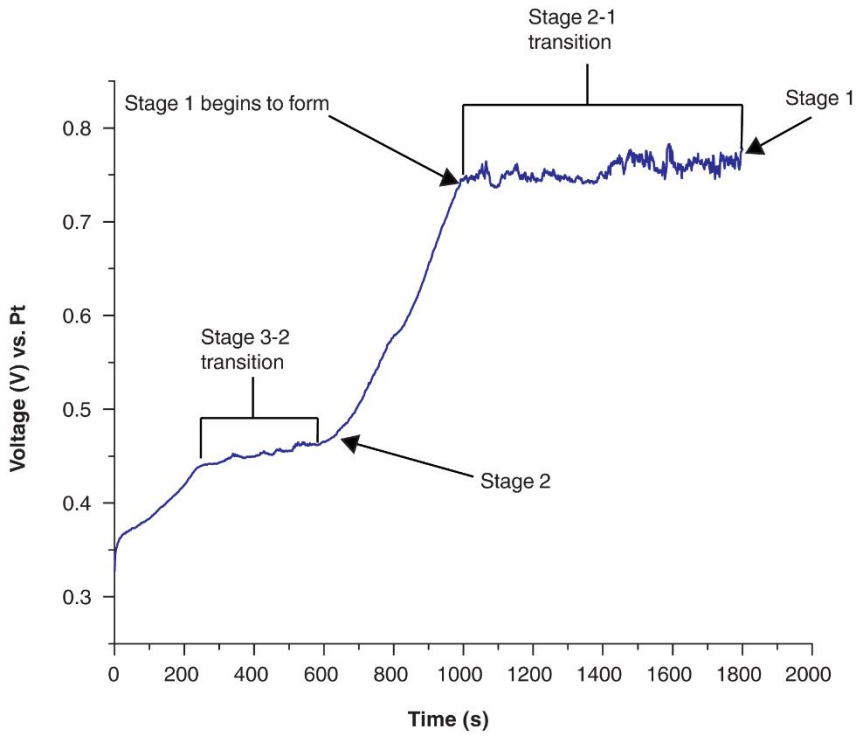


Figure 3-3: Chronopotentiogram showing the stage transitions in the electrolyte device. When a constant current is applied, the voltage begins to increase until it reaches a plateau. The first plateau is the stage 3-2 transition occurring near 0.45 V vs. Pt. Once all of the material has been converted to stage 2, the voltage once again increases until it reaches the potential for the formation of stage 1. Another plateau occurs for the stage 2-1 transition. At the end of the plateau, pure stage 1 forms.

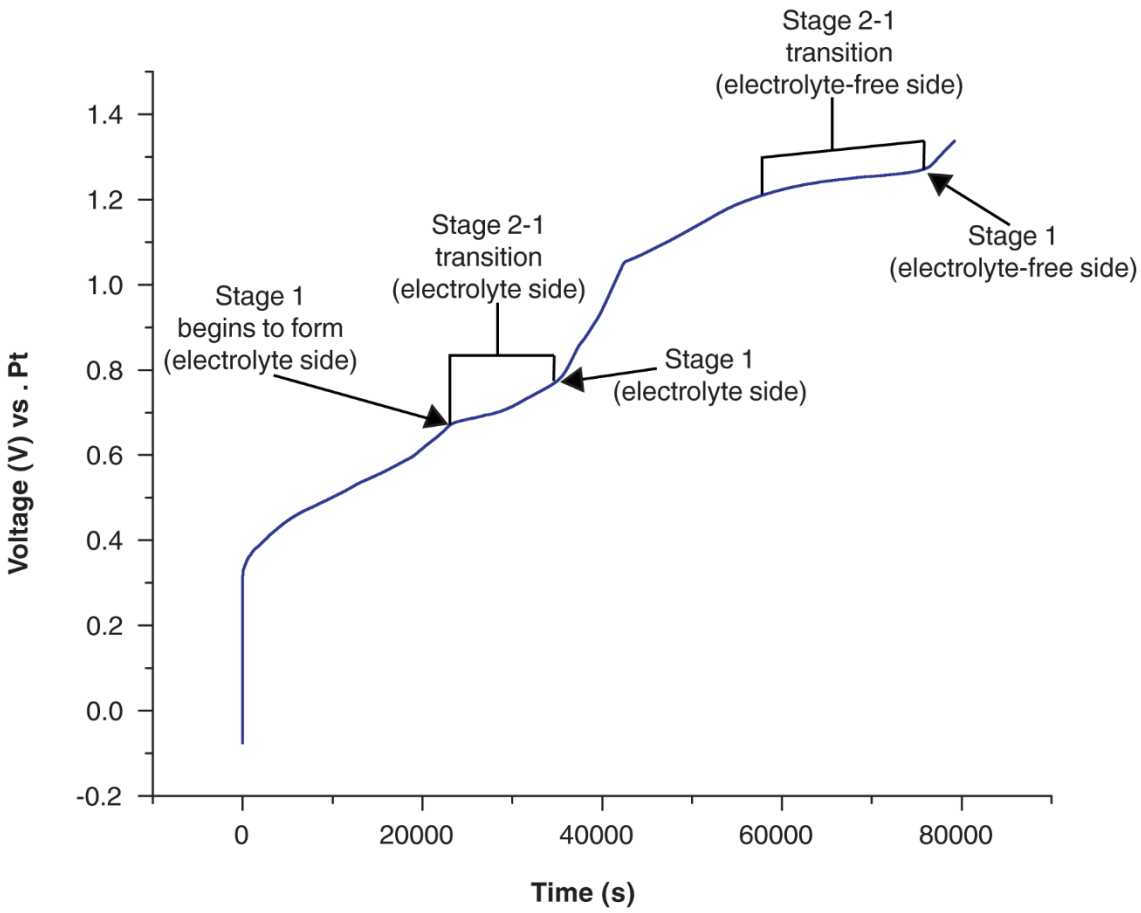


Figure 3-4: Chronopotentiogram showing the stage transitions in the electrolyte-free device. When a constant current is applied, the voltage begins to increase until it reaches the potential for the stage 1 compound in the electrolyte region (0.65 V – 0.80 V). After this plateau, all of the electrolyte region has been converted to stage 1. The potential increases again, as the electrolyte-free region begins to undergo the stage 2-1 transition (1.0 V – 1.3 V). At the end of this plateau, pure stage 1 is present.

Importantly, however, not all of the staging events were resolved in our chronopotentiograms due to the relatively high currents (0.07 mA) that we use in order to limit the time-scale of the experiments. At lower currents (e.g. 0.001 mA), more stage transitions can be observed, based on previous reports[16]. However, intercalation to stage 1 under these conditions has been reported to take up to a week, while our experiments were accomplished

in a period of hours, similar to the work of Aronson et al.[19] For the electrolyte device, the graphite is surrounded by electrolyte on all sides and intercalation occurs more rapidly (in a period of ~ 30 minutes – 2 hours, depending on the size/thickness of the graphite). However, for the electrolyte-free device, the addition of a barrier increases the time required for intercalation to stage 1 (~5-24 hours). Based on our experiments, complete intercalation from the electrolyte region to the electrolyte-free region occurs regardless of the size ratio between the electrolyte and electrolyte-free regions. However, intercalation occurs more rapidly when the electrolyte-free region is small, since the kinetics were slower in the electrolyte-free region.

3.2.3 Optical Microscopy

Optical images and videos were acquired *in-situ* using a Nikon Eclipse E600 microscope, equipped with a Nikon T Plan 50X SLWD objective with an N.A. of 0.40. Videos were recorded at 1 fps, with an MJPEG compression to reduce the file size.

3.2.4 Raman Spectroscopy

Raman spectra of the bisulfate-graphite intercalation compounds were obtained *in-situ* using a Renishaw Raman instrument, a 633 nm laser line, and a Nikon T Plan 50X SLWD objective with an N.A. of 0.40. Extended scans were recorded from 3200 cm^{-1} to 100cm^{-1}, using 100% laser power and 10s exposure time. Since the stage 2-1 transition occurs rapidly, we performed static scans centered at 1580 cm^{-1} during that regime. Figure 3-5a,b show the absence of a D peak at ~1330 cm^{-1} for both the electrolyte and electrolyte-free devices respectively.

To demonstrate the advantage of the electrolyte-free device over a traditional geometry, we quantified the intensities of the Raman shifts for the HOPG, stage 2, and stage 1 graphite. It is important to note that the sampling depth for HOPG is ~ 130 Å[23], but since graphite intercalation compounds have a lower density of graphite, the sampling depth is greater (~1000 Å) after intercalation[17]. In the electrolyte, we observed a ~27-fold increase in scattering intensity going from graphite to stage 1, which agrees with previous work[20]. Interestingly, in the electrolyte-free region, the increase in scattering intensity was ~40-fold or 1.5 times the increase we observed in the electrolyte region for stage 1. Moreover, the relative peak intensity for the electrolyte-free region was greater than that of the electrolyte region by a factor of ~2 for stage 2 and ~1.5 for stage 1. This difference suggests that spectroscopically probing an area laterally separated from the electrolyte results in enhanced signal.

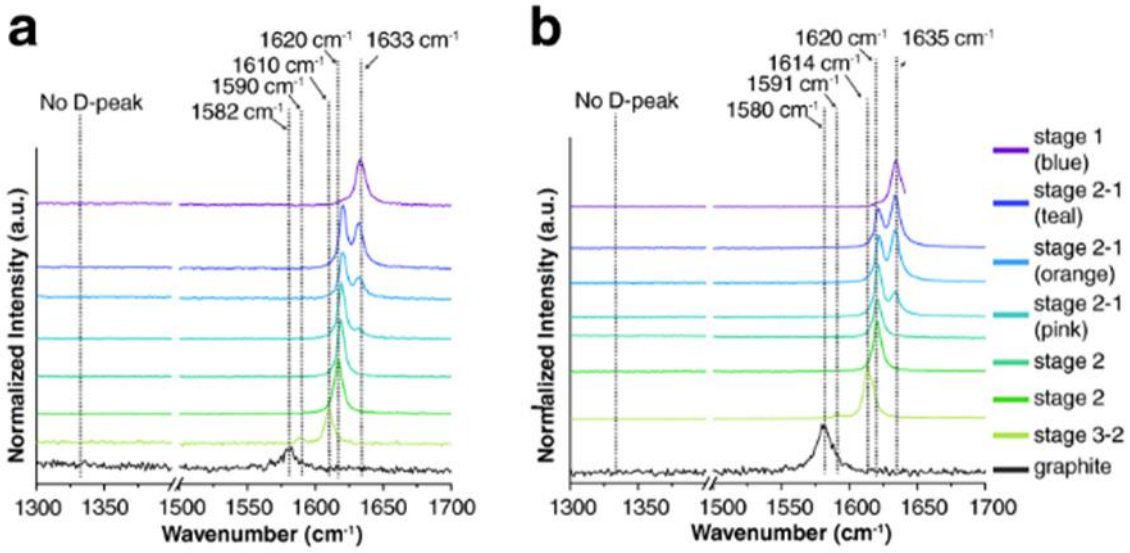


Figure 3-5: Raman spectra of (a) electrolyte and (b) electrolyte-free regions.

3.2.5 UV-vis Spectroscopy

The reflectance spectra of the bisulfate-graphite intercalation compounds were obtained *in-situ* from 350 nm – 800 nm, using a Craic UV-vis-NIR microspectrophotometer with a polychromatic Xe source and an EC Epiplan Neofluar LD objective with an N.A. of 0.55. The aperture size was 14.7 x 14.7 μm for the electrolyte-free spectra and 9.6 x 9.6 μm for electrolyte region. The time needed to acquire an individual spectrum using this instrument can range from 30 seconds up to several minutes. Since the stage 2-1 transition tends to occur more rapidly through the regions, the time resolution of our instrument was not sufficient to capture the range of colors passing through a single region. Thus, we took multiple spectra from a variety of points during the stage 2-1 transition and show representative images and spectra in Figure 3-8 of the text. Since the conditions in the cell changed throughout the experiment, the background spectrum was first obtained on the platinum substrate, before intercalation, in both the electrolyte and electrolyte free regions.

3.2.6 FT-IR Spectroscopy

Infrared reflectance spectra were acquired *in-situ* using a Bruker Optics Hyperion 1000 with Tensor 27, equipped with an MCT detector and a 36X objective with a pixel resolution of 1.1 μm. Since the glass coverslips absorb in the mid-infrared, we used a 10 mm x 0.13 mm CaF_2 window, which has above 90% transmission from 0.13 μm to 10 μm (Crystran). Since the conditions in the cell changed throughout the experiment, the background spectrum was first obtained on the platinum substrate, before intercalation, in the electrolyte-free region.

3.3 Device Design

The electrolyte-free device features a region of the electrode that is laterally-separated from the electrolyte. Thus, we created a planar device with an electrolyte and electrolyte-free compartment (**Figure 3-6a,b**, **Figure 3-1**, and **Figure 3-2**). To fabricate this device, we sputtered Pt onto discrete regions of a glass slide to create the conductive substrate for the highly-oriented pyrolytic graphite (HOPG), as well as the counter and pseudoreference electrodes (Figure 3-2a). We adhered a strip of HOPG (~10 mm x 5 mm x 100 μm) onto the Pt substrate to form the working electrode (Figure 3-2b). To form the barrier, a thin polymer strip was placed across the surface of the HOPG. A thin layer of chemically resistant epoxy covered the polymer barrier to increase its resistance to electrolyte propagation (Figure 3-2c). We mounted two glass windows over the electrodes with the chemically-resistant epoxy (Figure 3-2d,e). In the electrolyte device, the electrolyte is injected and contacts the counter and pseudoreference electrodes and the entire surface of the HOPG. In the electrolyte-free device, however, we added a barrier (Figure 3-6a,b and Figure 3-2c,e) that allows the electrolyte to contact the counter, pseudoreference electrodes, and only part of the HOPG surface (Figure 3-6a,b). This design feature is critical, since it allows ions to insert into the graphite on the electrolyte side and spread through the electrode without covering the surface.

3.4 Optical Microscopy

We hypothesized that this design would cause the ions to pass through the graphite laterally, from the electrolyte side to the electrolyte-free side. To strengthen this hypothesis, we monitored intercalation *in-situ* using optical microscopy in the electrolyte (**Figure 3-6**c-h) and electrolyte-free devices (Figure 3-6i-n). The images shown in Figure 3-6 were taken in the

same locations in each region during intercalation. Initially, the graphite appeared grey before intercalation (Figure 3-6c,i). As current flowed during chronopotentiometry, the voltage became more positive, (**Figure 3-3** and **3-4**), causing negatively-charged bisulfate ions to

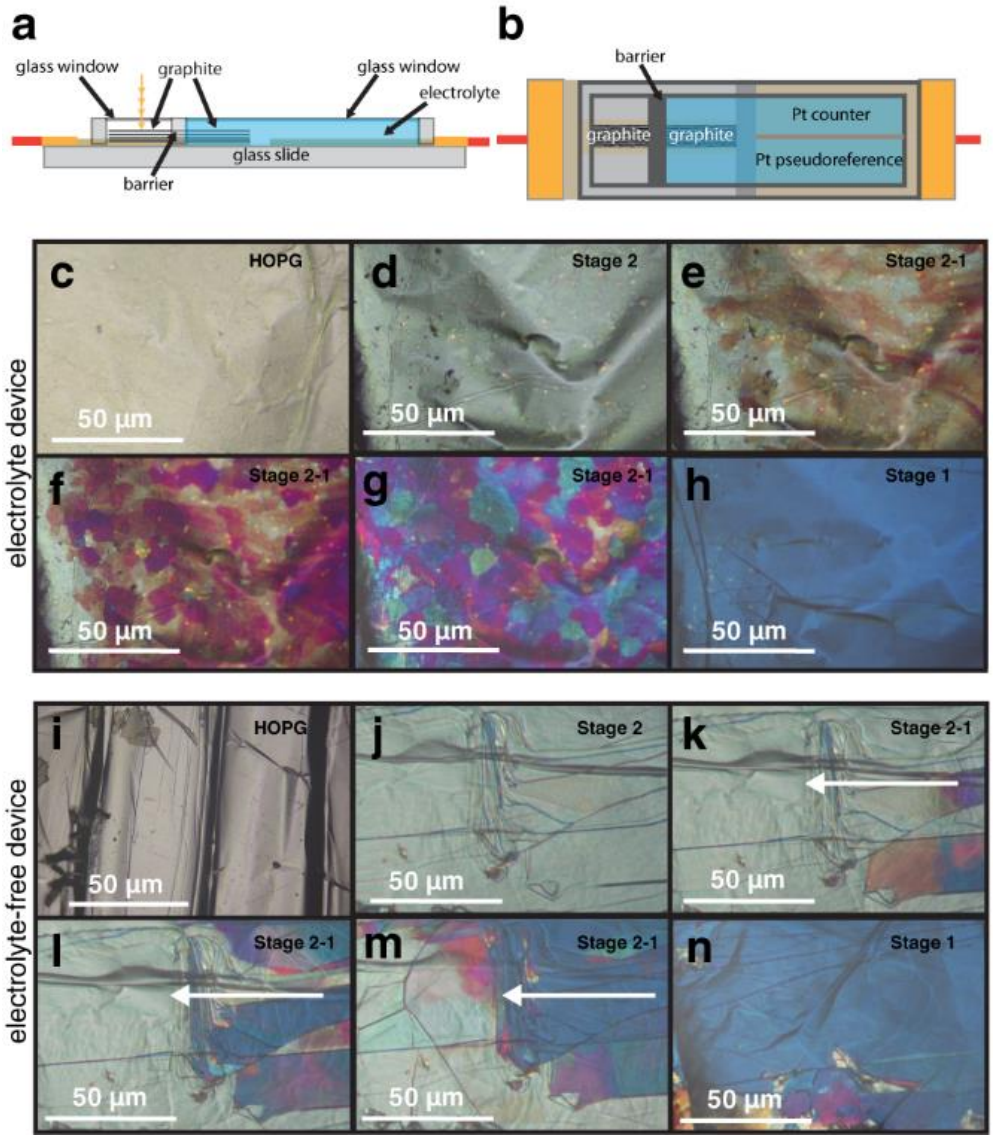


Figure 3-6. Device schematic and in-situ optical microscopy images in electrolyte and electrolyte-free environments. Side (a) and top-down (b) views of the device. The HOPG working electrode spans the electrolyte and electrolyte-free regions, with a barrier separating

the two environments. (c)-(h) show the optical images of graphite immersed in electrolyte (c) before intercalation, (d) at stage 2, (e)-(g) during the stage 2-1 transition, and (h) at stage 1. (i)-(n) show the optical images of graphite (i) before intercalation, (j) stage 2, (k)-(m) during the stage 2-1 transition, and (n) at stage 1. Arrows show the direction of ion transport during the transition region. For (c)-(h), images were acquired over a period of 15 minutes and for (i-n), images were acquired over a period of 2 hours.

intercalate into the graphite. As ions inserted between the layers, the material transitioned through a series of stages (Figure 3-3 and 3-4), where a stage is defined as the ratio of host to guest layers. For example, when the degree of intercalation reaches stage 2, there are two layers of graphite for every one layer of intercalant. At stage 2, the material appears grey-blue (Figure 3-6d,j).

Images (Figure 3-6d-f, k-m) and videos (SI video 1, 2) of the stage 2-1 transition clearly demonstrate the key difference between the direction of ion transport in the two devices. In the electrolyte, ion insertion can occur at the flake edges[10] or along grain boundaries in the basal surface[13,20]. At the onset of the stage 2-1 transition, we observed regions of orange (Figure 3-6e), followed by magenta, purple, and blue (Figure 3-f,g) emerging within individual grains. Then, as more ions intercalated, a wave of color, also known as an intercalant front[10], initiated at the graphite's edges and propagated toward the center. The characteristic blue of the stage 1 material followed these fronts until they merged at the center and the material was completely stage 1 (Figure 3-6h).

These intercalation dynamics contrast starkly with the those that occur in the electrolyte-free device (Figure 3-6k-n). In the electrolyte-free region, ions can only propagate from the electrolyte side. In addition, since the surface is also free from electrolyte, intercalation cannot occur through grain boundaries in the basal surface. Thus, the ions propagate laterally through the graphite, as we observed with optical microscopy (Figure 3-6k-n, SI video 2). Figure 3-6k-n shows the progression of the intercalant front through the

graphite from the electrolyte side to the electrolyte-free side.

In addition, our observations of ion transport during the stage 2-1 transition led us to compare our results to a model[24] for Li-diffusion, which predicts that two rates describe Li^+ transport in HOPG: fast intragrain ("horizontal") transport and slow grain boundary ("vertical") transport. Our observations were consistent with this model at the end of the stage 2-1 transition (Figure 3-6g,h, m,n; SI video 1, 2), since an intercalation front moved laterally, but not vertically through the HOPG. However, our observations at the onset of the stage 2-1 transition could not be fully described by this model, with regions of color appearing at distinct locations in the graphite's surface at different rates. Based on these observations, we hypothesized that there is likely a fairly large activation energy for nucleating a new intercalant island within a domain for the bisulfate-graphite system. The Daumas-Herold model[12] coupled with Dimiev et al.'s description[11] of intercalant island formation during chemical intercalation offered additional insight into the colorful domains we observed: the colors that appear are due to intercalant islands coalescing during the stage 2-1 transition. Our results agree with those of Dimiev et al., except that we visually separate the colors into at least 5 distinct hues: orange, magenta, purple, cyan, and blue. We identified the general trend that orange appears first, followed by magenta, purple, cyan and then the final blue of stage 1. Other colors (i.e. yellow and green) do not appear consistently in our videos, and when they do arise, disappear rapidly. We attribute this to an unfavorable alignment of the intercalant islands, which is readily replaced by a more energetically favorable configuration as the ions propagate through the HOPG.

Our observations in the electrolyte-free region appear to offer additional support for the intercalant island hypothesis (SI video 2). Often, we observed that the intercalant islands

moved rapidly until they reached a visible or invisible boundary. Then, some time elapsed before the color propagated into an adjacent region. During this time, the concentration of bisulfate in the region increased until it reached the stage 1 structure. Then, the islands moved into adjacent regions. Sometimes, the rate of ions exiting the filled domain appeared to outpace the rate of ions filling it, since the region reverted to colors characteristic of a stage 2-1 transition region. Based on our observations, we hypothesized that structural effects, such as grain boundaries in the graphite may play a role in determining preferential pathways for bisulfate transport within the HOPG. In the electrolyte region, the bisulfate ions can enter through any edge and propagate through the HOPG layers. However, in the electrolyte-free region, we restrict the number of possible transport pathways. Thus, the bisulfate must travel laterally from the electrolyte-side to the electrolyte-free side. If a structural feature or local potential prevents the ions from traveling through a certain region, the bisulfate concentration builds up in that region until either the graphite layers restructure to accomodate transport across the barrier or an alternate pathway is identified. These observations provide motivation to systematically study the effects of the HOPG structure on bisulfate transport in the future.

3.5 Raman Spectroscopy

To monitor the effects of charge transfer and determine whether intercalation induced defects in the graphite lattice, we performed *in-situ* Raman spectroscopy in both the electrolyte (**Figure 3-7**a) and electrolyte-free (Figure 3-7b) devices. The graphite G-peak is highly sensitive to charge transfer. Before intercalation, the G-peak appeared at 1580 cm^{-1} and there was no D-peak (1330 cm^{-1}) (SI Figure 3-5a,b), as expected for high-quality HOPG. As

intercalation progressed, a doublet emerged, characteristic of stages n>2.[20] The lower frequency component (G_1) arises from interior graphite layers that are not adjacent to an intercalant layer.[6,7,20] The layers directly adjacent to intercalant layers (G_2) experience greater charge transfer, and effectively screen the interior layers. [6,7,20] Thus, G_2 was shifted to higher frequencies. When intercalation reached stage 2, the doublet resolved into a single peak, since

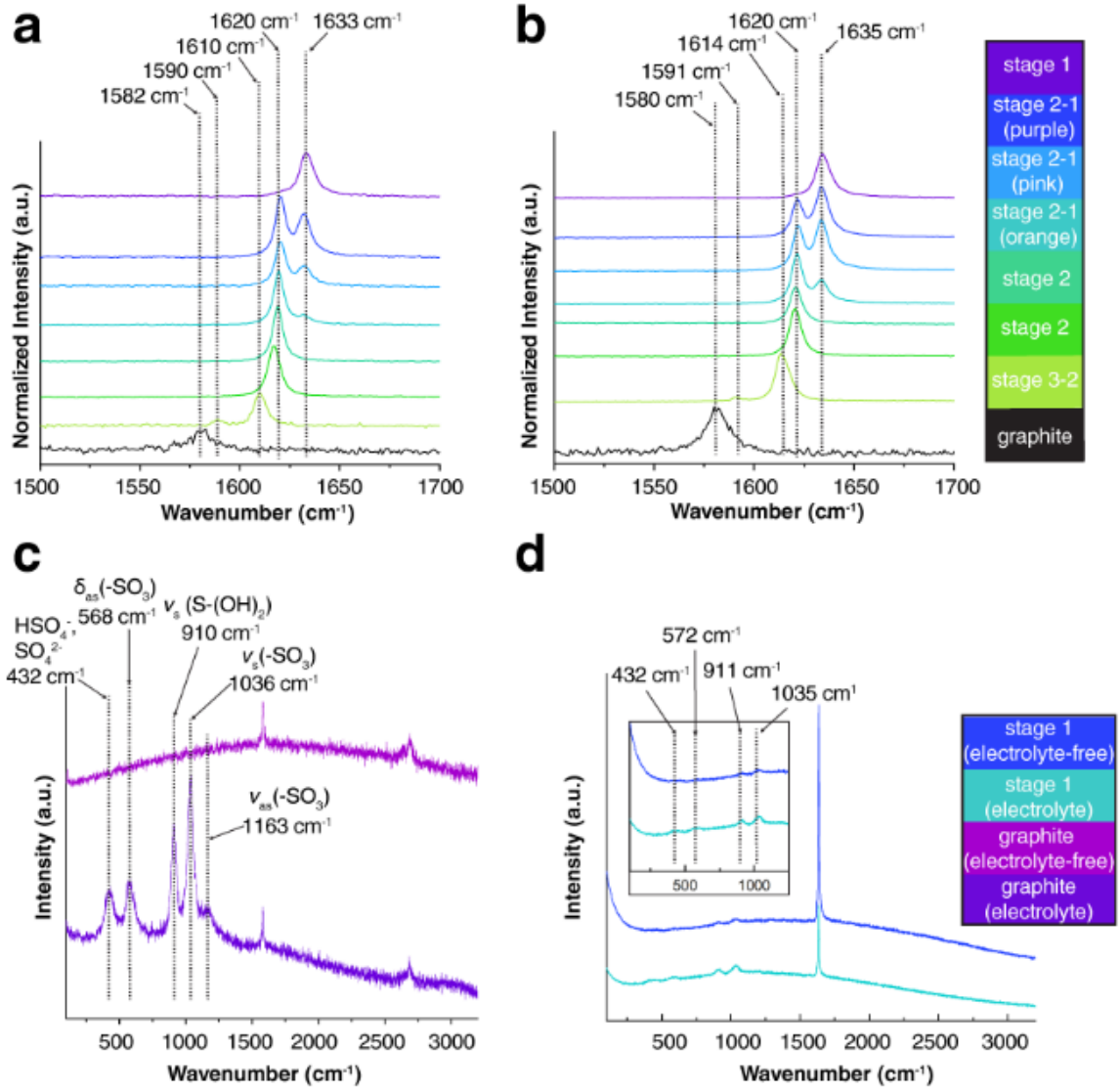


Figure 3-7. Raman shifts of the graphite G-peak in (a) the electrolyte and (b) the electrolyte-free regions during intercalation. The full Raman spectra from 100-3200 cm^{-1} for (c) HOPG

before intercalation and (d) stage 1 in the electrolyte and electrolyte-free devices. The curves have been vertically displaced.

every graphite layer was adjacent to an intercalant layer. During the stage 2-1 transition, we observed the splitting of the G-peak, since the transition region consisted of stage 2 and stage 1 as ions coalesced and reordered within the layers to form the stage 1 structure. When the material reached stage 1, the G-peak resolved into a single peak at 1635 cm^{-1}, which agrees well with previous reports[10,20] . It is also important to note that the D peak was not present in the spectra for the intercalated material, regardless of environment (**Figure 3-5**a,b).

The main difference between the Raman spectra of graphite taken in the electrolyte and electrolyte-free regions occurs at low frequencies (Figure 3-7c,d). Before intercalation, the spectrum taken in the electrolyte exhibited peaks corresponding to Raman shifts of the bisulfate and sulfuric acid species (Figure 3-7c). However, these peaks were absent in the electrolyte-free spectrum (Figure 3-7c), indicating that these components were not covering the surface of graphite. This further confirmed that signal is not passing through the electrolyte. As ions intercalated into the electrolyte-free region, low-frequency features emerged in the spectra (Figure 3-7d), indicating that bisulfate and sulfuric acid species[25] were present between the layers. Based on the Raman spectra (Figure 3-7d), we observed that bisulfate and sulfuric acid species are present in the stage 1 material for the electrolyte and electrolyte-free devices.

3.6 UV-Vis Spectroscopy

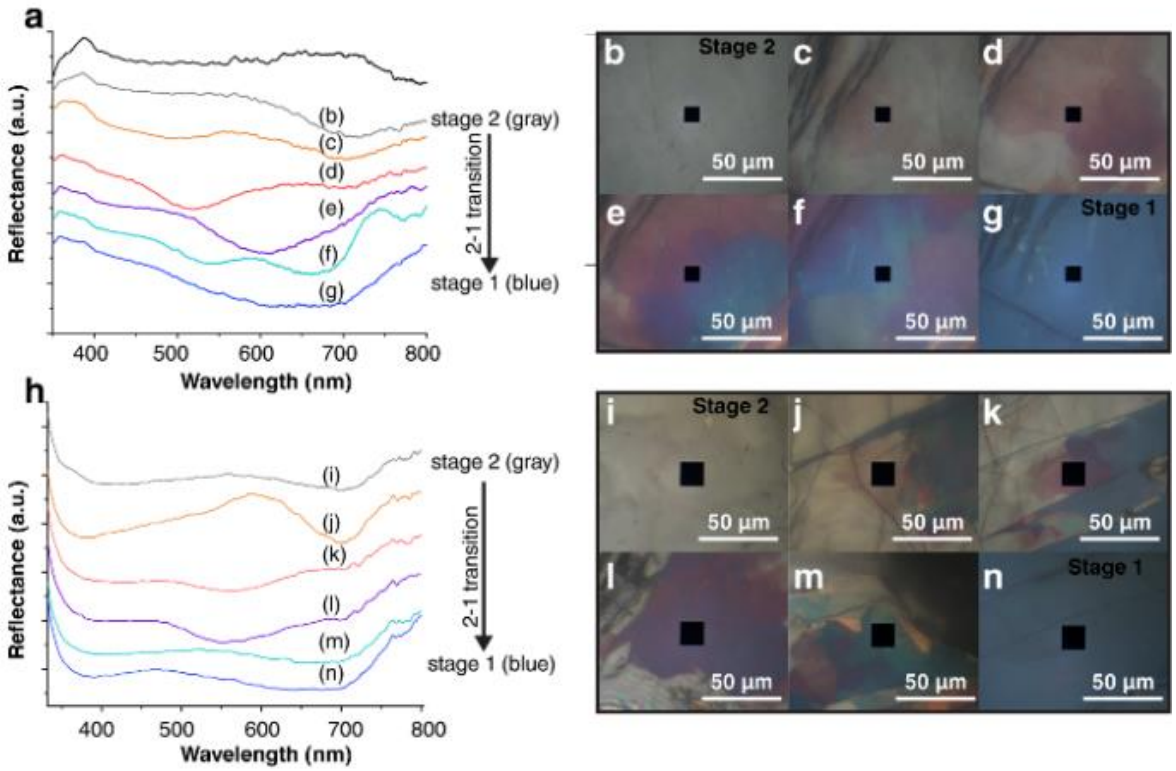


Figure 3-8. In-situ visible reflectance spectra of graphite in (a) the electrolyte and (h) the electrolyte-free environments. Spectra were taken at the points indicated in the optical images shown on the right. These images correspond to the following lines on (a) and (h). (b),(i) stage 2, and (c)-(f), (j)-(m) stage 2-1, and (g), (n) stage 1 in the electrolyte and electrolyte-free regions, respectively.

To spectroscopically probe the electronic structure of graphite in the electrolyte and electrolyte-free region in the visible, we took reflectance spectra *in-situ* from 350-800 nm (**Figure 3-8**). Graphite is a semi-metal, with a relatively flat reflectance spectrum in the visible (Figure 3-8a). Upon intercalation with bisulfate, the carrier concentration of graphite increased significantly, which caused the plasma frequency to shift into the visible (Figure 3-8a,b). Our results indicate that the reflectance minimum is between 650-720 nm for stage 1, which agrees with previous reports[9,10]. Interestingly, higher energy features appear during the stage 2-1

transition (Figure 3-8c-f,j-m). These features could be attributed to interference patterns, such as those that are observed in thin films[26].

3.7 FTIR-Spectroscopy

Finally, we performed spectroscopy in the mid-IR to demonstrate the advantage that probing the electrolyte-free region offers. First, we compared the features of the electrolyte region (**Figure 3-9**a) with those in the electrolyte-free region (Figure 3-9b). Since the electrolyte covers the surface of graphite in the electrolyte region, the spectrum reflects the absorption from the bulk electrolyte rather than from bisulfate species between the layers of graphite. The vibrational shifts from the electrolyte spectrum match well with studies[21,27,28] on the IR absorption of bisulfate and indicate the presence of O_3S-OH, O=S=O, -SO_3, and H_3O^+ groups. We compared this spectrum to spectra taken in the electrolyte-free region before and during intercalation as well as after deintercalation (Figure 3-9b). Initially in the electrolyte-free region, we observed a relatively flat reflectance of graphite. As bisulfate intercalated, features corresponding to absorption from bisulfate groups emerged. In addition, the stage 1 spectrum displays bands that appear near 1295 and 1700 cm^{-1}, which have been assigned to the H-O-H bending modes of H_3O^+ [29]. Upon deintercalation, the bisulfate bands disappeared and the spectrum resembled that of the graphite before intercalation, suggesting that the insertion of the bisulfate species is reversible under the appropriate conditions. Although features in the electrolyte-free region appeared to be similar to those expected from the sulfuric acid/bisulfate spectrum (Figure 3-9a), the Raman and IR active asymmetric S-O stretching mode of bisulfate at ~1195 cm^{-1} is notably absent in the intercalated material (Figure 3-7d, Figure 3-9b).

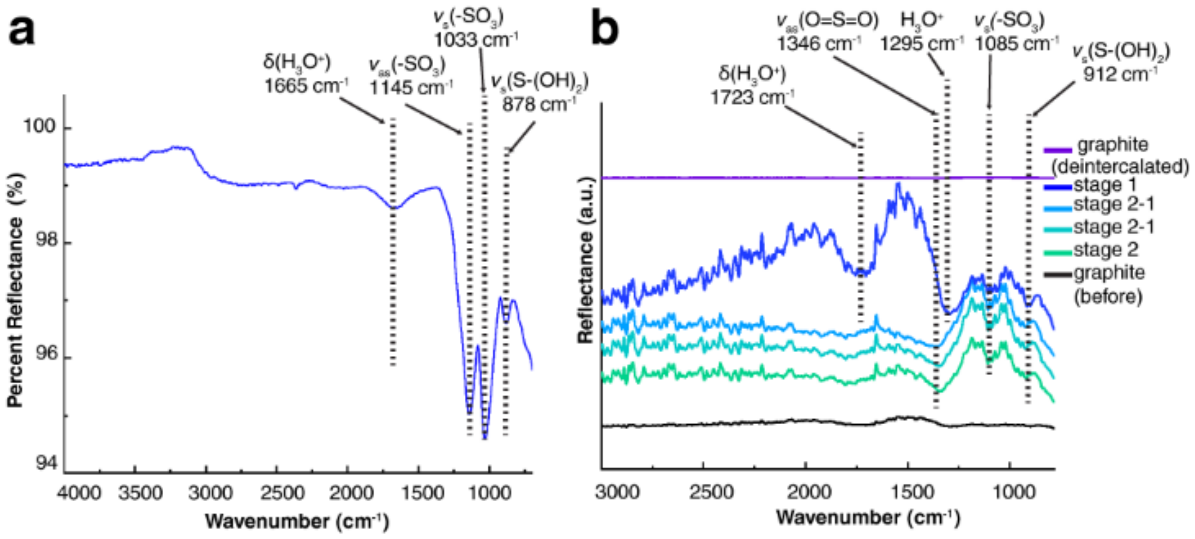


Figure 3-9. Mid-infrared spectra of the electrolyte region (a) and the electrolyte-free environment (b) during intercalation. The curves have been vertically displaced.

The orientation of the bisulfate ions within the layers of graphite could provide an explanation for the absence of the asymmetric modes, as has been hypothesized in studies on bisulfate adsorption on metallic electrodes.[29] For example, if the bisulfate ions were oriented between the layers in such a way that the asymmetric mode were obstructed, absorption from that mode would be weak or nonexistent. However, the absence of a single mode is not enough to assign orientation and motivates studies of other vibrational modes, particularly those at lower frequencies (< 600 cm^{-1}). [29] Our findings highlight that IR spectroscopy in an electrolyte-free environment could offer valuable insight into the presence of functional groups or the orientation of ions/molecules in layered materials *in-situ*.

3.8 Conclusions and Future Work

In summary, we have designed a device that enables us to perform *in-situ* spectroscopy in a planar geometry without signal passing through the electrolyte. Our results provide a

strong motivation for probing electrode materials in an electrolyte-free region. In addition, the qualitative differences we observed via optical microscopy call for detailed modeling to quantify the kinetics of intercalation in an electrolyte vs. electrolyte-free environment. Notably, our device also provides a platform to analyze *in-situ* other electrode-electrolyte systems in which electrolyte interferes with the technique, such as X-ray diffraction or X-ray and ultraviolet photoelectron spectroscopies. We propose that this device is generalizable to any other system in which the host material is layered, the lateral size of the host material is sufficient to create a barrier, and there is adequate driving force to induce ion transport between the two regions. Such work will contribute to the design and analysis of electrode materials for optoelectronics and energy storage applications.

REFERENCES

[1] M. S. Stark, J. Cheng, H. Kim, K. L. Kuntz, S. C. Warren, *Small* **2020**, *17*, DOI 10.1002/smll.202004823.

[2] V. Köhler, Thomas, Hanzig, Juliane, Koroteev, *Physcial Sci. Rev.* **2018**, *4*, 20170154.

[3] E. R. White, J. J. Lodico, B. C. Regan, *Nat. Commun.* **2017**, *8*, 1969.

[4] W. Bao, J. Wan, X. Han, X. Cai, H. Zhu, D. Kim, D. Ma, Y. Xu, J. N. Munday, H. D. Drew, M. S. Fuhrer, L. Hu, *Nat. Commun.* **2014**, *5*, 4224.

[5] K. Ni, X. Wang, Z. Tao, J. Yang, N. Shu, J. Ye, F. Pan, *Adv. Mater.* **2019**, *31*, 1808091.

[6] M. S. Dresselhaus, G. Dresselhaus, *Adv. Phys.* **1981**, *51*, 1.

[7] M. S. Stark, K. L. Kuntz, S. J. Martens, S. C. Warren, *Adv. Mater.* **2019**, *31*, 1.

[8] G. . Hennig, *Prog. Inorg. Chem.* **1959**, *1*, 126.

[9] G. R. Hennig, *J. Chem. Phys.* **1965**, *43*, 1201.

[10] A. M. Dimiev, G. Ceriotti, N. Behabtu, D. Zakhidov, M. Pasquali, R. Saito, J. M. Tour, *ACS Nano* **2013**, *7*, 2773.

[11] A. M. Dimiev, K. Shukhina, N. Behabtu, M. Pasquali, J. M. Tour, *J. Phys. Chem. C* **2019**, *123*, 19246.

[12] N. Daumas, A. Hérold, *C.R. Hebd. Seances Acad. Sci., Ser. C* **1969**, *268*, 373.

[13] R. Nishitani, Y. Sasaki, Y, Nishina, *Synth. Met.* **1989**, *34*, 315.

[14] P. C. Eklund, D. S. Smith, V. R. K. Murthy, *Synth. Met.* **1981**, *3*, 111.

[15] J. Wan, W. Bao, Y. Liu, J. Dai, F. Shen, L. Zhou, X. Cai, D. Urban, Y. Li, K. Jungjohann, M. S. Fuhrer, L. Hu, *Adv. Energy Mater.* **2015**, *5*, 1401742.

[16] A. Metrot, J. E. Fischer, *Synth. Met.* **1981**, *3*, 201.

[17] P. C. Eklund, in *Intercalation Layer. Mater.* (Ed.: M.S. Dresselhaus), Springer, New York City, USA, **1986**, pp. 337–344.

[18] W. Rudorff, *Zeitschrift fur Phys. Chemie.* **1940**, *45B*, 42.

[19] G. Aronson, S, Frishberg, C, Frankl, *Carbon N. Y.* **1971**, *9*, 715.

[20] D. C. Alsmeyer, R. L. Mccreery, *Anal. Chem.* **1992**, *64*, 1528.

[21] K. L. Nash, K. Jessica Sully, A. B. Horn, *J. Phys. Chem. A* **2001**, *105*, 9422.

[22] M. Pourbaix, *Natl. Assoc. Corros.* **1974**.

[23] Y. W. Alsmeyer, R. L. McCreery, *Anal. Chem.* **1991**, *63*, 1289.

[24] K. Persson, V. A. Sethuraman, L. J. Hardwick, Y. Hinuma, Y. S. Meng, A. van der Ven, V. Srinivasan, R. Kostecki, G. Ceder, *J. Phys. Chem. Lett.* **2010**, *1*, 1176.

[25] R. M. Bell, M. A. Jeppesen, *J. Chem. Phys.* **1935**, *3*, 245.

[26] H. Anders, *Thin Films in Optics*, Focal Press, London, **1967**.

[27] A. B. Horn, K. J. Sully, *Phys. Chem. Chem. Phys.* **1999**, *1*, 3801.

[28] K. Kunimatsu, M. G. Samant, H. Seki, *J. Electroanal. Chem.* **1989**, *272*, 185.

[29] K. Kunimatsu, M. G. Samant, H. Seki, *J. Electroanal. Chem.* **1989**, *258*, 163.

CHAPTER 4 – STAGING DYNAMICS AND ION TRANSPORT RATES IN GRAPHITE ELECTRODES

4.1 Introduction

Designing better electrode systems for optoelectronics and energy storage motivates fundamental studies of intercalation and staging dynamics in electrode materials. However, despite significant advances and a vast amount of literature on intercalation[1–4], the mechanisms of staging, ion transport, the optical properties, and the influence of structure are still areas of interest for even the most common intercalation compounds[1,5–8]. The lag in progress is partially driven by the need for new tools to systematically study (de)intercalation in-situ, with high spatial resolution[1,9]. Spatially-resolved optical measurements can reveal staging dynamics and provide insight into the mechanism of intercalation.[6,10] However, it is important to understand the origin of the features observed in these techniques.

In our previous work, we identified a series of colors that emerge during the stage 2-1 transition in the graphite-bisulfate system[9] (Figure 4-1a). Although these transitory colors had been described as wavefronts, subfronts[10], or intercalant islands[5], it was still unclear what was the origin of these colorful phases. In-situ experimental observations offered some insight into a possible solution. Raman spectra of the stage 2-1 transition, demonstrate that the G-peak splits into two peaks at 1620 cm^{-1} and 1635 cm^{-1}, representing graphite layers in a stage 1 or stage 2 environment respectively[5,9,10]. As the colors progress from orange to purple, the stage 1 component becomes more intense, while the stage 2 component decreases in intensity[5,9,10]. In addition, in-situ UV-vis reflectance measurements of the colored regions also indicate that

different colors have different carrier concentrations[9]. The spectra show several dips in reflectance across the visible, which seem to agree with the observed color of the regions[9]. These colors likely emerge from distinct carrier concentrations from the stage 1 and stage 2 regions during the stage transition. Since there are different carrier concentrations in stage 1 and stage 2, it is probable that there is also complex coupling between carriers, in addition to inter- and intra-band absorption. Despite the complexities of the absorption spectra, these observations led us to hypothesize that the colors may represent a series of substages, which we define here as the periodic ordering of stage 1 and stage 2 regions within local domains (Figure 4-6). The scheme in Figure 4-6 presents a simplified picture of the transition from stage 2 to stage 1, with each consecutive color representing a substage with a higher stage 1 content. We defined the ratios, based on assumptions from electrostatics, since it is unlikely that electrostatic repulsion would drive periodic ordering further than ~2 nm (6 layers) away.[11] Thus, the simplest mechanism would be for orange to exhibit a 2:1 (filled:empty) ratio initially. As intercalation progresses, the domains can slide along the graphite layer to achieve a 3:1 ratio (magenta), followed by 4:1 ratio (purple) and 5:1 (cyan) in local domains.

To examine the hypothesis of substages, here we describe a video analysis platform that we developed to probe the color patterns and ion transport kinetics in the bisulfate GIC. This program enabled us to clearly visualize the (de)intercalation process and isolate distinct colors through masking and pixel quantification. In addition, implementing optical flow algorithms results in speed distributions, which offer insight into the rates of transport for (de)intercalation, colors, and specific domains. These results tend to support a substage model and suggest that the mechanism for (de)intercalation is strongly influenced by electrostatic repulsion, strain, and local structure, which complements other experimental work[5,9].

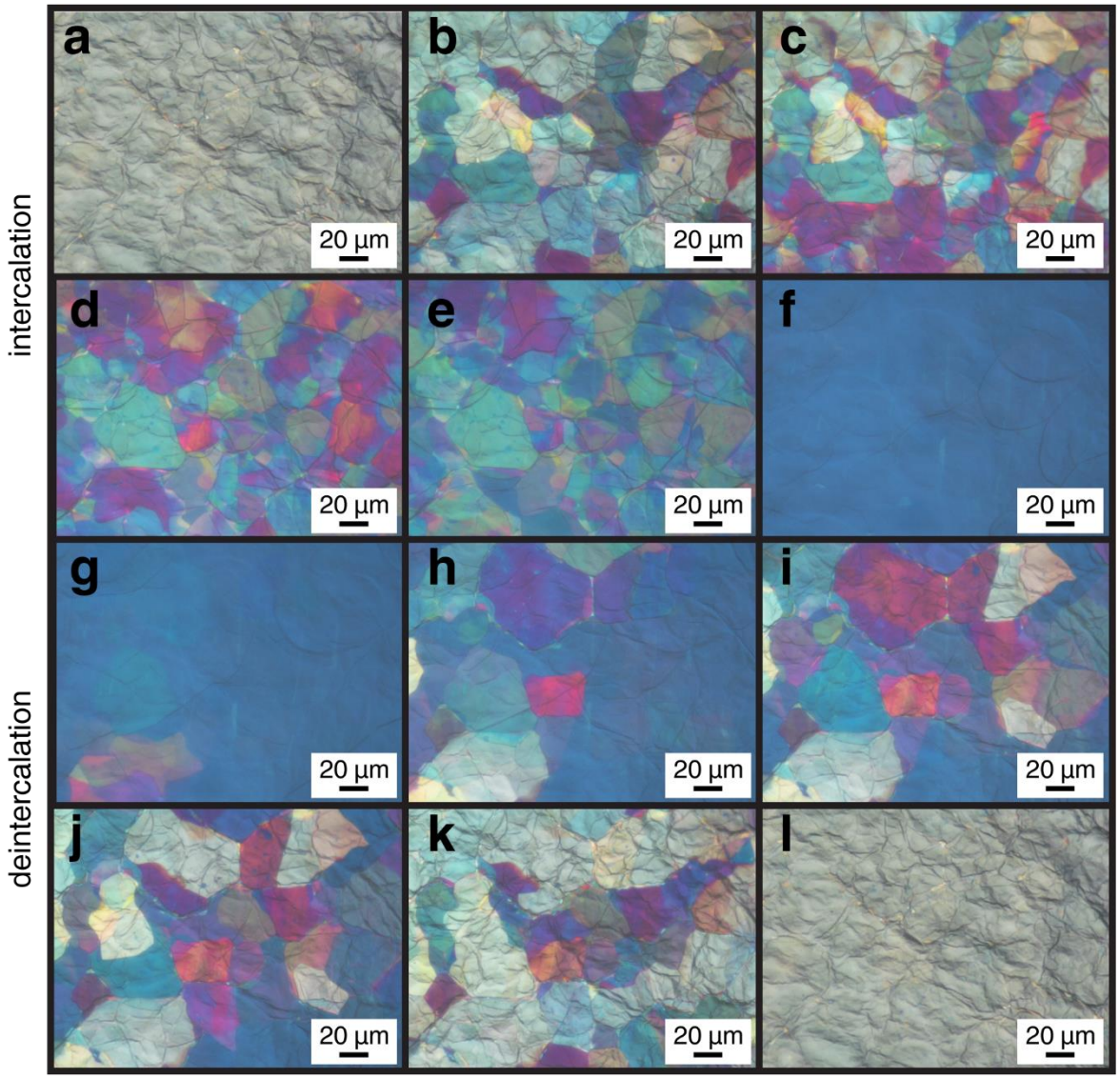


Figure 4-1: Optical microscopy images showing the domains of color during (a-f) intercalation and (g-l) deintercalation.

4.2 Developing the Image Analysis Program

The image analysis program we designed in this work has 5 parts: 1) Masking, 2) Edge detection, 3) Velocity calculation, 4) Cropping, and 5) Counting pixels, which are described below. These components enabled us to design a platform where we could perform image sequence analysis to better understand the intercalation rates in intercalation compounds. Here,

I describe the methods we used to create this program, including the sources we found helpful and the rationales behind the coding choices we made during the development process.

4.2.1 Masking methods

In image analysis, thresholding is a standard technique to process images. If a pixel in an image has a value less than the threshold value, that pixel is assigned a value (i.e. black). If the pixel has a value greater than the threshold value, it is assigned a different value (i.e. white). Thus, thresholding enables to select certain regions of interest in an image based on the values (color) of individual pixels. During thresholding, there are two important considerations that must be taken into account: 1) colorspace and 2) threshold range. Color space is a critical factor in image processing and segmentation because the geometry of the color space can lead to better separation for thresholding[12,13].

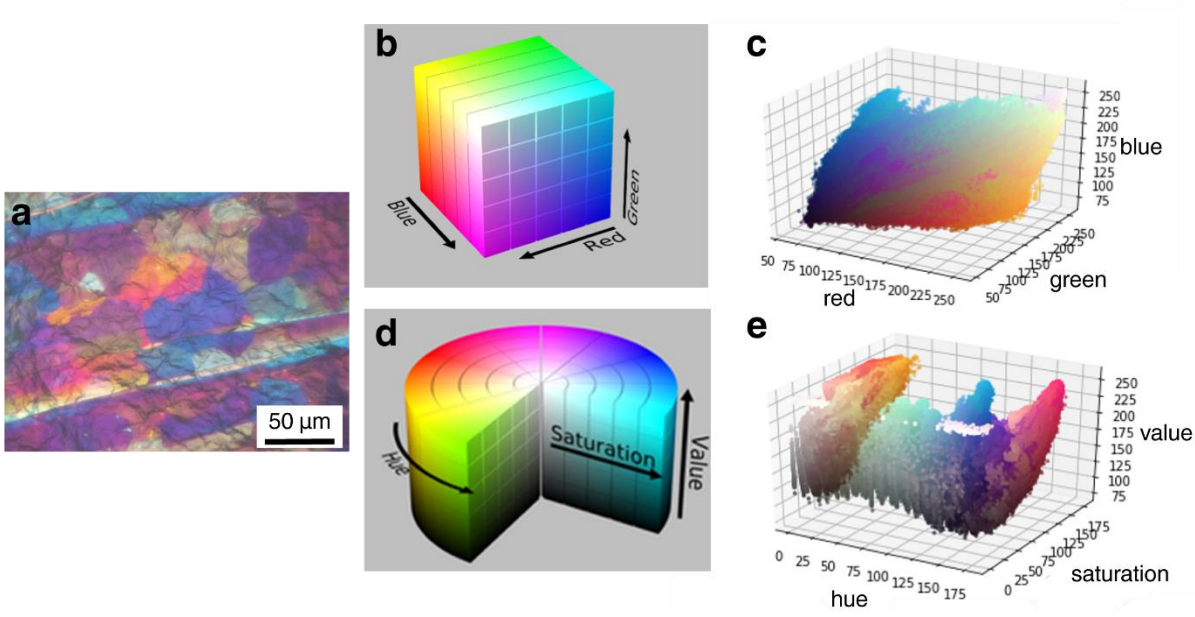


Figure 4-2: Comparison of the pixel groupings that result from segmentation of a) a representative image using b) cubic RGB color space in c) and d) the cylindrical HSV color

space in e) (b and d reproduced from reference[14]).

For example, we attempted to use the RGB colorspace initially to cluster the colors from the optical images (Figure 4-2a-c). However, as Figure 4-2 shows, RGB is a cubic color space, and the distance between certain colors, such as X and Y is small. Even with a finely-tuned threshold range, the separation between adjacent colors may not be sufficient using this color space, resulting in pixels being assigned incorrectly during thresholding. Therefore, the cylindrical HSV (hue, saturation, value/brightness) is the preferred color space for image processing since it results in better separation of pixel values (Figure 4-2a,d-e). Hue ranges from 0-360^{o}, Saturation ranges from 0-255, and Brightness ranges from 0-255. To threshold the colors in our intercalation image sequences, we implemented functions from OpenCV, a package that contains a series of programming functions for image processing and computer vision techniques[15]. It is important to note, that although HSV is a cylindrical color space, with Hue ranging from 0^{o} to 360^{o}, OpenCV uses 0^{o} to 180^{o}, with Saturation and Brightness maintaining the same ranges[12,14,15]. These functions enabled us to assign pixels within a certain range to a specific color (Figure 4-3). For example, we identified the range for the blue color that appears at pure stage 1. The lower end of the range has HSV values of (102, 50, 50) with the higher end of the range being (120, 255, 255).

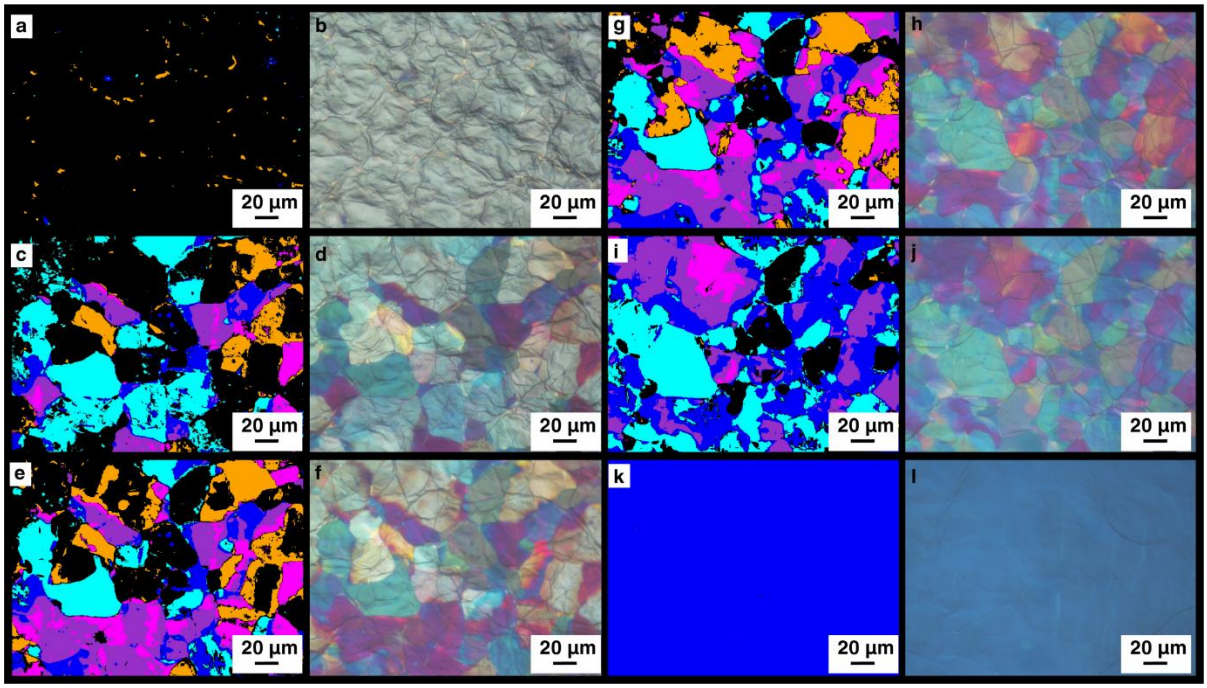


Figure 4-3: Color masks (a,c,e,g,i,k) that result from image segmentation of the frames (b,d,f,h,j,l) using the methods described in this section.

Once we identify the threshold range for the blue pixels, we can use the OpenCV function, cv2.inRange, to define that threshold range as blue:

```
blue = cv2.inRange(image,(low_h, low_s, low_v), (high_h, high_s, high_v))
```

where image is the image to be thresholded, low_h, low_s, low_v and high_h, high_s, high_v are the lower and upper HSV bounds of the threshold range, respectively. Once we have defined pixels in this range as blue, we can then reassign the value (color) of those pixels, using a for loop:

```
for j in zip(*np.where(blue == 255)):
  image [j[0], j[1], 0] = 255
```

```
image [j[0], j[1], 1] = 0
image [j[0], j[1], 2] = 0
```

where j refers to each pixel in the image. These lines of code loop through each pixel in the image and when a pixel is in the blue range (np.where(blue == 255)), it reassigns each channel of the pixel (0, 1, or 2) to values in the RGB color space (BGR in OpenCV). Although we reassign the color to be blue here, the pixel values could be assigned to any color. We repeated this process for each color in the image, creating masks of the five dominant colors in the optical microscopy videos (Figure 4-3).

4.2.2 Edge detection method

Before quantifying intercalation velocities, we identified the edges of the color domains using edge detection techniques. Canny edge detection is the method commonly used in image segmentation to isolate specific ROIs or the boundaries of a structure[15,16]. In general, there are 3 steps in the canny edge detection algorithm, as follows: 1) Blurring, 2) Sobel edge detection, 3) Removing non-edge pixels[15]. Here, we detail these steps and highlight the specific parameters used in our code.

The first step in Canny edge detection is blurring with a Gaussian blur by applying a low-pass filter to remove noise from the image. This process creates a smooth transition from the image of an object to the background or another object by averaging out changes in pixel intensity at the edges[15]. To implement a blur, a rectangular group of pixels (i.e. the kernel) surrounding the filter pixel is selected. The dimensions of these kernels must be odd. Then, the algorithm takes the weighted average of the pixels in the kernel, with pixels closer to the center weighted more strongly than those further away[15,16]. This filtering occurs for each channel of

the pixel and the weighted average for each channel replaces the pixel value at the center of the kernel. Based on this, the larger kernels will result in a greater degree of blurring, whereas smaller kernel sizes have less blurring.

Next, Sobel edge detection identifies the intensity gradients that occur at the edges of objects in an image[15]. To find the intensity gradients, the derivative of the curve that fits the gradient between light and dark areas in the image is computed. The maximum of that derivative determines the location of an edge pixel[15]. Pixels at locations where the derivative is not at a maximum are removed. Sometimes, pixels that lie too far from an edge will be classified as edge pixels using the Sobel method, but non-maximum suppression removes pixels that are too far from an edge. When the gradient value of a pixel is above the threshold, it is likely to be an edge site. Similarly, a low gradient value will result in the pixel being eliminated. An intermediate value requires further analysis through a technique known as hysteresis. Hysteresis surveys the intermediate edge candidates to see whether they are adjacent to strong edge pixels. If so, they are defined as edge pixels and if not, they are eliminated.

Based on this process, we implemented the Canny edge method in our program, using the cv2.Canny function and defined the lower and upper bounds for the threshold as follows:

```
sigma = 0.33
v = np.median(frame)
lower = int(max(0, (1.0 - sigma) * v))
upper = int(min(255, (1.0 + sigma) * v))
if ((upper - lower) > 10):
    edged = cv2.Canny(frame, lower, upper)
```

else:

```
edged = cv2.Canny(frame, 100, 200)
```

We have the option to tune the sigma function to modulate the degree of Gaussian blurring as well as the upper and lower threshold bounds to determine which pixels will be removed. The above parameters are the ones that we found to work best for detecting edges in the intercalation videos. Figure 4-4 shows an image that has been masked (Figure 4-4a), and the resulting frame after edge detection (Figure4-4b).

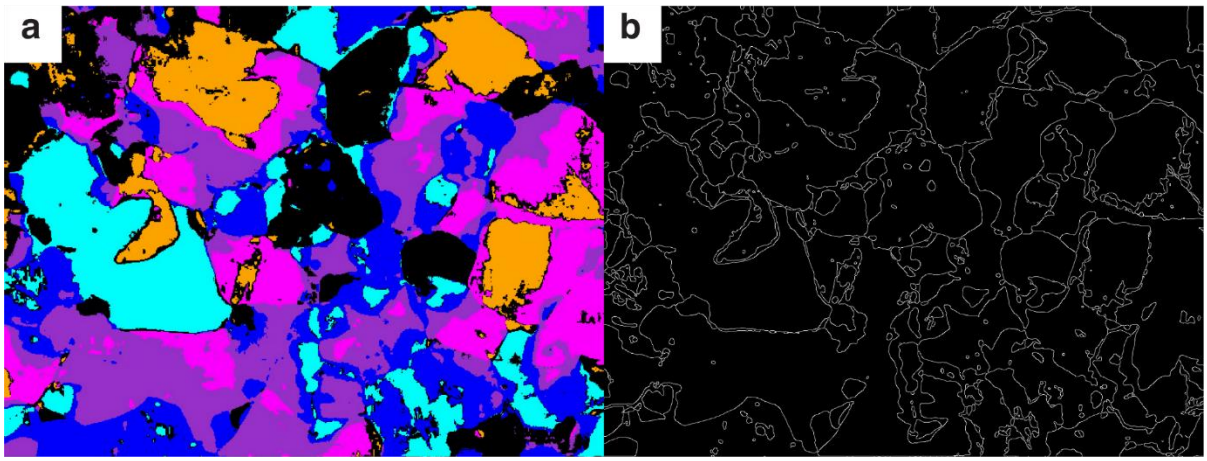


Figure 4-4: A frame that has a) undergone image segmentation and recoloring, and b) subsequent Canny edge detection.

4.2.3 Velocity calculation method

After detecting the edges in the images, we turned to optical flow from computer vision methods[15] to calculate the velocities of the moving edges. Optical flow is defined as the motion of an object (or the camera) between two consecutive frames of an image sequence[15,17]. Figure 4-5 illustrates the basic concept of optical flow. In optical flow methods, a pixel with intensity I at position and time (x, y, t) moves by dx and dy over time t. The new

pixel intensity is then I(x+dx, y+dy, t+dt). If the pixel intensities are constant between the two frames, a Taylor series approximation is applied to the two sides:

$$\frac{dI}{dx}\delta x + \frac{dI}{dy}\delta y + \frac{dI}{dt}\delta t = 0$$

Then, the dividing by δt:

$$\frac{dI}{dx}u + \frac{dI}{dy}v + \frac{dI}{dt} = 0$$

where u = δx/δt, v = δy/δt. For this equation, it is important to note that dI/dx and dI/dy are the image gradients along the horizontal and vertical axes respectively and dI/dt is the image gradient along the time axis.[17]

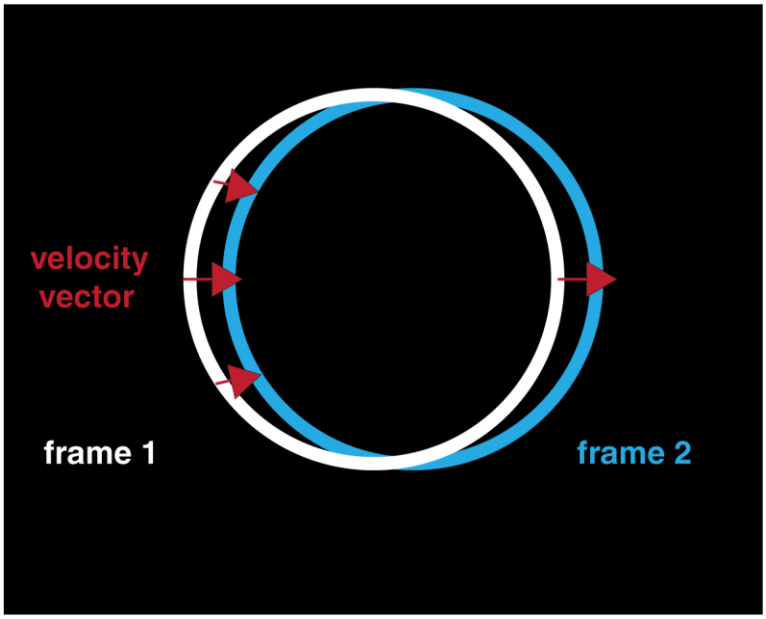


Figure 4-5: Illustration of optical flow, where the white circle represents an object to be tracked in frame 1. The blue circle represents the displacement of the object after a certain amount of time to in frame 2. The optical flow methods calculate the velocity vectors of the pixels in the object across frames.

Since this equation has two unknowns, the Lucas-Kanade or Gunnar-Farneback methods can be used to solve for the unknown variables[15,17]. The Lucas-Kanade method detects sparse optical flow, or the movement of a select number of pixels, usually at the corners of an object through a series of frames[18]. Although this method works well for applications, where the tracked objects appear to have a similar size and shape across multiple frames, (e.g. vehicles or pedestrians) the domains in our work change and disappeared through the videos. This feature created several problems with the Lucas-Kanade optical flow tracking. First, the algorithm selects a few points initially and compares the position of these pixels across multiple frames. However, when a domain disappeared, the algorithm did not adapt to select new pixels to track. Also, the domains did not have distinct corners, which prevented the

corner-detecting algorithm from identifying a sufficient number of points to track initially.

To remedy these issues, we turned to the Gunnar-Farneback method, which estimates the velocities between two frames based on a polynomial expansion[19]. In contrast to Lucas-Kanade, Gunnar-Farneback estimates dense rather than sparse optical flow. Dense optical flow tracks the movement of all pixels in an image from frame to frame instead of just the corner points. In this method, the intensity change of each pixel is measured between two frames and an image is generated with the pixels highlighted. Then, the magnitude and direction are calculated from the flow vectors (u, v)[19]. The magnitude of the vectors corresponds to the displacement, which we use to calculate the velocity. In OpenCV, the function for Farneback optical flow is cv2.calcOpticalFlowFarneback( ), with input parameters of the two frames to be analyzed as well as the size of the pixel neighborhood and the standard deviation of the Gaussian used to smooth the derivatives before polynomial expansion.

4.2.4 Data Analysis

We extracted the calculated displacements from the algorithm and exported them as a .csv file for further plotting and analysis. Before plotting the data, we binned the calculated velocities using the Scott method[20] from statistics to calculate the bin width for each plot:

$$bin\ width = \frac{1}{\sqrt[3]{N}} * \sigma * 3.49$$

where N is the number of data points, σ is the standard deviation, and the value of 3.49 is a standard constant[20,21]. Since the lower counts dominated the histogram, we weighted the data to account for contributions from higher rates, by multiplying the number of counts in each bin by the value of the bin. Then, we normalized the data to account for the intercalation area: Normalized Weighted Counts = weighted counts/(Sum of counts*bin width). The area is

normalized to a value of 1. Due to the area normalization process, each plot will intersect the other plots at some speed. After normalization, the data generally resemble a Boltzmann distribution, and can be analyzed in a similar way, with graphs that lie further to the right having higher rate distributions, compared to graphs that are further to the left.

4.3 Characterizing Staging Dynamics

The methods are described in detail in Section 4.2, but we will briefly summarize the process here. We performed image segmentation of videos across in the HSV color space. This step reassigns the channels of each pixel to either orange, magenta, purple, cyan, blue, or black. Then, these frames with the new colors are compiled, creating a video with the masked colors (Figure 4-3). Masking the colors offers a unique opportunity to confirm the color patterns we observe during (de)intercalation by removing distracting features and enabling us to focus on individual domains. Next, Canny edge detection is performed on the frames in the masked video (Figure 4-4) to eliminate extraneous pixels for velocity calculations. Finally, the optical flow algorithm tracks the displacement of the edge pixels over time, enabling us to estimate the rates of ion transport.

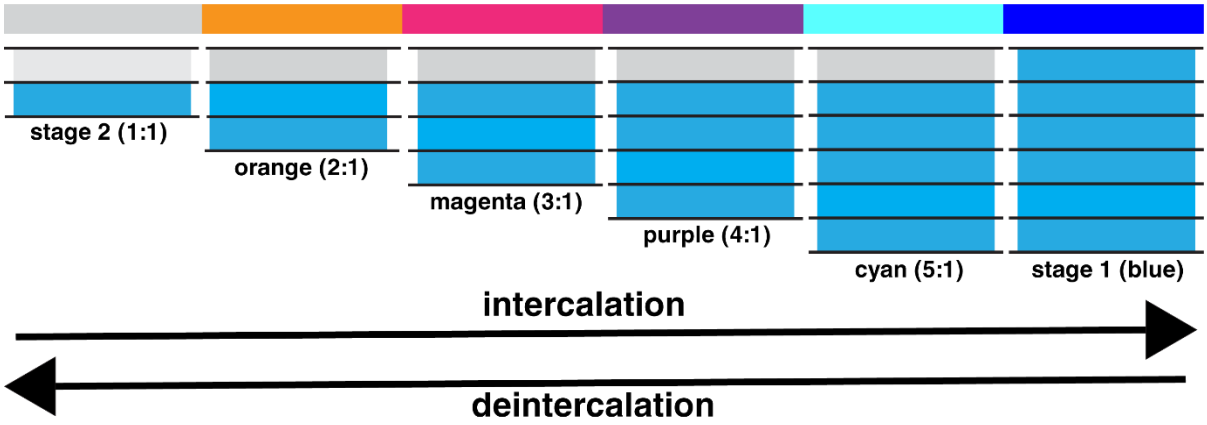


Figure 4-6: Scheme that illustrates what the periodic patterns in local domains could look like, with ratios indicating the ratio of filled to unfilled layers. This progression could enable the formation of orange, magenta, purple, cyan, and blue (stage 1), during the stage 2-1 transition during (de)intercalation.

With the masked videos, we can quantify the number of pixels for each color as well as the order of colors that appear over time during (de)intercalation (Figure 4-7). Importantly, these plots confirm the ordering of colors for intercalation that we identified in our previous work[9] and suggest that the ordering for deintercalation is the reverse. The idea of ordered substages is strengthened by the exact reversal of the colors during deintercalation (Figure 4-1g-l, 4-7b), where the pattern is blue, cyan, purple, magenta, and orange, compared to orange, magenta, purple, cyan, and blue during intercalation (Figure 4-1a-h, Figure 4-7a). Qualitative observations of (de)intercalation via optical microscopy suggest that deintercalation (24 minutes) takes longer to complete than intercalation (15 minutes). To observe whether this difference can be quantified, we calculated the (de)intercalation speeds using the Gunnar-

Farneback optical flow method.

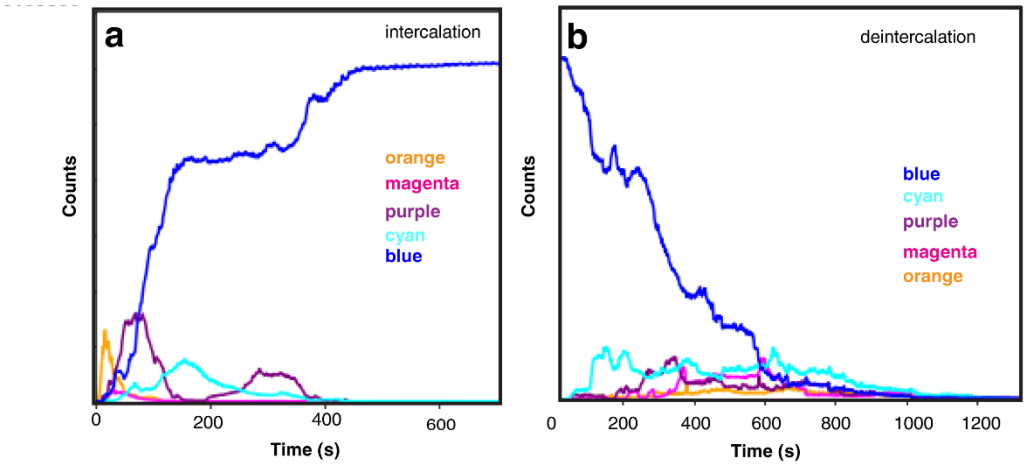


Figure 4-7: Demonstration of how the colors emerge over time during a) intercalation and b) deintercalation. For intercalation, colors tend to appear in the following order: orange, magenta, purple, cyan, and blue. The pattern is the reverse for deintercalation

The corresponding speed distribution is shown in Figure 4-8. Here, the intercalation profile lies to the right of the deintercalation profile, indicating that the rates for intercalation overall are faster than the deintercalation rates, which agrees with qualitative predictions from optical microscopy image sequences. This difference could be attributed the fact that there are empty galleries present during intercalation before the stage 2-1 transition. These galleries would enable the intercalant islands to slide rapidly to a domain. However, at stage 1, all of the galleries are filled with ions. In order for ions to deintercalate a domain, there must be open pathways that are adjacent to that domain. Once ions at the edges of the material have deintercalated, ions in the center of the graphite, can begin to deintercalate. The lack of available pathways to the edge of the graphite slows down the overall rate of transport during deintercalation. Structural changes to the graphite during intercalation could also result in a

different deintercalation rate.

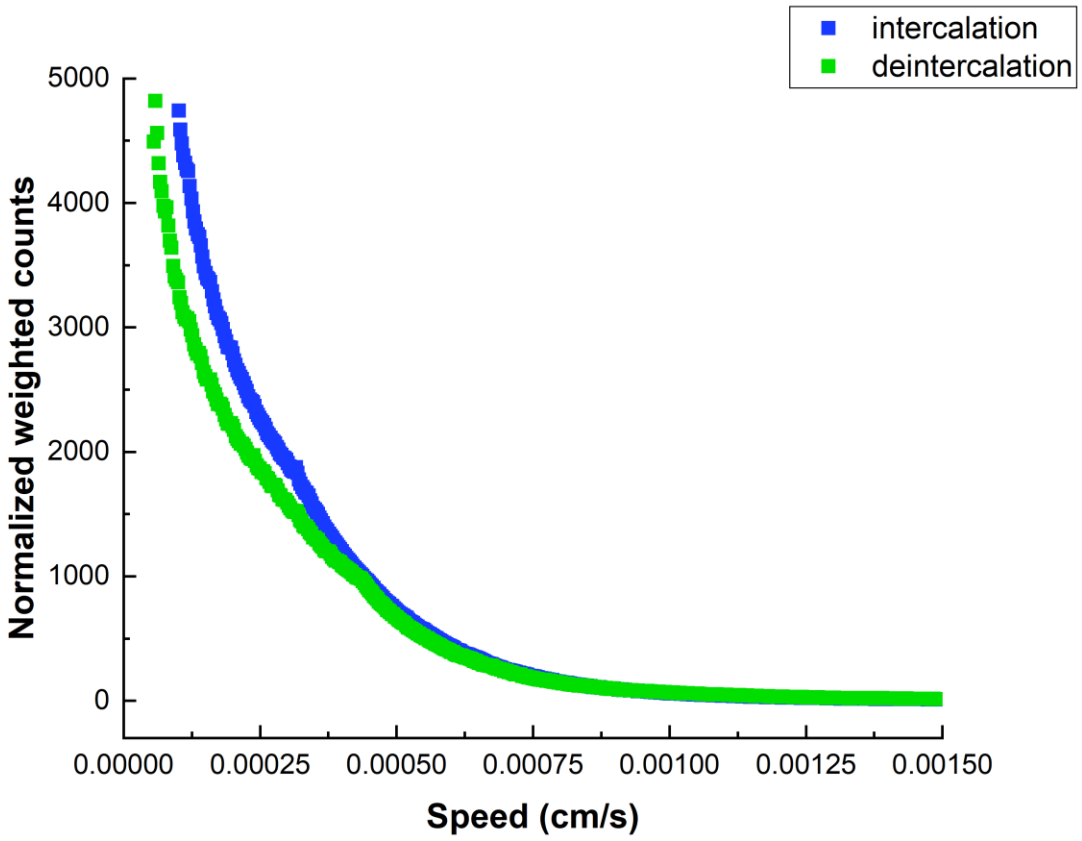


Figure 4-8: Comparing the distribution of speeds for a) intercalation and b) deintercalation.

To gain deeper insight into the (de)intercalation process, we investigated the rates of individual colors during intercalation and deintercalation (Figure 4-9). Interestingly, we saw a decrease in rate with increasing stage 1 content (Figure 4-9a), with orange > magenta > purple > cyan > blue. Although the profiles for deintercalation (Figure 4-9b) exhibit greater overlap, there is still a clear trend: the rate decreases with decreasing stage 1 content, with blue > cyan

> purple > magenta > orange. This observation can be explained by considering that during intercalation, there is greater electrostatic repulsion and strain[1,3] with increasing intercalant concentration.

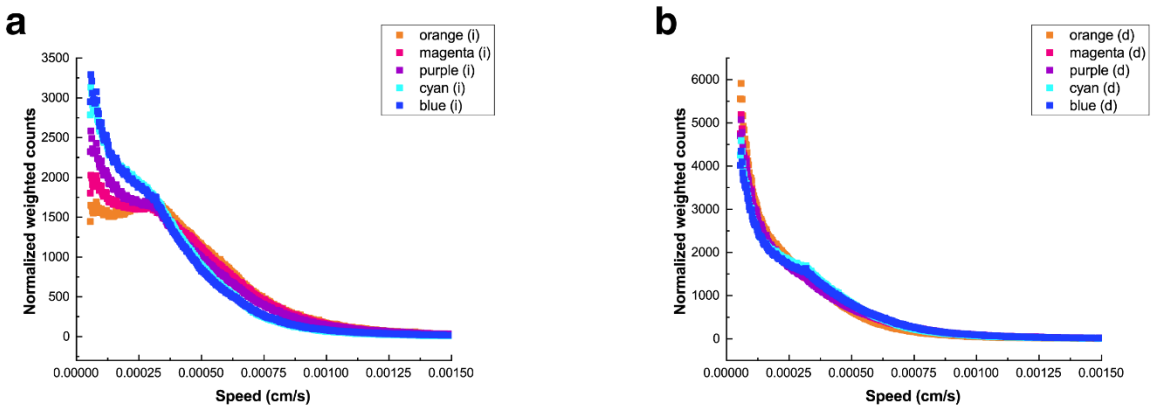


Figure 4-9: Comparison of the distribution of rates observed for each of the colors during a) intercalation and b) deintercalation.

It is also likely that there are favorable and unfavorable pathways for transport within the graphite lattice. Suppose that a local domain reaches the potential for the stage 2-1 transition. The intercalant islands begin to slide along the graphite layers to effect the transition to orange in that region. The conversion to orange would be rapid, since all pathways are open to transport. As more ions propagate toward the domain, the favorable pathways for transport could become blocked, forcing additional intercalant islands to take increasingly less favorable paths to reach their destination. During intercalation, both the electrostatic/strain and structural arguments would result in earlier substages exhibiting faster transport overall compared to later substages, which is what we observe in Figure 4-9a. During deintercalation, the trend in rates

is reversed, with blue and cyan exhibiting greater speeds than purple, magenta, and orange. Although there are fewer pathways available to blue/cyan initially, once routes become available, the transition occurs rapidly. This rapid transition is likely due to electrostatic effects, which are greater for the blue/cyan substages.

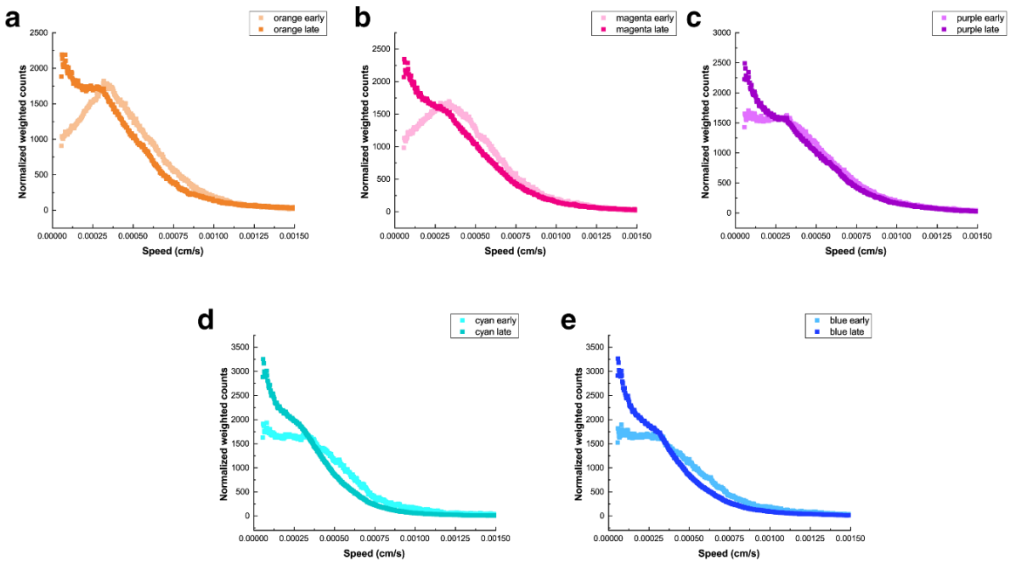


Figure 4-10: Comparing the distribution of rates during early and late times during intercalation for a) orange, b) magenta, c) purple, d) cyan, and e) blue.

To provide further insight into the possibility of transport pathways affecting rates, we analyzed the speeds at the initial appearance (early) and later propagation/disappearance (late) of each color for intercalation (Figure 4-10) and deintercalation (Figure 4-11). Interestingly, the early rates for all of the colors are faster than the later rates. We observe a similar trend for deintercalation (Figure 4-11). This observation can be explained by considering local graphite structure. For example, consider two domains, Domain 1, which is rapidly converted to purple

at an early time, and Domain 2, where the appearance of purple is slow. If Domain 1 is surrounded by favorable pathways, the transition could occur at an earlier time.

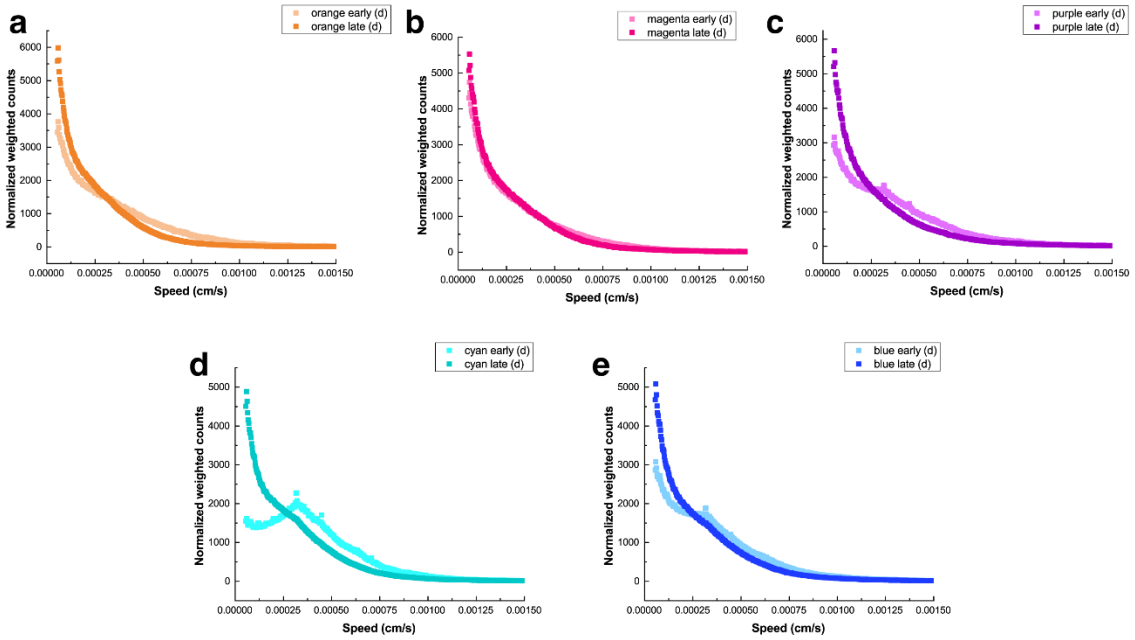


Figure 4-11: Comparing the distribution of rates during early and late times during deintercalation for a) orange, b) magenta, c) purple, d) cyan, and e) blue.

Conversely, if Domain 2 is adjacent to more resistive pathways, it may take the intercalant islands longer to reach that domain, and therefore the transition will be slower. This would result in different rates at earlier times compared to later ones, which is what we observe in Figure 4-10. Thus, structural considerations, such as the availability of transport pathways or the presence of a grain boundary, could inhibit or promote transport within domains at different times.

If availability of pathways were the dominant mechanism for deintercalation, we would expect to see faster rates at later times, as more pathways open up. Instead, we see the reverse: with early times exhibiting faster rates (Figure 4-11), for all of the colors. Initially, the majority

of pathways are blocked, yet blue and cyan move faster at earlier times (Figure 4-11d,e). Thus, it is likely that electrostatic repulsion and strain influence deintercalation[3,5]. Since stage 1 exhibits the greatest repulsion and strain between layers of adjacent intercalants[1,22], blue would be the most unstable. When the potential is reversed, the intercalant islands would move to alleviate the strain and reduce repulsion. Once pathways begin to empty, the ions have the option to choose between favorable and unfavorable pathways and this mechanism begins to compete with the stability of the substage.

If the availability of favorable transport routes does play a major role in (de)intercalation rates, we would expect to see difference among individual domains, since a region's proximity to favorable pathways would determine whether or not it would (de)intercalate rapidly. We analyzed 10 regions of interest (ROIs) during intercalation (Figure 4-12) and deintercalation (Figure 4-13). Overall, the rate profiles demonstrate that the rate distributions vary across domains and these differences tend to be more pronounced for intercalation (Figure 4-12a, b).

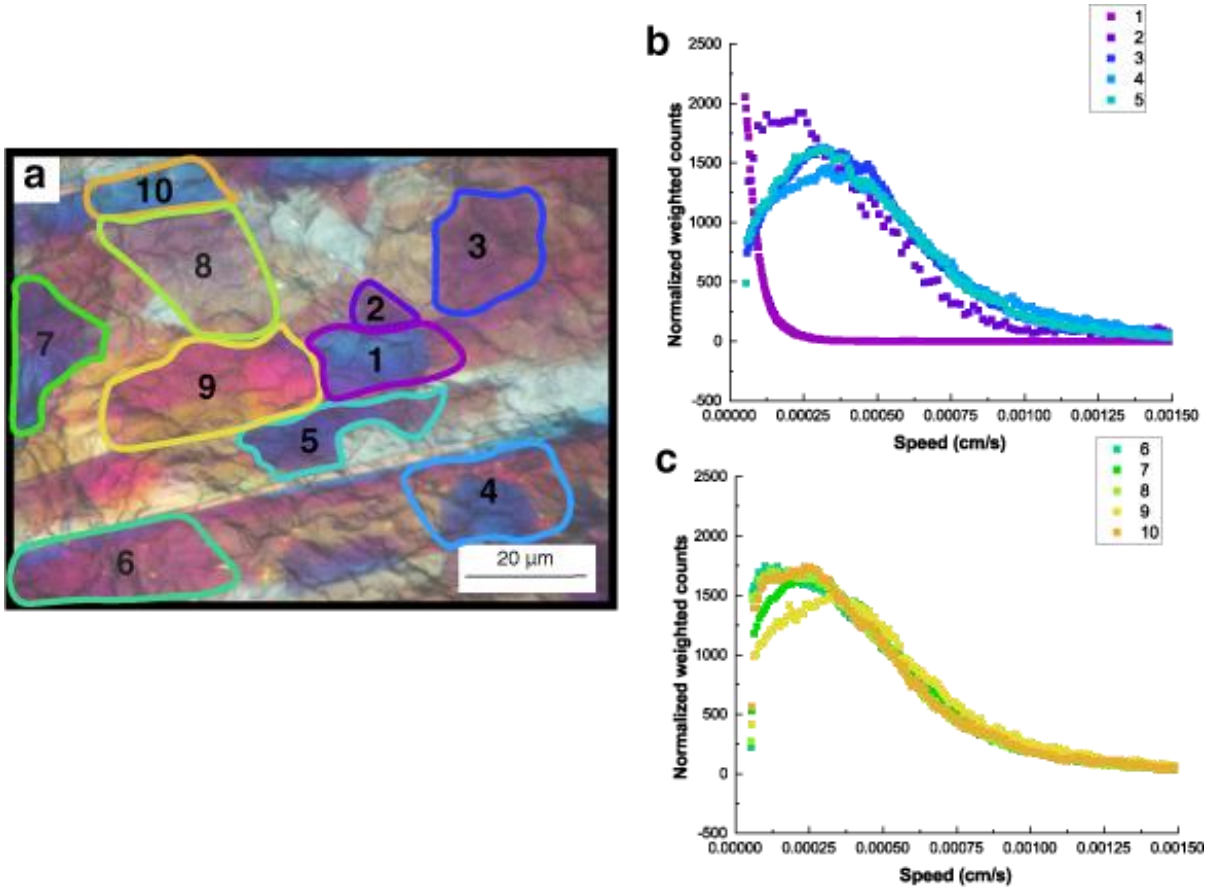


Figure 4-12: Investigating the speed distributions of a) individual domains during intercalation**.** The numbers in the legends in b) and c) correspond to the regions demarcated in a).

Based on these observations of inhomogeneity, we analyzed the color patterns and rate profiles for the substages for two ROIs during intercalation. Figure 4-14 shows the masked images, color profile, and speed distributions for ROI1 (ROI1 is also depicted in Figure 4-12). Based on the masked frames and the color plot, the evolution of the substages is straightforward: orange nucleates within the first 15 s of intercalation (Figure 4-14a,g). Then, magenta appears in the center of the domain and grows outward (Figure 4-14b,g). Purple also nucleates from the center and follows a similar growth pattern (Figure 4-14c,g). After the appearance of purple, blue nucleates and begins to fill the domain (Figure 4-14d).

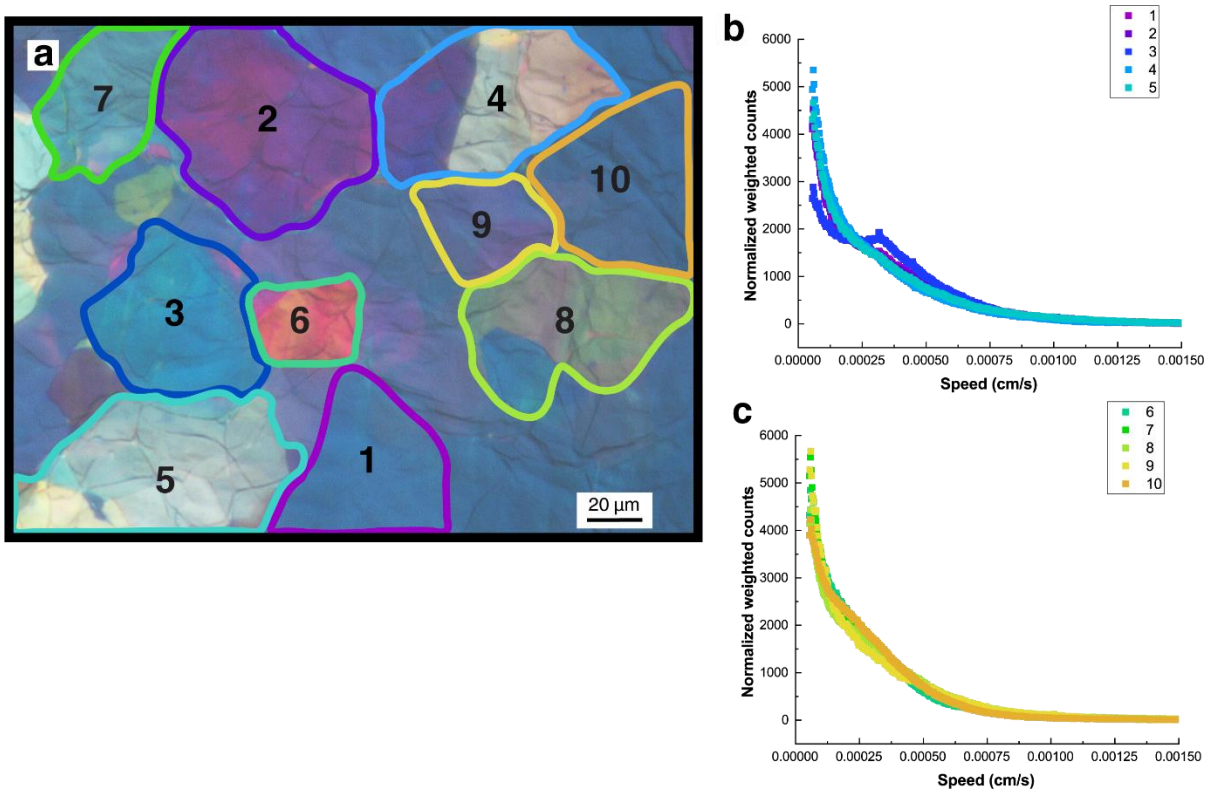


Figure 4-13: Investigating the speed distributions of a) individual domains during deintercalation**.** The numbers in the legends in b) and c) correspond to the regions demarcated in a)

However, instead of filling the domain completely, blue is displaced by cyan (Figure 4-14e). This displacement is reflected in the color profile (Figure 4-14g) with a dip in the blue paired with a simultaneous increase in cyan. Finally, the blue reenters the domain and fills it completely (Figure 4-14f,g). Interestingly, these observations seem to indicate that deintercalation occurs during intercalation, since cyan (an earlier substage) displaces blue. In addition, the speed distributions reveal that the colors follow a similar pattern as intercalation overall, with orange, magenta, and purple having faster rates than blue and cyan.

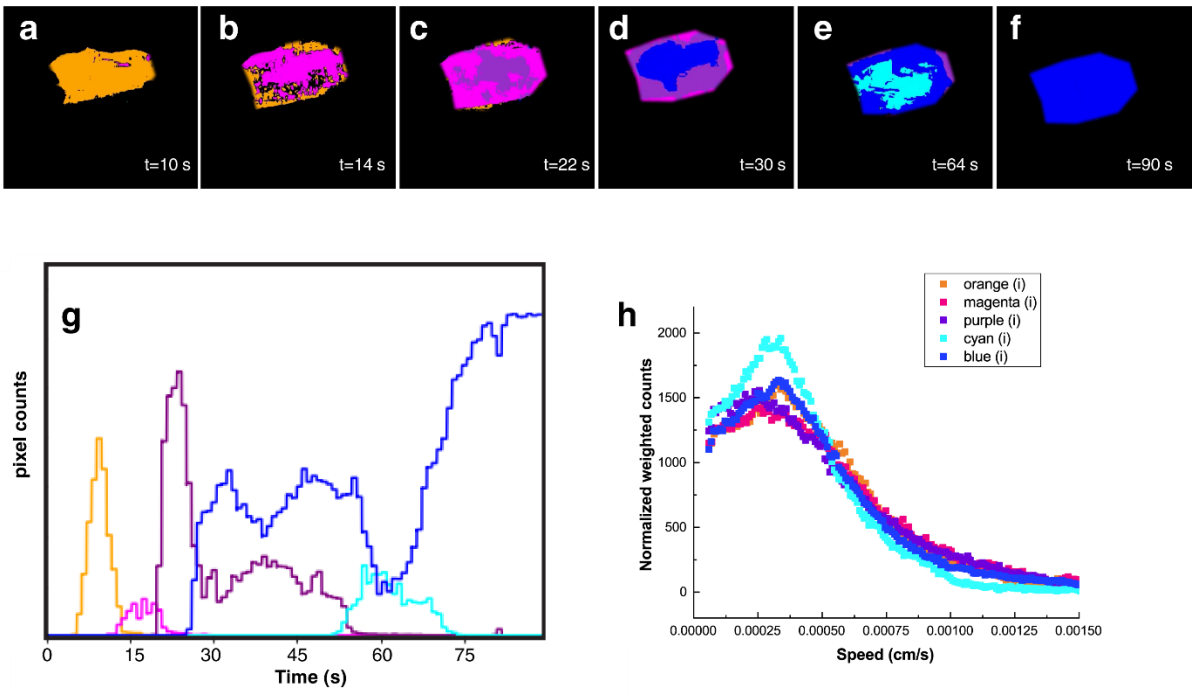


Figure 4-14: Analysis of domain 1, showing the evolution of colors during intercalation from the masked frames a)-f), the pixel counts (g), and the distribution of rates (h).

In ROI3 (Figure 4-15), the colors emerge in a similar fashion to ROI1 for early substages. However, at later times, the domain undergoes more significant deintercalation, with the colors turning blue, then cyan (Figure 4-15e), followed by purple (Figure 4-15f). Importantly, ROI1 and ROI3 are two of the first ROIs to intercalate, which suggests that they are adjacent to favorable pathways. However, since we observe partial deintercalation of the domains, it is possible that they are bounded by domains with unfavorable routes for ion transport on at least one side. Thus, ROI1 and ROI3 fill quickly, from one or more sides, but neighboring domain(s) remain unfilled. Since the intercalant islands cannot enter the neighboring domains by other routes, the concentration gradient builds between ROI3 and its

neighbor. Eventually, ions leave ROI3 (Figure 4-15f) and the domain is filled through the pathways by which it was filled originally.

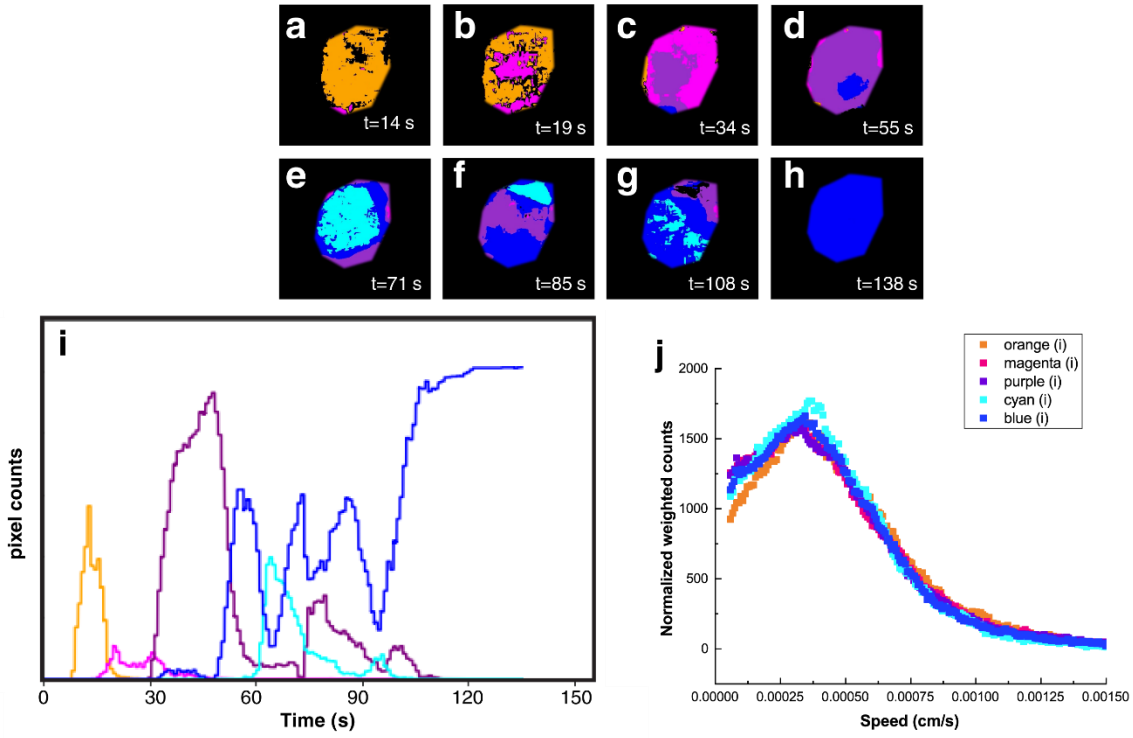


Figure 4-15: Analysis of domain 3, showing the evolution of colors during intercalation from the masked frames a)-h), the pixel counts (i), and the distribution of rates (j).

In addition to intercalation, we also present an analysis of two regions during deintercalation: dROI2 (Figure 4-16) and dROI6 (Figure 4-17). (Both domains are pictured in Figure 4-13a). Figure 4-16a-f shows how the colors change during deintercalation. Initially, the domain appears blue, then cyan emerges, followed by blue again. This observation suggests that the domain deintercalated to the cyan substage and then re-intercalated to blue before passing through the other substages (cyan, purple, magenta, orange). With the exception of the blue-cyan-blue transition at early times, the domain exhibits the same color pattern (Figure 4-16a-e) we observed across the full frame (Figure 4-7b). However, the rate distribution of individual colors is different from what we observe during deintercalation. During the initial

appearance of each color (Figure 4-16g), blue, cyan, and orange have faster rates than magenta and purple. At later times, magenta appears to exhibit faster distributions compared to the other colors, followed by cyan and blue/purple (Figure 4-16h).

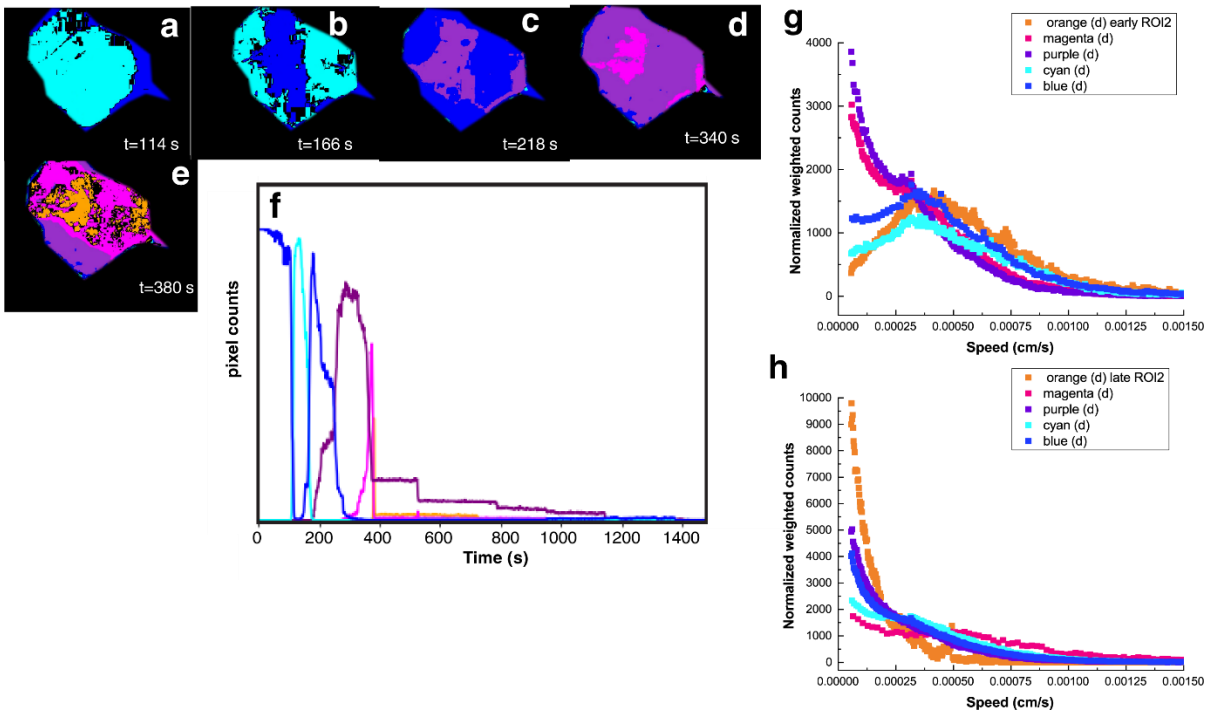


Figure 4-16: Analysis of domain 2, showing the evolution of colors during deintercalation from the masked frames a)-e), the pixel counts (f), and the distribution of rates at g) early and h late times.

For dROI6, the appearance of the colors is slightly different from dROI2. Here, the cyan does not propagate through the region. Instead, the domain transitions directly from blue to purple within the first few minutes of deintercalation. Once deintercalation of the domain, the transition from blue to orange is fairly rapid, taking only ~37 s (Figure 4-17a-d). However, the color then turns magenta again as the orange disappears (Figure 4-17e). Then, the orange color nucleates and the two colors remain in the region simultaneously (Figure 4-17f,g) until ~15 minutes have elapsed, before disappearing completely.

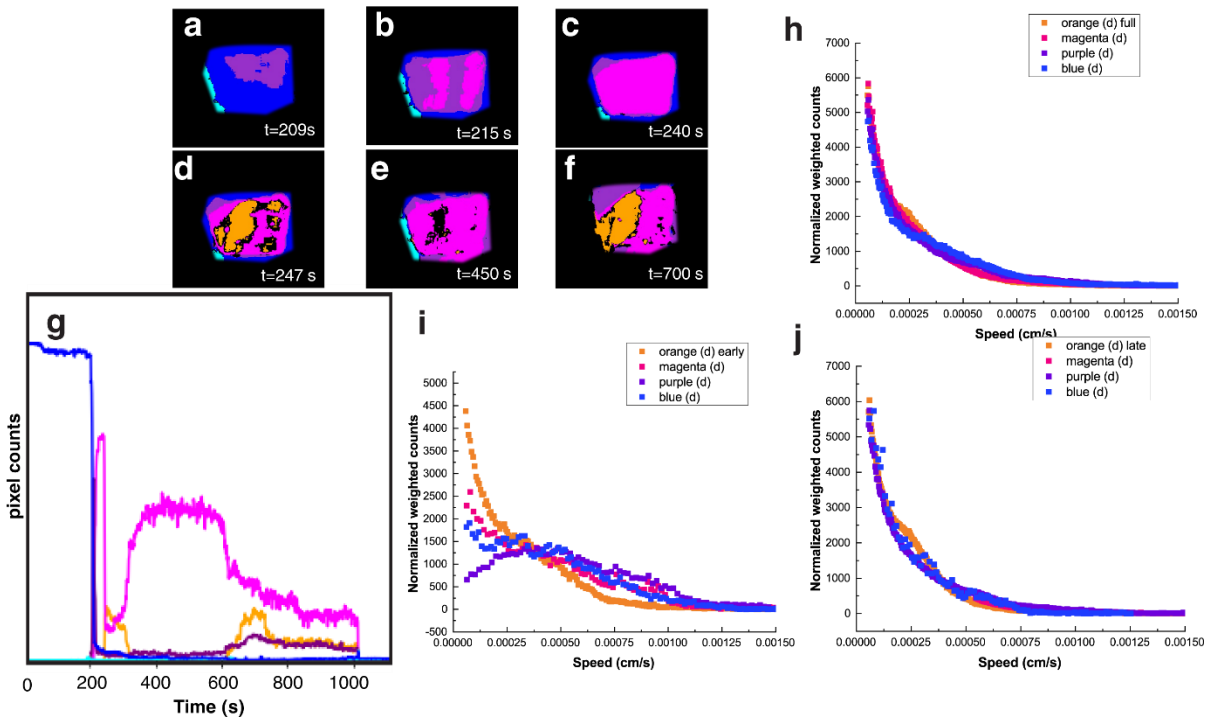


Figure 4-17: Analysis of domain 6, showing the evolution of colors during deintercalation from the masked frames a)-h), the pixel counts (i), and the distribution of rates (j).

4.4 Conclusion and Future Work

In summary, we have developed a video analysis platform to investigate staging dynamics and quantify transport rates during (de)intercalation. We hypothesized that the colors represent substages of distinct stage 1/stage 2 composition and our observations of the reproducible color changes, the slower rates with increasing stage 1 composition, and the color patterns observed in individual domains during (de)intercalation strengthen this suggestion. Faster transport rates at early times for specific colors during both intercalation and deintercalation suggest that there may be competition between electrostatic repulsion/strain

considerations and the availability of less resistive transport pathways. In addition, the dynamics we presented for the individual domains further strengthen the idea that the mechanism of staging and transport is complex, even in a supposedly homogeneous graphite sample, like HOPG and motivates further study.

Importantly, these analyses can be extended to other intercalation compounds that exhibit color changes, and provide an opportunity to study the kinetics of intercalation in a variety of systems. A particularly interesting subset of these intercalation compounds would be ultrathin flakes, since these materials have different lateral sizes and thicknesses, which affect transport rates[1] (see Chapter 1). It would also be interesting to study whether (de)intercalation rates in a flake change with cycling. We have included code for the ultrathin flake analysis for the bisulfate system in our code (Section 4.2) and have already acquired experimental images (Section 2.6) for such an analysis.

In the future, we also hope to perform electron-backscattered diffraction (EBSD) SEM to look at the orientation, grain boundaries and local structure of the graphite before intercalation and after deintercalation. Combining this method with observations from our video analysis program would give us insight into how the local structure influences (de)intercalation. If transport pathways play a role, we would expect to see correlations between the presence of grain boundaries or rotational disorder and transport rates.

In addition, we are currently modeling the graphite-bisulfate intercalation process using a 6-layer model in COMSOL to verify the intercalation rates and observe the staging dynamics using the finite element method[23–25]. This method involves modeling the free energy of a layered system, taking the variational derivative of the free energy to obtain the chemical potential, and calculating the flux from these values[23–25]. From these calculations, we can

obtain voltage profiles, and intercalation rates for the individual colors. These results will lay the foundation for our lab to probe phase transformations during (de)intercalation and extend our analysis to the advanced battery materials the Warren group is developing.

REFERENCES

[1] M. S. Stark, K. L. Kuntz, S. J. Martens, S. C. Warren, *Adv. Mater.* **2019**, *31*, 1.

[2] M. S. Dresselhaus, Ed. , *Intercalation in Layered Materials*, Plenum Press, New York, **1986**.

[3] M. S. Dresselhaus, G. Dresselhaus, *Adv. Phys.* **1981**, *51*, 1.

[4] J. Wan, S. D. Lacey, J. Dai, W. Bao, M. S. Fuhrer, L. Hu, *Chem. Soc. Rev.* **2016**, *45*, 6742.

[5] A. M. Dimiev, K. Shukhina, N. Behabtu, M. Pasquali, J. M. Tour, *J. Phys. Chem. C* **2019**, *123*, 19246.

[6] Y. Guo, R. B. Smith, Z. Yu, D. K. Efetov, J. Wang, P. Kim, M. Z. Bazant, L. E. Brus, *J. Phys. Chem. Lett.* **2016**, *7*, 2151.

[7] J. Wan, W. Bao, Y. Liu, J. Dai, F. Shen, L. Zhou, X. Cai, D. Urban, Y. Li, K. Jungjohann, M. S. Fuhrer, L. Hu, *Adv. Energy Mater.* **2015**, *5*, 1401742.

[8] W. Bao, J. Wan, X. Han, X. Cai, H. Zhu, D. Kim, D. Ma, Y. Xu, J. N. Munday, H. D. Drew, M. S. Fuhrer, L. Hu, *Nat. Commun.* **2014**, *5*, 4224.

[9] M. S. Stark, J. Cheng, H. Kim, K. L. Kuntz, S. C. Warren, *Small* **2020**, *17*, DOI 10.1002/smll.202004823.

[10] A. M. Dimiev, G. Ceriotti, N. Behabtu, D. Zakhidov, M. Pasquali, R. Saito, J. M. Tour, *ACS Nano* **2013**, *7*, 2773.

[11] P. C. Eklund, in *Intercalation Layer. Mater.* (Ed.: M.S. Dresselhaus), Springer, New York City, USA, **1986**, pp. 337–344.

[12] R. Stone, "Image Segmentation Using Color Spaces in OpenCV + Python.," can be found under https://realpython.com/python-opencv-color-spaces/. , **2020**.

[13] J. Cheng, H. D., Jiang, X. H., Sun, Y., & Wang, *Pattern Recognit.* **2001**, *34*, 2259.

[14] N. Baldwin, “Colorimetry and the Cartography of Color,” can be found under https://medium.com/thinking-design/colorimetry-and-the-cartography-of-color-415ef5315c0a, **2019**.

[15] A. Bradski, Gary, Kaehler, *Learning OpenCV: Computer Vision with the OpenCV Library*, O’Reilly Media, **2008**.

[16] J. Canny, *IEEE Trans. Pattern Anal. Mach. Intell.* **1986**, *8*, 679.

[17] C. Lin, “Introduction to Motion Estimation with Optical Flow,” can be found under https://nanonets.com/blog/optical-flow/, **2020**.

[18] T. K. B. D. Lucas, in *Proc. Imaging Underst. Work.*, **1981**, pp. 121–130.

[19] G. Farnebäck, in *Scand. Conf. Image Anal.*, **2003**, pp. 363–370.

[20] D. W. Scott, *Biometrika* **1979**, *66*, 605.

[21] K. He, G. Meeden, *J. Stat. Plan. Inference* **1997**, *61*, 49.

[22] M. S. Dresselhaus, G. Dresselhaus, *Adv. Phys.* **1981**, *51*, 1.

[23] R. B. Smith, E. Khoo, M. Z. Bazant, *J. Phys. Chem. C* **2017**, *121*, 12505.

[24] T. R. Ferguson, M. Z. Bazant, *Electrochim. Acta* **2014**, *146*, 89.

[25] M. Chandesris, D. Caliste, D. Jamet, P. Pochet, *J. Phys. Chem. C* **2019**, DOI 10.1021/acs.jpcc.9b05298.